2018-03-14

Development of a New Real-Time Precise Point Positioning System

Yang, Hongzhou

UNIVERSITY OF CALGARY

Development of a New Real-Time Precise Point Positioning System

by

Hongzhou Yang

A THESIS

SUBMITTED TO THE FACULTY OF GRADUATE STUDIES

IN PARTIAL FULFILMENT OF THE REQUIREMENTS FOR THE

DEGREE OF DOCTOR OF PHILOSOPHY

GRADUATE PROGRAM IN GEOMATICS ENGINEERING

CALGARY, ALBERTA

March, 2018

Abstract

Real-time Precise Point Positioning (PPP) is drawing increasing attentions from both the Global Navigation Satellite System (GNSS) community and real-time users with different applications, such as offshore navigation, precise agriculture and hazard warning. To meet the rapidly increasing demand, the International GNSS Service (IGS) Real-Time Service (RTS) is currently disseminating several real-time high-frequency State Space Representation (SSR) products through the Internet under the Networked Transport of Radio Technical Commission for Maritime Services (RTCM) via the Internet Protocol (NTRIP) protocol. High availability of real-time PPP services requires high availability of precise orbit and clock corrections. Any correction outage, either due to corrupted ephemeris or loss of communication link, will degrade the availability of precise positioning using the service. Meanwhile, the communication burden is very heavy with such high update rates.

To tackle the above limitations, a new robust real-time PPP system with higher availability is proposed in this thesis. The proposed system consists of three components regarding server end, communication end and user end. For the new real-time PPP system, the satellite orbit and clock Initial Parameters (IP) products are generated at the server end and broadcast to the user end for the generation of high precision orbit and clock products, afterwards, the real-time PPP can be carried out with the IP-based high precision satellite products. With the IP products, the real-time PPP system can operate with scalable update rates according to the various accuracy requests of different applications. Furthermore, the new real-time PPP system can continue during Internet connection outages, which is not uncommon in real applications due to the Internet connection

losses. The prototype of the new real-time PPP system is developed and substantially tested in real-time.

Keywords: New real-time PPP system, Initial parameters, Satellite orbit prediction, Satellite clock offsets prediction, scalable update rates, Internet connection outages

Acknowledgements

I would express my heartful gratitude to my supervisor, Dr. Yang Gao. Not only the academic skills are imparted by him, but also the attitude towards life and difficulties. With the light shed by him, the research challenge for a Ph.D. student becomes more tolerable and fruitful. I have seen Dr. Gao actively sought out opportunities for his graduate students and supported us to present research results at international conferences such as the ION GNSS+ to have an early impact on applications.

I would like to thank my committee members: Dr. Naser El-Sheimy and Dr. Susan Skone from Department of Geomatics Engineering. Dr. Lina Kattan from Department of Civil Engineering, University of Calgary, and Dr. Sunil Bisnath from York University.

I would give my sincere thanks for the funding from the Chinese Scholarship Council (CSC), and the University of Calgary, which supports my whole Ph.D. period in the Department of Geomatics Engineering, University of Calgary, Canada.

With the company of the group members, the life in Canada becomes more joyful and warm. They are Dr. Min Wang, Dr. Shuang Du, Dr. Yihe Li, Dr. Yashar Balazadegan Sarvrood, Bei Huang, Wentao Zhang, Feng Xu, Dr. Shaohua Chen, Fei Liu, Yan Xiang, Ye Wang, Peiyuan Zhou, Kaixiang Tong, Yuting Gao. Special thanks also go to the students in other groups and visiting scholars: Dr. Haiyu Lan, Dr. You Li, Prof. Jingui Zou, Prof. Fuhong Wang, Prof. Jiazhu Zheng, Dr. Tao Li, Dr. Yongxue Zhang, Prof. Hongzhou Chai, Dr. Zhixi Nie, Xiaoming Dong, Jingjing Dou, Han Zheng and Jia Qiu.

Last but not least, I want to give my wholehearted appreciation to my parents Fan Yang, Meilan Cai, my wife Anqi Chen and my younger brother Yazhou Yang. Without the love from them, I can hardly conquer the difficulties in both life and research.

Dedication

To my parents

Fan Yang and Meilan Cai,

My wife,

Anqi Chen

Table of Contents

List of Tables

List of Figures and Illustrations

List of Abbreviations

Abbreviations	Definition
AC	Analysis Centers
ADEV	Allan Deviation
APC	Antenna Phase Center
ARP	Antenna Reference Point
AVAR	Allan Variance
BNC	BKG NTRIP Client
CDDIS	Crustal Dynamics Data Information System
CODE	Center for Orbit Determination in Europe
CoM	Center of Mass
Cs	Cesium
DE	Development Ephemerides
DFFT	Discrete Fast Fourier Transform
DOY	Day of Year
ECOM	Empirical CODE Orbit Model
EGNOS	European Geostationary Navigation Overlay Service
ET	Ephemeris Time
FFT	Fast Fourier Transform
GAGAN	GPS Aided GEO Augmented Navigation
GDOP	Geometry Dilution of Position
GEO	Geosynchronous Earth Orbit

GNSS	Global Navigation Satellite System
HDOP	Horizontal Dilution of Position
ICRF	International Celestial Reference Frame
ICRS	International Celestial Reference System
IDFFT	Inverse Discrete Fast Fourier Transform
IERS	International Earth Rotation and Reference Systems Service
IF	Ionosphere Free
IGS	International GNSS Service
IGR	IGS Rapid
IGU	IGS ultra-rapid
IIF	II Follow-on
IIR	II Replenishment
IIR-M	II Replenishment-Modernized
IP	Initial Parameters
ICRF	International Celestial Reference Frame
ITRF	International Terrestrial Reference Frame
JPL	Jet Propulsion Laboratory
LS	Least Square
MEO	Medium Earth orbit
MSAS	Multifunction Satellite Augmentation System
MVAR	Modified Allan Variance

NTRIP	Networked Transport of RTCM via Internet Protocol
PCO	Phase Center Offset
PCV	Phase Center Variations
PDOP	Positioning Dilution of Position
PPP	Precise Point Positioning
PRN	Pseudo-Range Number
Rb	Rubidium
RTCM	Radio Technical Commission for Maritime Services
RTK	Real-Time Kinematic
RTS	Real-Time Service
RTWG	Real-Time Working Group
SISRE	Signal-in-Space Range Error
SISURE	Signal-in-Space User Range Error
SRP	Solar Radiation Parameter
SSR	State Space Representation
STD	Standard Deviation
STEC	Slant Total Electron Content
SVN	Satellite Vehicle Number
TDOP	Time Dilution of Position
TRS	Terrestrial Reference System
UAV	Unmanned Aerial Vehicle
UEE	User Equipment Error

UERE	User Equivalent Range Error
UTC	Coordinated universal time
VDOP	Vertical Dilution of Position
VTEC	Vertical Total electron content
WAAS	Wide Area Augmentation System

CHAPER ONE: INTRODUCTION

1.1 Background

Precise Point Positioning (PPP) is an advanced technique to obtain centimeter to decimeter level positioning accuracy worldwide with a single Global Navigation Satellite System (GNSS) receiver (Zumberge et al. 1997). Compared to relative positioning techniques such as Real-Time Kinematic (RTK) requiring at least two receivers operating simultaneously, PPP can produce high accuracy position solutions more efficiently with a single GNSS receiver. To obtain high accuracy solutions, various error sources must be considered and mitigated in PPP processing, such as satellite orbit errors, satellite clock errors, troposphere refraction, ionospheric effects, carrier phase wind up effects, relative effects, antenna phase offsets and variations, solid Earth tide effects and ocean loading tide effects. Typically, precise satellite orbit and clock products provided by International GNSS Service (IGS) are utilized to mitigate the satellite orbit and clock errors correspondingly, which are the most significant error sources in GNSS positioning (Bisnath and Gao 2009). However, limited by the long latency of precise orbit and clock products previously, PPP was primarily operated in post-mission mode and used in scientific applications with less demands in terms of timeliness such as crustal deformation monitoring and low-Earth-orbit satellite-based gravity recover determination. Recently, driven by increasing demands from the user community and maturing in the real-time infrastructure construction, real-time PPP is emerging in various applications by using real-time precise satellite orbit and clock products (Choy et al. 2017). The crucial aspect of real-time PPP is the availability of real-time precise satellite orbit and clock products, which are generated and disseminated at very high update rates by different research institutes and companies. Satellite orbit and clock products

belong to State Space Representations (SSR), which can be physically modelled and update rates can be different (Weber 2012). With different physical characters, the satellite orbit and clock products can be updated at different rates, such as 60 s for orbit and 10 s for clock of IGS03 products. The availability of real-time PPP solutions elevates PPP as a potentially alternative to differential GNSS techniques, in particular the highly productive and practical RTK solution (Grinter and Roberts, 2013). Currently, real-time PPP is widely used in various applications, such as geohazard monitoring, time transferring, hydrography, atmospheric remote sensing, precision agriculture and offshore navigation. Meanwhile, the demands for high-precision low-cost high-available positioning solutions are increasing from a wide range of applications in the mass market, such as autonomous driving and Unmanned Aerial Vehicle (UAV). For those applications concerning safety and economic benefits, the requirements for reliability are much higher and the communication costs are considered as a crucial factor.

In 2001, the IGS Real-Time Working Group (RTWG) was established aimed at generation and dissemination of real-time products to users. The IGS workshop themed "Towards Real Time" was held in Ottawa in the spring of 2002 to discuss the prototype of Real-Time Service (RTS). In June 2007, the IGS announced the Call for Participation in the IGS Real-time Pilot Project and officially launched RTS in 2013. Currently, the IGS RTS products are broadcast to the real-time users through Internet based on NTRIP (Weber *et al.*, 2005). The PPP users can recover the precise orbit and clock information by applying the RTS to broadcast ephemeris. There are several RTS products that can be received in real-time via the Internet from IGS freely, including IGS01, IGS03, CLK01, CLK15, CLK20, CLK22, CLK52, CLK70, CLK81 and CLK90, as listed in Table 1-1. IGS01 and IGS03 are two combined RTS products mostly used by real-time PPP

users, which are firstly generated by individual real-time ACs and combined by IGS real-time analysis center coordinator. The other RTS products generated by eight individual real-time ACs are broadcast to real-time users directly. The update rates of RTS are very high, typically 5~10 seconds for satellite clock and 5~60 seconds for satellite orbit. To access the correction streams produced by the IGS RTS, an NTRIP client application must be installed at the user side. To date, the BKG NTRIP Client (BNC) (Weber and Mervart 2007) and the RTKLIB software (Takasu, 2012) are the mostly commonly used open source applications to retrieve the correction stream.

Table 1-1 Brief description of ten RTS products

Products	Generating agency	update rates (Orbit/Clock)	Orbit reference point
IGS01	ESA/ESOC	5/5	APC
IGS03	BKG	60/10	APC
CLK01	BKG	60/ 5	CoM
CLK15	WUHAN	5/5	CoM
CLK20	DLR	5/5	APC
CLK22	NRCan	5/5	APC
CLK52	ESA/ESOC	5/5	CoM
CLK70	GFZ	10/5	APC
CLK81	GMV	5/5	CoM
CLK90	CNES	5/5	CoM

APC: Antenna Phase Center; CoM: Center of Mass

There are also some commercial services existed earlier in the market supporting real-time PPP such as OmniSTAR, Starfire, Veripos and Terrastar. The common used commercial real-time products are presented in Table 1-2. For the service provided by companies, the high update rate corrections are broadcasted through either the Internet or L-band satellite with the preference of

the user. It requires an annual subscription fee and specialty hardware (L-band) to receive the signal (Gakstatter 2013).

Table 1-2 Real-time correction Product/Service and the corresponding companies

Product/Service	Companies
RTX, OmniSTAR	Trimble Navigation, Ltd (Leandro et al. 2011)
Atlas	Hemisphere GNSS
G2+	Fugro N.V.
StarFire	NavCom Technology, Inc.
TERRASTAR	NovAtel Inc., Altus Positioning Systems, Septentrio
Apex, Ultra	Veripos, Septentrio
C-NavC	C-Nav
MagicPPP	GMV (Merino and Lainez 2012)

With the availability of the real-time corrections, various studies have been carried out for the performances of real-time PPP (Gao and Chen, 2004; Chen *et al.*, 2013; Liu and Stürze, 2013; Li *et al.*, 2015; Elsobeiey and Al-Harbi, 2016). To shorten the convergence time of real-time PPP, studies were carried out regarding to regional augmentation, multipath mitigation and ambiguity resolution (Collins et al. 2008; Mervart et al. 2008; Geng et al. 2011; Laurichesse 2011; Li 2012; Hadas et al. 2013; Shi et al. 2014; Li and Zhang 2014; Seepersad and Bisnath 2015; Li et al. 2015a, b, 2016). The real-time cycle slip detection and fixing is also studied by some scholars (Banville and Langley 2010; Zhang and Li 2012). Real-time PPP in various applications - ionosphere determination, troposphere determination and earthquake warning - are investigated (Li *et al.*, 2013; Yuan *et al.*, 2014; Abdelazeem *et al.*, 2016). For single-frequency users, real-time PPP is also studied by some scholars (Chen and Gao 2005; van Bree and Tiberius 2012; de Bakker and Tiberius 2017). Hadas and Bosy (2014) evaluated the degradation of IGS RTS over time and attempted short-term prediction of IGS RTS. Regarding to the availability of the real-

time PPP, some initial studies are carried out for mitigating outage (El-Mowafy *et al.*, 2017), but only the Standard Deviation (STD) of the positioning results are presented.

1.2 Limitations

Although high precision satellite orbit and clock corrections are widely available in real-time now, a continuous connectivity is required for PPP users to continuously receive precise orbit and clock corrections so that the orbit and clock errors can be mitigated for precise position determination. There are several major limitations for existing works and they are listed in the following,

1. Currently, the generation of real-time corrections in real-time Analysis Centers (AC) consists of two steps, the first step is to obtain precise orbit and clock products and then format them into RTCM SSR by fitting the difference between the precise products and broadcast ephemeris based on simple mathematic models. To maintain high precision, the prediction length of real-time corrections based on simple mathematic models for real-time PPP users is limited. Thus, current real-time PPP systems need to update the real-time corrections at very high rates.
2. For current precise orbit and clock products, the update rates are very high, typically every 5~60 seconds for satellite orbit corrections and every 5~10 seconds for satellite clock corrections. Such a high update rate of corrections means a large amount of corrections data will be transmitted to PPP users. Thus, products with high update rates may not be feasible for many applications in the mass market concerning about communication cost, which is particularly true for precision applications with mobile devices.

3. High update rates of real-time correction poses heavy operation burden on the whole real-time PPP system. For example, the server such as real-time ACs need to update the RTS products with very high rates such as every 5 seconds, which makes it very challenging to ensure the reliability of the RTS products. Meanwhile, frequent connection between the server and the PPP users and server need to be ensured, which can be difficult for some applications operated in a challenging network environment.
4. A continuous connectivity is required in current real-time PPP system for real-time PPP users to receive high-frequency precise orbit and clock connections to mitigate orbit and clock errors for precise position determination. A loss of correction data due to loss of network connectivity would quickly degrade the performance of the positioning solutions. For those applications concerning safety, the requests for the availability is much higher and current real-time PPP system can't meet the demands.

1.3 Objective and Contributions

The overall objective of this thesis is to develop a new real-time PPP system to address the aforementioned limitations in real-time PPP applications, particularly in support of mass-market applications. The major contributions of this thesis include:

1. Initial Parameters (IP) is proposed as an accurate condensed real-time message to be transmitted for real-time PPP system. For each satellite, the orbit IP includes the satellite position, velocity and SRP, while the satellite clock IP consists of the polynomial terms and periodic terms. Different from current RTS products fitted with simple mathematic model, IP is based on physical characters of satellite orbit and clock and has longer life cycle. Thus, IP allows the update rates of orbit and clock products to be scalable dependent on

application performance requirements. Meanwhile, IP can be used to maintain the high precision PPP solution with longer outages.

2. IP is designed in an extended SSR format, with only SRP and periodic terms are added to current RTS, to keep compatible with current real-time PPP system. PPP users can choose to utilize the current SSR or extended SSR products seamlessly. This mode is called "tightly coupled mode" of IP and RTS in this thesis.
3. A real-time PPP system based on IP orbit and clock products are designed and developed, which is able to mitigate connection outages and improve the availability of precise positioning in challenging environments, and also improve the robustness and cost of the positioning system. Apart from the real-time positioning at the user end, the new system also addresses the generation and dissemination of IP products at server end.
4. Methods and algorithms for real-time generation of satellite orbit and clock IP products at the server end have investigated and developed. For the orbit IP generation, dynamic models regarding primary forces on GPS satellites are investigated, and the numerical integrators including both the single-step and multi-step methods are implemented. For the satellite clock IP generation, a new satellite clock offset prediction method considering the datum jump is proposed and implemented.
5. The real-time high precision orbit and clock prediction using IP products have been investigated and developed at user end. After receiving IP products disseminated by server, the high precision orbit and clock prediction is implemented at user end with scalable update rates which is able to mitigate correction outages and maintain continuous

availability of precise positioning solutions. The accuracy of the predicted satellite orbit and clock is also investigated.

6. Software modules in C++ have been developed to implement the algorithms and methods developed for the new real-time PPP system, regarding server end, communication end and user end. This software module at user end is designed and implemented as cross-platform (Windows and Linux), and thus the IP based prediction and real-time PPP can be carried out both in Windows system and Linux system.
7. A prototype system has been developed to integrate different components of the new real-time PPP system to support field tests and positioning performance analysis, using scalable update rates of IP products and for mitigation of correction outages. The prototype system has been tested in various real-time scenarios with the server continuously operating in real-time to generate and disseminate IP products through the Internet.

1.4 Thesis outline

Chapter Two firstly introduces the observation equations of PPP regarding pseudo-range code and carrier phase observations; afterwards, the error sources including satellite-related errors, transmission related errors and receiver associated errors and corresponding mitigation methods are presented. Finally, the state estimation for the PPP is introduced with focus on Kalman filter.

Chapter Three introduces the structure and design of the new real-time PPP system in terms of server end, user end and communication end. For each component in the new system, the function modules are explained in details and the IP related modules are highlighted.

Chapter Four presents the implementation of satellite orbit and clock IP generation at the server end. For the orbit part, the variation equations are solved with numerical integrators including

both single-step and multi-step methods, during which the primary forces acting on the satellites as well as the corresponding partial derivatives with respect to orbit IP are considered carefully. The implementation of the satellite clock IP generation at server end is introduced afterwards. The mitigation method of day boundary jump issue is proposed for the satellite clock offsets prediction. An innovative satellite clock offsets prediction model is originated, which can be effectively applied for IGS RTS clock predictions.

Chapter Five addresses the realization of the precise orbit and clock offsets prediction by applying the IP products at the user end. Furthermore, the predicted orbit and clock products are evaluated separately.

Chapter Six illustrates the system prototype regarding server end, communication end and user end firstly. Afterwards, the positioning performances are analyzed focusing on two primary features, scalable update rates and outage mitigation. Extensive static and kinematic real-time PPP tests are carried out to investigate the performances of the new real-time PPP systems.

Chapter Seven summarizes the results and draws the conclusions and provides suggestions for future work.

CHAPER TWO: PPP OBSERVATION EQUATIONS, ERROR SOURCES AND MITIGATION

In this Chapter, the observation equations of the PPP technique are first discussed in Section 2.1 regarding pseudo range and carrier phase observations. Section 2.2 introduces the error sources in PPP and the corresponding mitigation strategies. Least Square (LS) estimation and Kalman filter are briefly introduced for state estimation.

2.1 The Observation Equations of PPP

The un-differenced pseudo range and carrier phase observation equations for PPP at different signal bands can be expressed as:

$$\begin{aligned} P_{Li} &= \rho + dT + \delta Orb + \delta Clk + dSag + dTrop + a_{Li} dIono_{L1} \\ &\quad + d\,\mathrm{Re}l + dSite + RB_{P_{Li}} - SB_{P_{Li}} + \varepsilon\left(P_{Li}\right) \\ \Phi_{Li} &= \rho + dT + \delta Orb + \delta Clk + dSag + dTrop - a_{Li} dIono_{L1} \\ &\quad + d\,\mathrm{Re}l + dSite + dWind + dCenter + \lambda_{Li} N_{Li} + RB_{\Phi_{Li}} - SB_{\Phi_{Li}} + \varepsilon\left(\Phi_{Li}\right) \end{aligned} \tag{2-1}$$

where,

L_i denotes the GNSS signal bands, i.e. L_1 , L_2 or L_5 ;

P_{Li} denotes the measured pseudo-range on L_i (m)；

Φ_{Li} denotes the measured carrier-phase on L_i ;

ρ denotes the calculated geometric range;

dT denotes the receiver clock;

δOrb denotes the satellite orbit error；

δClk denotes the remaining satellite clock error after applying the clock correction；

$dSag$ denotes the Sagnac effect;

$dTrop$ denotes the troposphere delay;

$dIono_{Li}$ denotes the ionosphere delay on L_1 (m);

$d\,\mathrm{Re}\,l$ denotes the relativity effect;

$dSite$ denotes the site displacement effect;

$dWind$ denotes the phase windup effect;

$dCenter$ denotes the antenna center phase offset;

a_{Li} denotes the ionosphere dispersion coefficient for L_i as $a_{Li} = f_1^2 / f_i^2$;

λ_{Li} denotes the wavelength of L_i(m);

N_{Li} denotes the integer ambiguity on L_i;

$RB_{P_{Li}}$ denotes the receiver FCB of pseudorange code on L_i;

$RB_{\Phi_{Li}}$ denotes receiver FCB of carrier phase on L_i;

$SB_{P_{Li}}$ denotes satellite FCB of pseudorange code on L_i

$SB_{\Phi_{Li}}$ denotes satellite FCB of carrier phase on L_i

$\varepsilon\left(P_{Li}\right)$ denotes the measurement noises including multipath of pseudorange code on L_i

$\varepsilon\left(\Phi_{Li}\right)$ denotes the measurement noises including multipath of carrier phase on L_i

Three PPP models are commonly used, including the Ionospheric-Free (IF) model (Kouba and Héroux 2001), the UoC model (Gao and Shen 2002) and the un-differenced un-combined model

(Abdel-salam 2005). In this thesis, the IF model is used if there is no special statement to the contrary.

2.2 PPP Related Error Sources and Mitigation Methods

To obtain high precision positions, GNSS error sources must be handled carefully, either to be estimated or modeled. Generally, the error sources fall into three main categories, including satellite-related error sources, receiver-related error sources and the transmission-related error sources. In this chapter, the details of each category are introduced as well as the corresponding mitigation technologies.

2.2.1 Satellite orbit and clock errors

GPS satellites operates in Medium-Earth-Orbit (MEO) with altitude of approximately 20,200 km. Four satellites are spreading in each of six orbital planes, which are identified from A to F. The nominal GPS constellation (Teunissen and Montenbruck 2017) parameters are listed as follows,

Table 2-1 Nominal GPS constellation parameters

Parameter	Value
Number of operational satellites	24
Number of orbit planes	6
Number of satellites in a plane	4
Orbit type	Near circular
Eccentricity	Less than 0.02
Inclination	55^0
Nominal orbital altitude	20180 km
Period of revolution	11 h 58 m
Longitude of ascending node between planes	60^0
Ground track repeat cycle	2 times in 1 sidereal day

In recent years, the constellation has been overpopulated with up to 31 operational satellites (U.S. COAST GUARD NAVIGATION CENTER 2018), which is listed as follows,

Table 2-2 GPS CONSTELLATION STATUS

Plan	Slot	SVN	PRN	Block	Clock	Plan	Slot	SVN	PRN	Block	Clock
A	1	65	24	IIF	CS	D	2	66	27	IIF	RB
A	2	52	31	IIR-M	RB	D	3	72	8	IIR	RB
A	3	64	30	IIF	RB	D	4	53	17	IIF	RB
A	4	48	7	IIR-M	RB	D	5	59	19	IIR	RB
B	1	56	16	IIR	RB	E	1	69	3	IIF	RB
B	2	62	25	IIF	RB	E	2	73	10	IIF	RB
B	3	44	28	IIR	RB	E	3	50	5	IIR-M	RB
B	4	58	12	IIR-M	RB	E	4	54	18	IIR	RB
B	5	71	26	IIF	RB	E	6	47	22	IIR	RB
B	6	51	20	IIR	RB	F	1	70	32	IIF	RB
C	1	57	29	IIR-M	RB	F	2	55	15	IIR-M	RB
C	2	66	27	IIF	RB	F	3	68	9	IIF	RB
C	3	72	8	IIF	CS	F	4	60	23	IIR	RB
C	4	53	17	IIR-M	RB	F	5	41	14	IIR	RB
C	5	59	19	IIR	RB	F	6	43	13	IIR	RB
D	1	61	2	IIR	RB						

Various estimation strategies are used for precise orbit determination in IGS ACs. Some ACs apply the two-step process: first to derive the orbits along with EOPs, station positions, tropospheric delays, and carrier-phase integer ambiguities using double-difference carrier phase observations, then the clock products can be obtained by fixing the above estimated parameters in the undifferenced observations. Others process undifferenced pseudo range and carrier-phase observations and estimate all parameters in one step (Teunissen and Montenbruck 2017). There are several different products for satellite orbit and clock errors, such as broadcast almanac, broadcast ephemeris, IGS precise ephemeris and real-time corrections for broadcast ephemeris. The GPS clock parameters provided by the IGS refer to the ionosphere-free linear combination

of the L1 P(Y) and L2 P(Y) signals. The accuracies of IGS products (IGS 2018a) are listed in the following Table 2-3.

Table 2-3 The description of the IGS products

Type		Accuracy	Latency	Updates	Sample Interval
Broadcast	orbits	~100 cm	real time	--	daily
	Sat. clocks	~5 ns RMS ~2.5 ns SDev			
Ultra-Rapid (predicted half)	orbits	~5 cm	real time	at 03, 09, 15, 21 UTC	15 min
	Sat. clocks	~3 ns RMS ~1.5 ns SDev			
Ultra-Rapid (observed half)	orbits	~3 cm	3 - 9 hours	at 03, 09, 15, 21 UTC	15 min
	Sat. clocks	~150 ps RMS ~50 ps SDev			
Rapid	orbits	~2.5 cm	17 - 41 hours	at 17 UTC daily	15 min
	Sat. & Stn. clocks	~75 ps RMS ~25 ps SDev			5 min
Final	orbits	~2.5 cm	12 - 18 days	every Thursday	15 min
	Sat. & Stn. clocks	~75 ps RMS ~20 ps SDev			Sat.: 30s Stn.: 5 min

The IGS final products have the highest quality and internal consistency among all IGS products, with a delay of up to 13 to 20 days. IGS Rapid products (IGR) have a quality nearly comparable to that of the final products. They are made available daily with a delay of about 17 hours after the end of the previous observation day. The ultra-rapid products are released four times per day, at 03:00, 09:00, 15:00, and 21:00 UTC. Typically, the predicted orbits between 3 and 9 hours

into the second half of each ultra-rapid orbit file are most relevant for true real-time applications (IGS 2018a). Nowadays, the IGU products are the combinations of the results from different ACs. Aside from a secular orbital plane rotation caused by the Earth-oblateness, the corresponding almanac model does not consider orbital perturbations; A perturbed Keplerian orbit representation is used for the broadcast ephemeris model; The global average Signal in Space Range Error (SISRE) values for the individual constellations amounted to 0.7 ± 0.02 m (GPS), 1.5 ± 0.1 m (BeiDou), 1.6 ± 0.3 m (Galileo), 1.9 ± 0.1 m (GLONASS), and 0.6 ± 0.2 m (QZSS) over a 12-month period in 2013/2014 (Montenbruck et al. 2015b). The historic quality of broadcast orbits and clocks (IGS 2018b) are shown as follows Fig. 2.1. The historic comparison results of AC solutions with IGS final products (IGS 2018c) are shown as Fig 2-2,

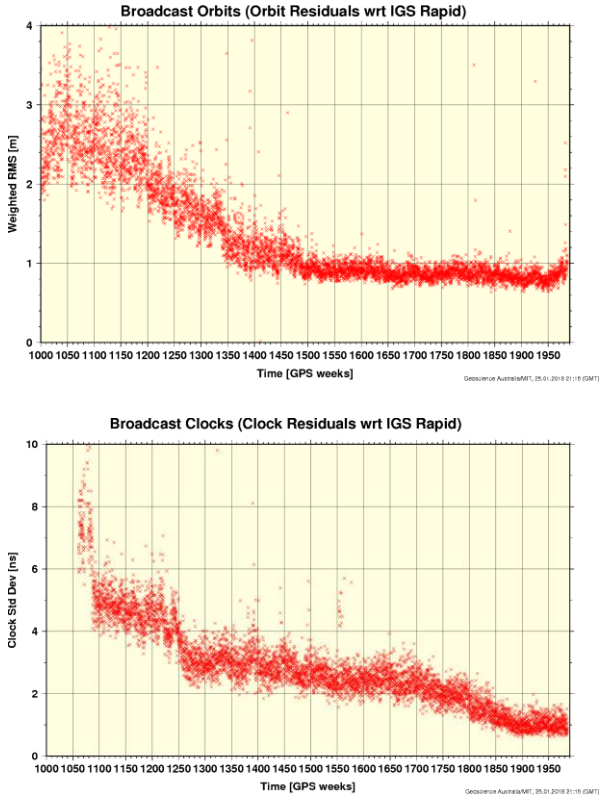

Figure 2-1 The quality of broadcast ephemeris (w.r.t to IGS Rapid)

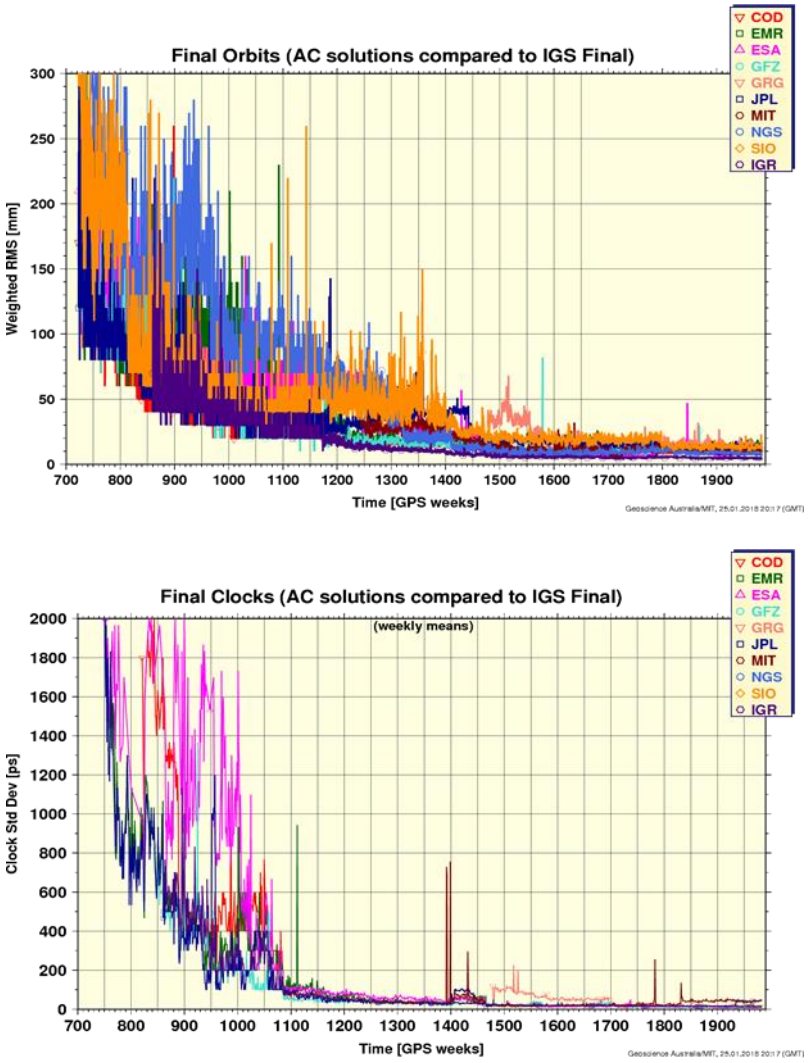

Figure 2-2 Satellite Orbit and clock errors of different ACs (w.r.t to IGS Rapid)

Four Satellite-Based Augmentation Systems (SBASs) have been implemented around the world, Wide Area Augmentation System (WAAS), Multifunction Satellite Augmentation System (MSAS), European Geostationary Navigation Overlay Service (EGNOS) and GPS Aided Geosynchronous Earth Orbit (GEO) Augmented Navigation (GAGAN). SBAS consists of three elements: the reference network, the central processing center and the GEO satellites. The reference network collects the GPS observation data in real-time and forward it to the control

center for further analysis. The control center processes the data and generates corrections and integrity. Those products are then broadcast to the users via GEO satellites. The SBAS message types (Teunissen and Montenbruck 2017) are listed as follows,

Table 2-4 SBAS message types

Type	Contents	Type	Contents
0	WAAS testing	17	GEO satellite almanacs
1	PRN mask assignments, set up to 51 and 212 bits	18	Ionospheric grid point masks
2-5	Fast pseudorange corrections and UDREs	19-23	Reserved for future messages
6	Integrity information, UDREs	24	Mixed fast/long-term satellite corrections
7	Fast correction degradation factor	25	Long term satellite corrections
8	Reserved for future messages	26	Ionospheric delay estimates and GIVEs
9	GEO navigation message (X, Y, time, etc.)	27	WAAS service message
10	WAAS network time/ Coordinated Universal Time (UTC) offset parameters	28	Clock-ephemeris covariance matrix message
11	Degradation parameters	29-61	Reserved for future messages
12	WAAS network time/(UTC) offset parameters	62	Internal test message
13-16	Reserved for future messages	63	Null message

The RTS correction streams are formatted according to the RTCM SSR and are broadcast using the NTRIP protocol. RTS corrected orbits are expressed within the ITRF 2014 (Altamimi et al. 2016). The calculation of the satellite clock offsets based on IGS RTS (Takasu and Yasuda 2013) is introduced as follows,

$$t_{satellite} = t_{broadcast} - \frac{\delta C}{c} \tag{2-2}$$

where,

$t_{broadcast}$ denotes satellite time computed according to corresponding GNSS ICD from broadcast clock parameters, identified by IOD/IODE of corresponding SSR orbit correction message;

$t_{satellite}$ denotes the satellite time corrected by SSR clock correction message;

δC denotes the clock correction obtained from SSR clock correction message;

c denotes the speed of light.

As we know, the satellite time can be expressed as the satellite clock time minus the satellite clock offset, which is shown as the following,

$$t_{corrected} = t_{clk} - tc \tag{2-3}$$

Then the final satellite clock offset can be expressed by the following equation and the sign has been changing to positive before $\frac{\delta C}{Speed\ of\ light}$,

$$tc_{satellite} = tc_{broadcast} + \frac{\delta C}{Speed\ of\ light} \tag{2-4}$$

Meanwhile, the polynomial is computed according to,

$$\delta C = C_0 + C_1(t - t_0) + C_2(t - t_0)^2 \tag{2-5}$$

where,

t denotes the epoch time;

t_0 denotes the reference time obtained from SSR Clock Correction message;

C_i denotes the polynomial coefficient from SSR Clock Correction message.

The reference time is computed by adding the GNSS epoch time with the SSR update interval, which is defined by DF391 in the RTCM.

The traditional orbit parameters include Delta radial, Delta Along-track, Delta Cross track, Dot Delta radial, Dot Delta Along-track, Dot Delta Cross track, with those parameters, the satellite orbit correction can be generated (Takasu and Yasuda 2013), which is shown in the following equations,

$$\Delta \mathrm{O} = \begin{bmatrix} \delta O_{radial} \\ \delta O_{along} \\ \delta O_{cross} \end{bmatrix} + \begin{bmatrix} \delta \dot{O}_{radial} \\ \delta \dot{O}_{along} \\ \delta \dot{O}_{cross} \end{bmatrix} \left(t - t_0 \right) \tag{2-6}$$

where,

δO_{radial} denotes orbit corrections in the radial direction at the reference time;

δO_{along} denotes orbit corrections in the along-track direction at the reference time;

δO_{cross} denotes orbit corrections in the cross-track direction at the reference time;

$\delta \dot{O}_{radial}$ denotes the orbit corrections rate in the radial direction;

$\delta \dot{O}_{along}$ denotes the orbit corrections rate in the along-track direction;

$\delta \dot{O}_{cross}$ denotes the orbit corrections rate in the cross-track direction;

t denotes the current epoch time;

t_0 denotes the GPS epoch time plus half of the update interval;

Then we can use the following equation to transfer the corrections into the ITRF in the global scale,

$$\delta X = \left[e_R \; e_T \; e_N \right] \Delta O \tag{2-7}$$

where e_R , e_T and e_N are the unit vector in radial, along track and cross track directions, which can be expressed as following,

$$\begin{aligned} e_T &= \frac{\dot{r}}{|\dot{r}|} \\ e_N &= \frac{r \times \dot{r}}{|r \times \dot{r}|} \\ e_R &= e_T \times e_N \end{aligned} \tag{2-8}$$

Then the correction will be applied to the broadcast ephemeris,

$$X_{orbit} = X_{Broadcast} - \delta X \tag{2-9}$$

where,

$X_{Broadcast}$ denotes the satellite orbit calculated from broadcast ephemeris;

X_{orbit} denotes the precise orbit after applying SSR.

2.2.2 Ionosphere effect

Ionosphere research attracts sufficient attention from the GNSS community due to the ionosphere range delay on GNSS signals is a major source in GNSS positioning. Generally, for L-band navigation signals, the ionospheric delay would be up to 15 m during the daytime, and 3 m during the nighttime. In the peak year of solar activity, the ionospheric delay might reach 40 m in the vertical direction, and 100 m the line-of-sight signal propagation (Wu et al. 2013). The GNSS radio signal will interact with charged particles. Slant Total Electron Content (STEC) and Vertical Total Electron Content (VTEC) are critical to describe the ionospheric delay and can be expressed as:

$$VTEC = \int N_e dh_0$$
$$STEC = \int N_e ds_0 \tag{2-10}$$

where,

N_e denotes the electron density and is always positive;

ds_0 denotes the slant path in the ionosphere;

dh_0 denotes the vertical path in the ionosphere;

The mapping function (Skone 2013) can convert the VTEC to STEC as:

$$M(E) = \frac{STEC}{VTEC} = \left[1 - \left(\frac{R\cos E}{R + h1}\right)^2\right]^{-1/2} \tag{2-11}$$

where,

$M(E)$ denotes the mapping function;

E denotes the elevation angle;

R denotes the Earth radius;

$h1$ denotes the height of the thin shell;

The first order ionospheric delay can be modeled as:

$$I_{Phase} = \frac{40.3}{f^2} STEC$$
$$I_{Group} = -\frac{40.3}{f^2} STEC \tag{2-12}$$

where,

f denotes the frequency;

I_{Phase} denotes the ionospheric phase delay;

I_{Group} denotes the ionospheric group delay;

We can see that the absolute ionospheric delay for pseudo range and carrier phase have the same absolute value, but with different signs. Meanwhile, the ionospheric delay is inversely proportional to the square of the frequency, so usually the ionospheric-free model will be carried out with dual frequency observations and the equation can be expressed as:

$$\begin{aligned} L_3 &= \frac{f_1^2}{f_1^2 - f_2^2} L_1 - \frac{f_2^2}{f_1^2 - f_2^2} L_2 \\ P_3 &= \frac{f_1^2}{f_1^2 - f_2^2} P_1 - \frac{f_2^2}{f_1^2 - f_2^2} P_2 \end{aligned} \tag{2-13}$$

For single frequency users, there are several models which can be used, such as the GPS Klobuchar model (Klobuchar 1987), the NeQuick Model (Radicella 2009), the NTCM model (Jakowski et al. 2011) and IRI model (Bilitza 2001; Bilitza and Reinisch 2008). In this section, the GPS Klobuchar model is introduced:

$$\begin{aligned} I_{L1} &= A_1 + A_2 \cos\left[\frac{2\pi(t_{GPS} - A_3)}{A_4}\right] \\ A2 &= \sum_{n=0}^{3} \alpha_n \phi_m \\ A4 &= \sum_{n=0}^{3} \beta_n \phi_m \end{aligned} \tag{2-14}$$

where,

t_{GPS} denotes the GPS time;

I_{L1} denotes the ionospheric delay on $L1$;

A_1 denotes the constant night-time value;

A_2 denotes the amplitude;

A_3 denotes a constant phase shift fixed at 14:00 local time;

A_4 denotes the period of the cosine function;

α_n denotes satellite-transmitted coefficients of cubic polynomials for the amplitude;

β_n denote the cubic polynomials for the period of the model;

ϕ_m denotes the geomagnetic latitude of the ionospheric piercing point.

The mean ionospheric height is assumed to be 350 km and the mapping function is defined as following,

$$M(E)_{GPS} = 1 + 16(0.53 - E)^3 \tag{2-15}$$

where E denotes the elevation angle.

2.2.3 Troposphere effect

The effect of the neutral atmosphere is denoted as tropospheric refraction, tropospheric path delay, or simply tropospheric delay, including the contribution of both troposphere and stratosphere. The troposphere path delay can be expressed as,

$$T = \int (n-1) ds_0 \tag{2-16}$$

where,

n denotes the refractive index;

s_0 denotes the signal path;

T denotes the troposphere delay;

The refractivity can be expressed as follows:

$$N^{Trop} = 10^6 (n-1) \tag{2-17}$$

Then the troposphere delay can be rewritten as:

$$T = 10^{-6} \int N^{Trop} ds_0 \tag{2-18}$$

N^{Trop} can be divided into two parts as follows:

$$N^{Trop} = N_{dry}^{Trop} + N_{wet}^{Trop} \tag{2-19}$$

where,

N_{dry}^{Trop} denotes the dry portion;

N_{wet}^{Trop} denotes the wet portion from the water vapor;

Then the troposphere delay can be written as,

$$T = T_{dry} + T_{wet} = 10^{-6} \int N_{dry}^{Trop} ds_0 + 10^{-6} \int N_{wet}^{Trop} ds_0 \tag{2-20}$$

The troposphere delay can be expressed with the zenith dry component and zenith wet component,

$$T = M_{dry} T_{dry}^{z} + M_{wet} T_{wet}^{z} \tag{2-21}$$

where,

M_{dry} denotes the dry mapping function;

M_{wet} denotes the wet mapping function;

T_{dry}^{z} denotes the zenith dry component;

T_{wet}^{z} denotes the zenith wet component;

Several models have been developed to describe the corresponding zenith dry component and zenith wet component, such as the Hopfield (Hopfield 1969), Saastamoinen (Saastamoinen

1972), Black_Eisner (Black and Eisner 1984) and UNB (Collins and Langley 1996; Leandro et al. 2006). In this section, the Hopfield model is introduced:

$$T_{dry}^{z} = 10^{-6} \cdot k_1 \cdot \frac{P_s}{T_s} \cdot \frac{h_d - h_s}{5}$$
$$T_{wet}^{z} = 10^{-6} \cdot (k_3 + 273(k_2 - k_1)) \cdot \frac{e_s}{T_s} \cdot \frac{h_w - h_s}{5} \quad (2\text{-}22)$$

where,

P_s denotes the surface pressure in mbar at the user location;

T_s denotes the temperature in Kelvin at the user location;

h_s denotes the geodetic height;

e_s denotes the water pressure at the user location;

$k_1 = 77.6$;

$k_2 = 71.6$;

$k_3 = 3.747 \times 10^{-5}$;

$h_d = 40163 + 148.72(T_s - 273.16)$;

Afterwards, the Niell mapping function (Niell 1996) is introduced as:

$$M_{dry} = \frac{1+\dfrac{a_h}{1+\dfrac{b_h}{1+c_h}}}{\sin E+\dfrac{a_h}{\sin E+\dfrac{b_h}{\sin E+c_h}}} + \left[\frac{1}{\sin E} - \frac{1+\dfrac{a_{ht}}{1+\dfrac{b_{ht}}{1+c_{ht}}}}{\sin E+\dfrac{a_{ht}}{\sin E+\dfrac{b_{ht}}{\sin E+c_{ht}}}}\right] \times \frac{H}{1000}$$

$$M_{wet} = \frac{1+\dfrac{a_w}{1+\dfrac{b_w}{1+c_w}}}{\sin E+\dfrac{a_w}{\sin E+\dfrac{b_w}{\sin E+c_w}}} \tag{2-23}$$

where,

H denotes the orthometric height;

E denotes the elevation angle;

$a_{ht} = 2.53\times10^{-5}$;

$b_{ht} = 5.49\times10^{-5}$;

$c_{ht} = 1.14\times10^{-5}$;

a_h, b_h and c_h denote the dry delay coefficients;

a_w, b_w and c_w denote the wet delay empirical coefficients;

2.2.4 Sagnac effect

Sagnac effect is caused by the Earth rotation and the corrections need to be applied if the receiver and satellite positions are computed in the Earth-centered Earth-fixed reference frame. The Sagnac correction (Ashby 2004) can be calculated as:

$$Sagnac = \frac{1}{c}(r_r(t_A) - r^s(t_E)) \cdot (\omega \times r_r(t_A)) \tag{2-24}$$

where,

c denotes the speed of light in vacuum;

$r_r(t_A)$ denotes the receiver vector at the signal receiving epoch;

$r^s(t_E)$ denotes the satellite vector at the signal transmitted epoch;

ω denotes the Earth rotation rate;

If we assume

$$S = \frac{1}{2}(r^s(t_E) \times r_r(t_A)) \tag{2-25}$$

Then Sagnac can be written as the following equation,

$$Sagnac = \frac{2}{c} S \cdot \omega \tag{2-26}$$

2.2.5 Receiver phase center offset & phase center variation

The antenna Phase Center Offset (PCO) denotes the difference between the Antenna Reference Point (ARP) and the mean Antenna Phase Centre (APC), which is given for each carrier frequency. The azimuth- and elevation-dependent phase center variations (PCV) describe the differences between true phase center and mean phase center. The use of PCO and PCV is shown as the following shortened formulae (Rothacher 2016) are given:

$$\begin{aligned} phase\ center\ position &= ARP\ \ position + \\ &\quad PCO\ (given\ in\ a\ topocentric\ left\text{-}handed\ system: \\ &\quad north, east\ and\ up\ components) \\ observed\ distance &= geometric\ distance + \\ &\quad PCV\left(zenith, azimuth\right) + \\ &\quad other\ corrections \end{aligned} \tag{2-27}$$

The PCO correction can be expressed as:

$$\xi_{PCO} = -\mathbf{e}(\mathbf{A}\mathbf{r}_{PCO}) \tag{2-28}$$

where,

A denotes the direction vector to transfer the PCO from the NEU to XYZ frame;

$\mathbf{r}_{PCO}$ denotes the PCO vector, which can be found in the IGS antenna files;

e denotes the direction vector in the line of sight direction;

Then the antenna phase correction at the receiver side can be written as:

$$\xi_r = \xi_{PCO} + \xi_{PCV} \tag{2-29}$$

where,

ξ_r denotes the receiver phase center correction in the line-of-sight direction;

ξ_{PCO} denotes the receiver PCO projected in the line-of-sight direction;

ξ_{PCV} denotes the receiver PCV interpolated with the value from the IGS antenna files;

2.2.6 Satellite phase center offset & phase center variation

The satellite PCO is defined as the difference between the mean phase center and the mass center, while the PCV is a variation as a function of the direction of the outgoing signal. The use of satellite PCO and PCV (Rothacher 2016) is shown as:

$$\begin{aligned} phase\ center\ \ position &= \ CoM\ \ \ position + \\ &\quad PCO\left(given\ in\ the\ satellite\ body\ \ frame\right) \\ observed\ distance\ \ \ &= \ geometric\ distance + \\ &\quad PCV\left(nadir, azimuth\right) + \\ &\quad other\ corrections \end{aligned} \tag{2-30}$$

Similarly, the antenna phase correction at the satellite side can be expressed as:

$$\xi_s = \xi_{sPCO} + \xi_{sPCV} \tag{2-31}$$

where,

ξ_s denotes the satellite phase center correction in the line-of-sight direction;

ξ_{sPCO} denotes the satellite PCO projected in the line-of-sight;

ξ_{sPCV} denotes the satellite PCV interpolated with the value from the IGS antenna files;

2.2.7 Phase wind-up effect

Carrier phase wind-up is due to the electromagnetic nature of circularly polarized waves. Its effect on phase measurements is based on the relative orientation of satellite and receiver antennas, and the direction of the line of sight. The phase wind up correction (Wu *et al.*, 1992; Kouba, 2009) can be computed as:

$$\begin{aligned} dWindup_{Li} &= \lambda_{Li} sign[\mathbf{k} \cdot (\mathbf{D}' \times \mathbf{D})] \cos^{-1}\left(\frac{\mathbf{D}' \cdot \mathbf{D}}{|\mathbf{D}'||\mathbf{D}|}\right) \\ \mathbf{D}' &= \mathbf{x}' - \mathbf{k} \times (\mathbf{k} \times \mathbf{x}') - \mathbf{k} \times \mathbf{y}' \\ \mathbf{D} &= \mathbf{x} - \mathbf{k} \times (\mathbf{k} \times \mathbf{x}) - \mathbf{k} \times \mathbf{y} \end{aligned} \tag{2-32}$$

where,

$dWindup_{Li}$ denotes the phase wind up correction on frequency Li ;

$\mathbf{k}$ denotes the satellite to receiver unit vector;

$\mathbf{x}'$ and $\mathbf{y}'$ denote direction vectors from the satellite body frame;

$\mathbf{x}$ and $\mathbf{y}$ denote direction vectors from the receiver local frame in north and east direction.

2.2.8 Relativity effect

The relativistic effects in GNSS can be divided into two different categories: delays affecting the signal path due to the Earth's gravitational potential, and deviations of the satellite clock frequency due to relativistic effects (Ashby and Spilker 1996). The Shapiro effect is a delay of the satellite signal due to Earth's gravitational field, which causes a propagation delay due to space-time curvature. The Shapiro effect can be expressed as:

$$\delta_{Shapiro}^{rel} = \frac{2GM_E}{c^3} \ln\left(\frac{\left\|r^s\right\| + \left\|r_r\right\| + \rho_r^s}{\left\|r^s\right\| + \left\|r_r\right\| - \rho_r^s}\right) \tag{2-33}$$

where,

$\delta_{Shapiro}^{rel}$ denotes the Shapiro delay error (m);

c denotes the speed of light in vacuum;

GM_E denotes the gravitational constant of the Earth;

$\left\|r^s\right\|$ denotes the geocentric distance of satellite (m);

$\left\|r_r\right\|$ denotes the geocentric distance of receiver (m);

ρ_r^s denotes the geocentric distance between the satellite and receiver;

The onboard clocks will be affected by relativity due to Earth's oblateness, the relativity effect on satellite clocks can be calculated as:

$$\delta^{rel} = -\frac{2}{c^2}\sqrt{\mu a}(e\sin E) \tag{2-34}$$

where,

e denotes the eccentricity;

E denotes the eccentric anomaly of the satellite orbit;

a denotes the semimajor axis;

c denotes the speed of light in a vacuum;

There is alternative way to calculate the relativity effect on the clock, which is shown as:

$$\delta^{rel} = -\frac{2}{c^2}\boldsymbol{\rho}^s \dot{\boldsymbol{\rho}}^s \tag{2-35}$$

where,

$\boldsymbol{\rho}^s$ denotes the satellite geocentric coordinate vector;

$\dot{\boldsymbol{\rho}}^s$ denotes the satellite geocentric velocity vector;

c denotes the speed of light in vacuum;

2.2.9 Site displacement effect

The site displacement effects are due to various forces such as lunar and solar gravitation, ice loading, oceans loading and atmosphere loading. The Earth and its crust deforms due to lunar and solar gravitation, which is called solid Earth tide effect (Petit and Luzum 2010). The horizontal and vertical deformations can be modeled by a spherical harmonics expansion and associated physical parameters.

$$\begin{aligned}\Delta\hat{r}_s = \sum_{j=2}^{3}\frac{GM_j R_E^4}{GM_E R_j^3}\left\{h_2\cdot\hat{r}_r\left(\frac{3}{2}(\hat{R}_j\cdot\hat{r}_r)-\frac{1}{2}\right)+3l_2(\hat{R}_j\cdot\hat{r}_r)[\hat{R}_j-(\hat{R}_j\cdot\hat{r}_r)\cdot\hat{r}]\right\}\\ +\left[-0.025m\cdot\sin\phi\cdot\cos\phi\cdot\sin(\theta_g+\lambda)\right]\cdot\hat{r}_r\end{aligned} \tag{2-36}$$

where,

GM_E denotes the gravitation parameter of the Earth;

GM_j denotes the gravitation parameter of the Moon and the Sun;

$\hat{R}_j$ denotes the unit vector from the Earth center to the Moon or the Sun;

R_j denotes the magnitude of the vector from the Earth center to the Moon or the Sun;

$\hat{r}_r$ denotes the geocentric unit vector of the user location;

m denotes the order of the spherical harmonics;

ϕ, λ and θ_g denote the site latitude and longitude and the GMST.

h_2 and l_2 denote the nominal second degree Love and Sheba dimensionless numbers;

With latitude, h_2 and l_2 can be calculated as:

$$\begin{aligned} h_2 &= 0.6078 - 0.0006[(3\sin^2\varphi - 1)/2] \\ l_2 &= 0.0847 - 0.0002[(3\sin^2\varphi - 1)/2] \end{aligned} \tag{2-37}$$

The magnitude of ocean tide is one order smaller than that of the solid earth tides. With semidiurnal and diurnal periods, the ocean tide effects can be neglected for static positioning over daily periods and the stations far from the coast. The ocean tides effect (Gérard and Luzum 2010) can be calculated by:

$$\Delta c = \sum_{j=1}^{11} A_{cj} \cos(\chi_j(t) - \phi_{cj}) \tag{2-38}$$

where,

Δc denotes the displacement vector due to ocean loading;

j denotes the number of tide waves;

χ_j denotes linear combinations of the fundamental astronomical arguments;

A_{cj} denotes the amplitude, which can be calculated using the ocean loading model;

ϕ_{cj} denotes the amplitude, which can be calculated using the ocean loading model;

The pole tides are caused by the polar motion and can be calculated as follows,

$$\Delta r_p = \begin{cases} -9\cos(2\phi)[(x_p - \bar{x}_p)\cos\lambda - (y_p - \bar{y}_p)\sin\lambda] \\ 9\sin(\phi)[(x_p - \bar{x}_p)\sin\lambda + (y_p - \bar{y}_p)\cos\lambda] \\ -33\sin(2\phi)[(x_p - \bar{x}_p)\cos\lambda - (y_p - \bar{y}_p)\sin\lambda] \end{cases} \quad (2\text{-}39)$$

where,

x_p and y_p denote the polar motion terms;

$\bar{x}_p$ and $\bar{y}_p$ denote the mean polar motion terms.

2.3 State Estimation

For parameter estimation, dual frequency signals are used to remove the effect of the first order ionosphere refraction, while the real-value carrier phase ambiguities are estimated from the measurement model along with the residual troposphere error, the receiver clock offset and the position coordinates. By applying the Taylor series expansion, the observation equations can be expressed as:

$$\begin{aligned} \delta\rho &= \rho - \rho_0 \\ &= H(x - x_0) + v \\ &= H\delta x + v \end{aligned} \quad (2\text{-}40)$$

where,

$\delta\rho$ denotes the measurement misclosure vector;

ρ denotes the observed measurement;

ρ_0 denotes the function with x_0;

x_0 denotes the approximate initial value;

x denotes the true value;

δx denotes the estimated correction for x_0;

v denotes the residual.

For single-epoch solution, the δx can be estimated with the following equation,

$$\delta x = (H^T P H)^{-1} H^T P \delta z \tag{2-41}$$

In which, P is the weighting matrix for observations, which reflects the relative uncertainty among the observations and has the following relation with Q_{PP}.

$$P = Q_{PP}^{-1} \tag{2-42}$$

By applying the error propagation law, the covariance matrix for x can be expressed as:

$$\begin{aligned} Q_{xx} &= \left[(H^T P H)^{-1} H^T P\right] \cdot Q_{PP} \cdot \left[(H^T P H)^{-1} H^T P\right]^T \\ &= (H^T Q_{PP}^{-1} H)^{-1} \end{aligned} \tag{2-43}$$

The diagonal elements are the variance for the estimated states and the off-diagonal elements denote the covariance between estimates. By assuming all observations are of the same quality with the same standard deviation δ.

$$Q_{PP} = \delta^2 I \tag{2-44}$$

then the Q_{xx} can be written as:

$$Q_{xx} = \delta^2 (H^T H)^{-1} \tag{2-45}$$

The $(H^T H)^{-1}$ is a function of the satellite receiver geometry. The Geometry Dilution of Position (GDOP) is the trace of the corresponding receiver position states and receiver clock in $(H^T H)^{-1}$ and the value is usually larger than 1. The GDOP is reduced to Positioning DOP (PDOP) by removing the receiver clock components and turns to Vertical DOP (VDOP) by omitting the horizontal components. Similarly, the Horizontal DOP (HDOP) can be calculated. The Time DOP (TDOP) only counts for the receiver clock components. The smaller the DOP, the better the geometry. User Equivalent Range Error (UERE) is calculated by combing satellite clock and ephemeris error, ionospheric error, troposphere error, receiver noise, and multipath together. The UERE contains two parts – SISRE referring to the satellite orbit and clock errors and the User Equipment Error (UEE) regarding the receiver errors and atmosphere errors (Teunissen and Montenbruck 2017). The relation can be written as:

$$UERE = \sqrt{SISRE^2 + UEE^2} \tag{2-46}$$

Both the DOP and UERE are fundamental to understand the positioning errors and the approximate relation can be expressed as:

$$Err = DOP \times UERE \tag{2-47}$$

However, PPP typically takes advantage of previous information to facilitate convergence, so Kalman filter is usually applied in the state estimation process. The Kalman filter is designed as a recursive form to compute the updated state estimate $\hat{x}_k^+$ by using a priori estimate $\hat{x}_k^-$ and the measurements z_k, which is expressed as:

$$\hat{x}_k^+ = K_k^x \hat{x}_k^- + K_k^z z_k \tag{2-48}$$

where K_k^x and K_k^z can be computed by minimizing the loss function. After derivation, the solution gives,

$$\begin{aligned} \hat{x}_k^+ &= \hat{x}_k^- + K_k(z_k - H_k\hat{x}_k^-) \\ P_k^+ &= (I - K_k H_k)P_k^- \\ K_k &= P_k^- H_k^T (H_k P_k^- H_k^T + R_k)^{-1} \end{aligned} \tag{2-49}$$

where

P_k denotes the variance matrix of the state;

K_k denotes the gain matrix;

R_k denotes the variance matrix of observations.

The above equations define the measurement update loop only, and the prediction loop between epochs is realized as follows,

$$\begin{aligned} \hat{x}_{k+1}^- &= \Phi_{k,k+1}\hat{x}_k^+ \\ P_{k+1}^- &= \Phi_{k,k+1}P_k^+\Phi_{k,k+1}^T + Q_k \end{aligned} \tag{2-50}$$

where

$\Phi_{k,k+1}$ denotes the transition matrix;

Q_k denotes process noise matrix.

Note that process noise and measurement noise are both assumed to be white and uncorrelated with each other.

2.4 Summary

Section 2.1 discussed the PPP observation equations regarding pseudo range and carrier phase observations. Section 2.2 introduces the PPP related error sources and corresponding mitigation methods, such as the satellite orbit and clock error, ionosphere error, troposphere error, Sagnac

effect, receiver PCO and PCV, satellite PCO and PCV, phase wind-up, relativity effects, solid Earth tides effect, ocean tides effect and pole tides effect. The state estimation is addressed in Section 2.3 regarding to Kalman filter and some evaluation indicators are introduced, such as GDOP, HDOP, VDOP and UERE.

CHAPER THREE: DESIGN OF A NEW REAL-TIME PPP SYSTEM

In this chapter, the system architecture of the new real-time PPP system is introduced in Section 3.1 for the server end, communication end and user end. Meanwhile, the compatibility between the new real-time PPP system and current real-time PPP system is discussed. The functional modules for each component are then presented in detail accordingly in Section 3.2 to 3.4. The IP related function modules in the whole system are addressed in Section 3.5.

3.1 Real-time PPP System Components

The system components of the current real-time PPP systems are illustrated as Fig. 3-1, current real-time PPP systems are realized by applying the real-time orbit and clock corrections on broadcast ephemeris.

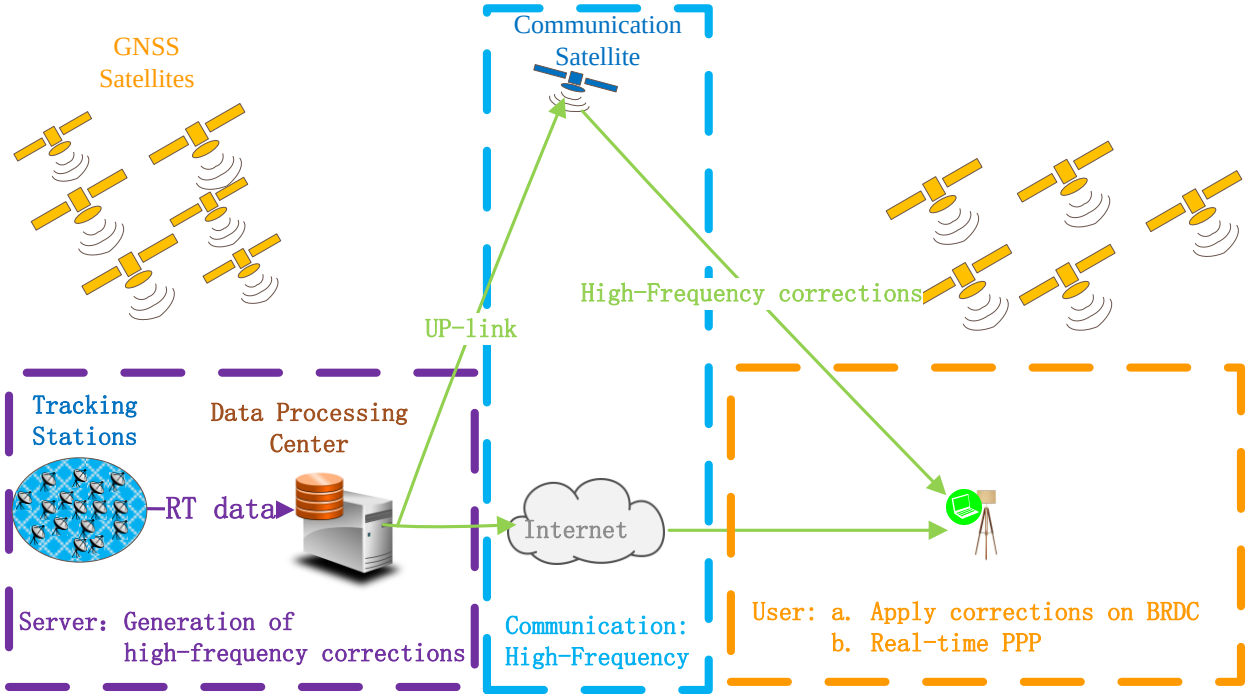

Figure 3-1 System components of the current real-time PPP systems

First and foremost, real-time network GNSS raw observation data of globally distributed reference stations need to be transmitted to the processing center at the server end to generate real-time orbit and clock corrections. The PPP users can receive and apply the corrections on broadcast ephemeris to obtain high-precision satellite orbit and clock products with the mathematic models introduced in Section 2.1.

The new real-time PPP system also consists of three primary components: the server end, the communication end and the user end (Gao et al. 2017). The system components and functions of the new real-time PPP system is shown in Fig. 3-2.

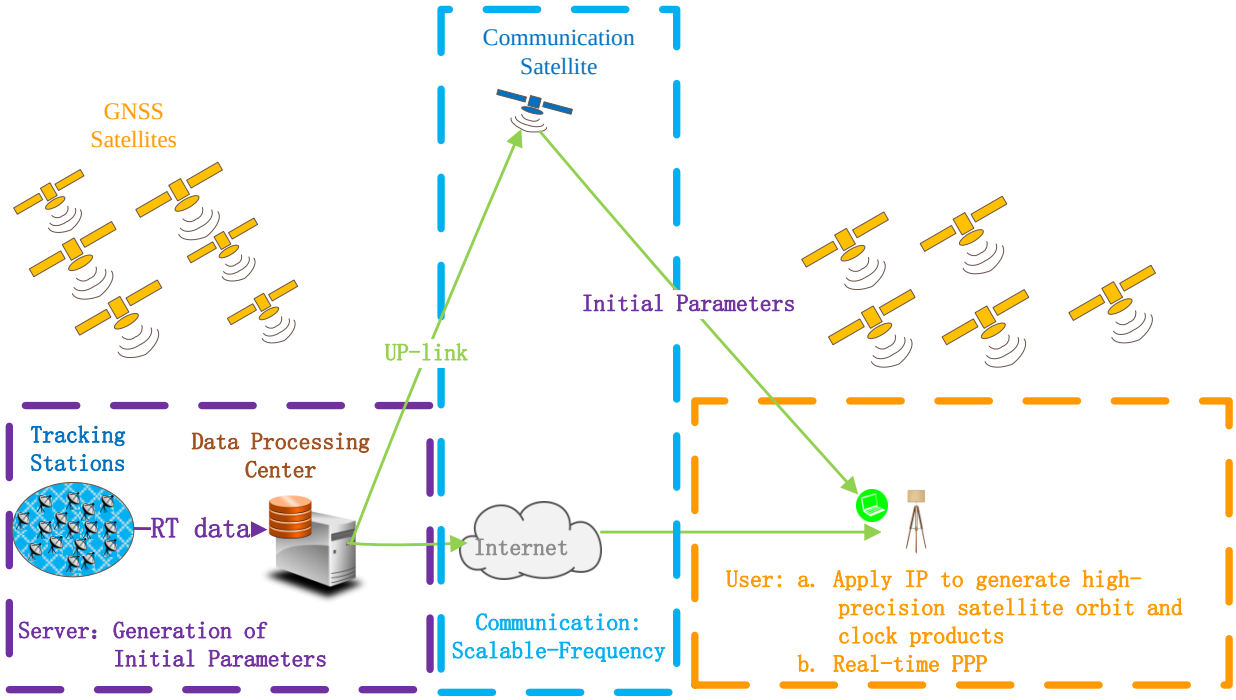

Figure 3-2 System components of the new real-time PPP systems

The main difference with the current real-time PPP is the products distributed in real-time. In the proposed real-time PPP system, IP products are generated, transmitted and applied. Accordingly, the generation process of the IP products at the server end will be different from current real-time PPP systems. Meanwhile, there are specific function modules at the user end to

generate high-precision satellite orbit and clock products based on IP. For the new real-time PPP system, the update rates can be scalable, and mitigation of Internet connection outages can be realized with the accurate physical models behind the IP products.

There are several functions that must be implemented for all the above-mentioned components to realize the new real-time PPP system. Real-time network GNSS raw observation data of globally distributed reference stations need to be transmitted to the server end to generate IP products. Alternatively, the IGS RTS products can be collected and applied to the generation of the orbit and clock IP products. Once generated at the server end, the IP products will be disseminated according to the requests of registered users via communication networks, such as communication satellites or the Internet. After receiving the real-time IP products, PPP users can generate high-precision satellite orbit and clock corrections at desired epoch times.

For each satellite, the orbit IP includes the satellite position, velocity and SRP, while the satellite clock IP consists of the polynomial terms and periodic terms. To update the current real-time PPP to the proposed real-time PPP system, three different ways can be carried out regarding to the transmitted message content：

a. The first method is directly using IP to replace real-time corrections, so the generation of high precision orbit and clock products at the user end need to be replaced accordingly;
b. The second method is adding the IP on top of current real-time corrections, so PPP user can choose whether to apply real-time corrections or IP products. Typically, the real-time corrections are applied in the normal situations with good connection of the server end and IP products are used when outages happen. This mode is called “loosely coupled mode” of the IP and RTS.

c. The third method transmits IP products in an extended SSR formats and only SRP and periodic terms are added to current RTS. The PPP users can choose to use RTS or extended RTS, which is similar to the second method. Meanwhile, the use of extended RTS is compatible with current RTS. This mode is called the “tightly coupled mode” of the IP and RTS, which is extensively tested in Chapter Six.

3.2 Function Modules of Server End

The function modules of the server end are demonstrated regarding the getting input data, quality check, IP generation, IP broadcasting and system logs generation. The detailed functions of each module are shown in Fig. 3-3 and explained in the subsequent text.

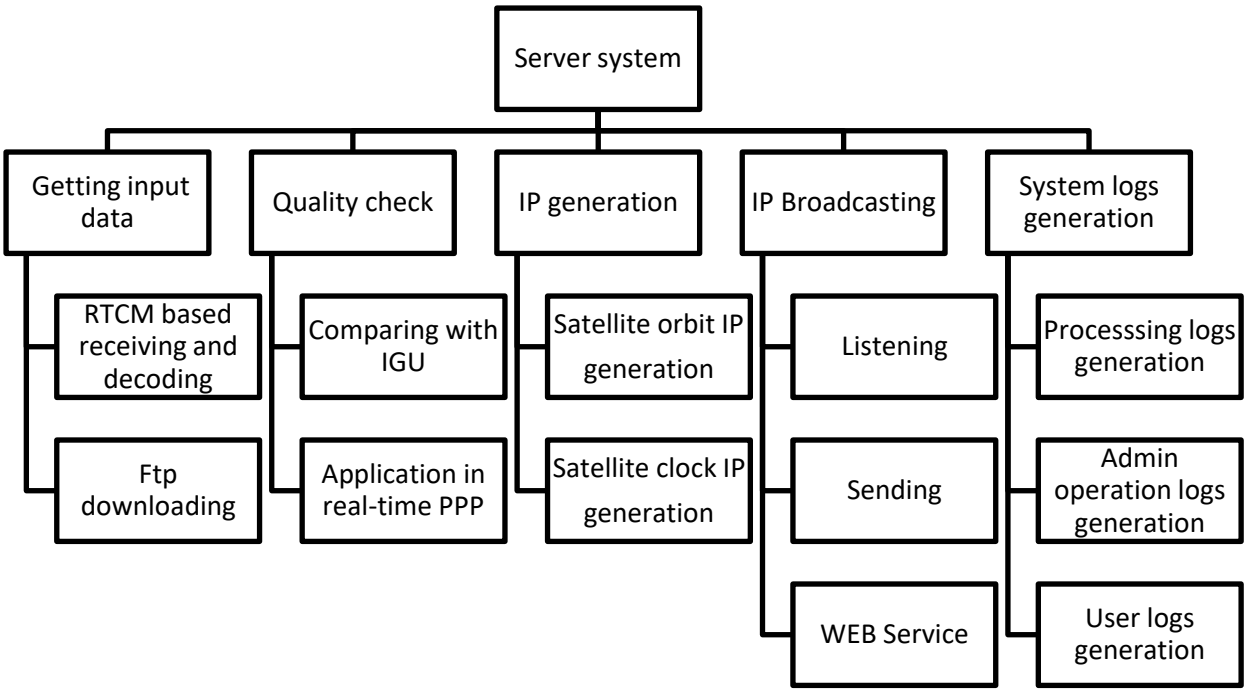

Figure 3-3 System function chart of server end for the new real-time PPP system

a. Getting input data module

This module is mainly responsible for obtaining input data either by receiving the RTCM based streams or downloading through ftp. The input data can be divided into four main types. The first type is the ephemeris information, such as the broadcast ephemeris, satellite orbit and clock corrections from IGS RTS and IGU products; the second type is the GNSS raw observations encoded in RTCM format; the third type includes the reference coordinates of the IGS stations derived from Scripps Orbit and Permanent Array Center through ftp; The fourth type is auxiliary information such the antenna file, Earth orientation parameters tables, and the lunar and solar ephemeris, which can be downloaded through ftp.

b. Quality check module

This module checks for the IGS RTS products and the generated IP products. The satellite orbit and clock prediction based on IP will be carried out in the server end as well to ensure integrity. The first check is to compare with the IGU products for each satellite, the specific satellite will be excluded from the messages once the errors surpassed the threshold. The second check applies the satellite orbit and clock products to real-time PPP in the server end to investigate the overall effects of visible satellites. The availability and latency of the IGS RTS products are continuously monitored as well.

c. IP generation module

This module is primarily used for the generation of IP products. For the orbit IP generation, the dynamic models and the numerical integrators are the crucial elements; for the clock IP generation, the polynomial terms and the periodic terms will be

extracted after the pre-processing. More details about this module will be discussed latterly.

d. IP broadcasting module

This module is developed for the broadcasting of IP products and other auxiliary information to registered users according to demands. Both the listening and sending functions are realized in the server end for communication. For the users, correct commands must be sent to the server to build the connection and request the IP products, which are encoded in self-designed format concerning communication load. Furthermore, the user management function is realized based on web service to ensure only the registered users can obtain the valid information.

e. System logs generation module

The system logs generation module is used to store critical information, which can be used for debugging. With continuous operation of the server end, some crucial information, such as processing logs, admin operation logs and user operation logs, are stored in the database for any potential uses.

3.3 Function Modules of Communication End

The current communication module of the new real-time PPP system is Internet-based and realized by TCP socket. First, the registered user must build the connection with the server end by sending the message including public internet protocol address and port number. To maintain simplicity and consistency, the Internet protocol address of the server end is set as fixed. After the successful handshaking connection, the user needs to send another request to the server end for IP products. The server end will respond with the corresponding IP products to the user if the

received request is included in the pre-defined command pools; otherwise, a notice message of "The request isn't correct" will be sent. The diagram of the communication between user and server is shown in Fig. 3-4. The new real-time PPP system can accommodate multiple real-time users simultaneously on either one device or separate devices, such as a PC or Raspberry Pi. For different users, the update-rate of IP products can be different according to the requests of various applications.

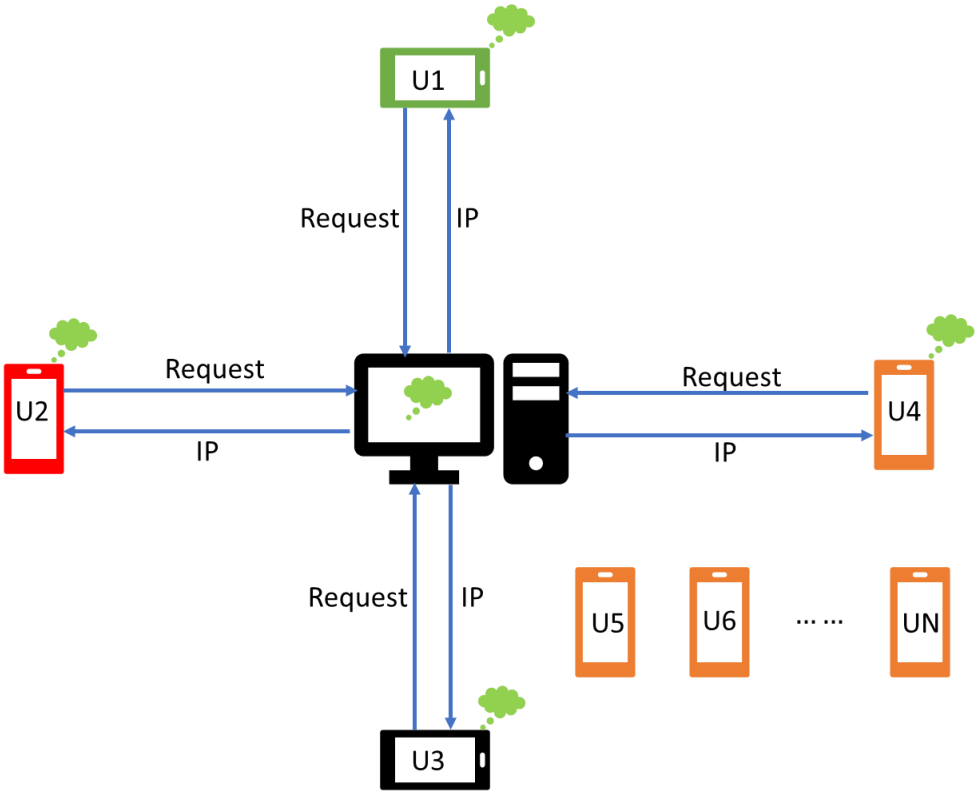

Figure 3-4 Communication end for the real-time PPP system

3.4 Function Modules of User End

For the user end of the new real-time PPP system, there are six main function modules regarding system settings, observation decoding, ephemeris calculation, errors mitigation, state estimation and system output and display, which are shown in Fig. 3-5.

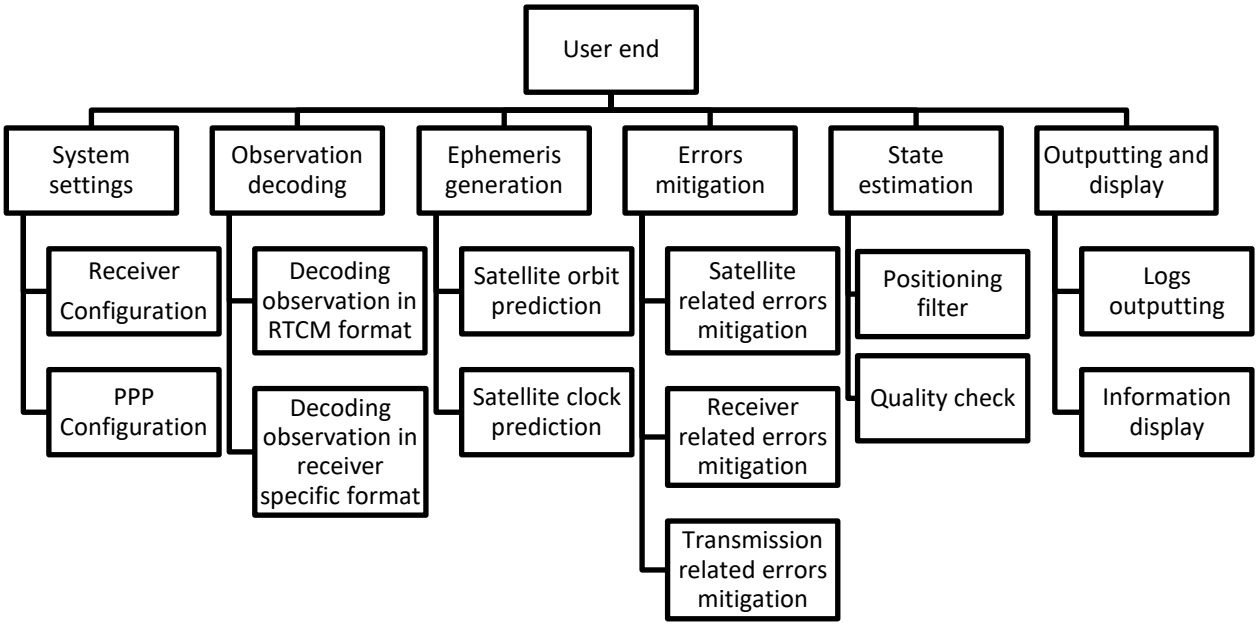

Figure 3-5 Function structure of user end of real-time PPP system

a. System settings module

This module is primarily for the realization of the settings at the user end, including the receiver configuration and PPP configuration, such as the receiver type, port number, bitrate, stop bits, flow control, update rate, elevation mask, excluded satellite PRN, output directory and so on. Currently, the receiver configuration can be set in the user GUI while the PPP configuration is realized in one configuration file.

b. Observation decoding module

The key feature of this module is decoding of real-time GNSS observations both in the RTCM formats and receiver specific formats. Even though the discussions are focused on GPS in this thesis, the observation decoding is designed and implemented for multi-GNSS PPP.

c. Ephemeris generation module

This module is responsible for the ephemeris generation, in which the satellite clock and orbit are calculated separately based on the IP products.

d. Errors mitigation module

This module realizes mitigation of the error sources in PPP, namely the satellite-related errors, receiver related errors and transmission related errors. The detailed methods are introduced in Chapter Two.

e. State estimation module

This estimation module is the crucial part at the user end, which mainly realizes the positioning filter to obtain accurate position results; meanwhile, the quality check procedures are implemented here, such as outlier detection, cycle slip detection and residual check.

f. Outputting and display module

This module is used for outputting and displaying results and useful information. Apart from the positioning results, the cycle slip information, used satellite number and DOP are also included in the system output logs. In the displaying part, the GUI is designed for user interactive operations, which will be introduced in detail in Chapter Six.

3.5 IP-Related Function Modules

The IP-related function modules are of great importance throughout the whole system and are explained here regarding satellite orbit and clock IP generation (server end), satellite orbit and clock prediction based on IP (user end). As shown in Fig. 3-6, the IP-related module consists of four components: satellite orbit IP generation at the user end, satellite clock IP generation at the user end, satellite orbit generation at the server end and satellite clock offset generation at the server end. The functions in each component are explained below:

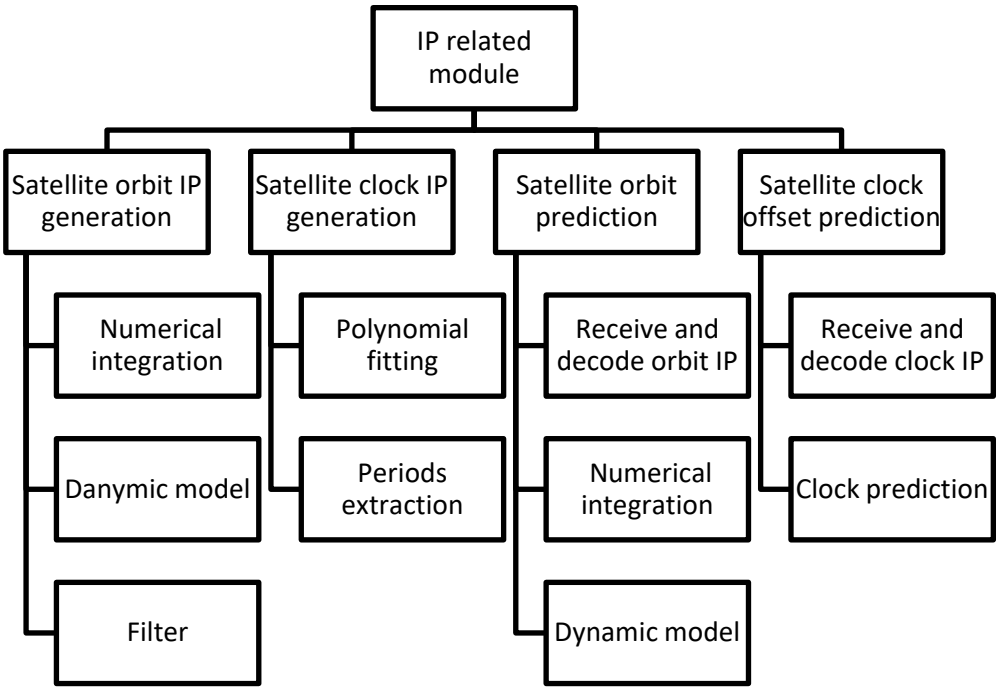

Figure 3-6 Function structure of the satellite orbit and clock part

a. Satellite orbit IP generation (Server end)

The numerical integration algorithms including the Runge-Kutta (single-step method) and Adams-Bashforsh-Moulton (multi-step method) are applied. The dynamic models of the satellites are also implemented, including the Earth gravitation, the gravitation of the Moon and Sun, and Solar Radiation Pressure (SRP). The estimation is then executed

to generate the orbit IP at specific reference epoch. The details will be introduced in Section 4.1.

b. Satellite clock IP generation (Server end)

For satellite clock IP generation, the polynomial fitting is of crucial importance due to the characters of atomic clocks onboard GPS satellites. The effects of the periodic terms need to be considered to improve the prediction further. The details will be introduced in Section 4.2.

c. Satellite orbit generation based on orbit IP (User end)

The satellite orbit IP is first received through the internet and decoded. Numerical integration will then be carried out based on the same dynamic models applied at the server end. Finally, the interpolation function will be called to calculate satellite position at the specific time. The details will be introduced in Section 5.1.

d. Satellite clock offset generation based on clock IP (User end)

The satellite clock IP is first received through the internet and decoded. Then clock offsets prediction is then implemented with the same clock model applied at server end to maintain consistency. Finally, the linear interpolation function will be carried out to calculate the satellite clock offsets at the specific time. The details will be introduced in Section 5.2.

3.6 Summary

In this chapter, the design of a new real-time PPP system is introduced in terms of server end, user end and communication end. For each component, the function modules are presented and explained. For the server end, the function modules include obtaining input data, quality check,

IP generation, IP broadcasting and system logs generation. For the used end, there are six main function modules, including system settings, observation decoding, ephemeris calculation, errors mitigation, state estimation and system output and display. For the communication part, the user needs to build the connection with the server firstly and then send the correct request messages to the server through the Internet to ask for IP products, afterward, the server will respond according to the request messages. As we can know that the IP related part is the key innovation, so the IP related modules throughout the whole system are explained together, including the generation of satellite orbit IP and clock IP, and the orbit and clock prediction based on IP.

CHAPER FOUR: SATELLITE ORBIT AND CLOCK IP GENERATION AT SERVER END

Satellite orbit and clock products are the two crucial elements for PPP. In this chapter, the generation of satellite orbit and clock IP at the server end are introduced separately. For the orbit IP generation, there are four parts - the forces on satellite, variation equations, numerical integrator and estimation of the orbit IP. For the clock IP generation, current atomic clocks onboard GPS satellites are introduced. The state-of-art prediction models are discussed and a new prediction model based on IGS RTS products is proposed.

4.1 Satellite Orbit IP Generation at Server End

4.1.1 Primary forces acting on the GPS satellites

The main forces acting on GPS satellites include Earth gravitation, lunar and solar gravitation, solid Earth tide, ocean tide and solar radiation pressure, which are introduced as follows:

4.1.1.1 Earth gravitation

Earth's gravity dominates the orbit of the GPS satellites. The basic orbit motion can be derived from Newton's laws of gravity.

$$\ddot{r} = G\frac{M}{r^3}\mathbf{r} \tag{4-1}$$

where,

$\ddot{r}$ denotes the force between the masses;

G denotes the gravitational constant;

M denotes the Earth mass;

r denotes the vector from the Earth center to the object.

It is convenient to use gravity potential and the gradient of gravity potential for the derivation, which can be expressed as follows,

$$\begin{aligned} \ddot{r} &= \nabla U \\ U &= GM\frac{1}{r} \end{aligned} \tag{4-2}$$

where,

∇U denotes the gradient of gravity potential;

U denotes the gravity potential;

With the above equation, the total potential of the Earth can be calculated by summing up the contributions from individual mass elements $dm = \rho(s)d^3s$ as the following equation,

$$U = G\int \frac{\rho(s)d^3s}{|r-s|} \tag{4-3}$$

where,

$\rho(s)$ denotes the density at a point s inside the Earth;

$|r-s|$ denotes the satellite's distance from this place.

The expansion in spherical harmonics is used to calculate the integral, which can be expended in a series of Legendre polynomials.

$$\begin{aligned} \frac{1}{|r-s|} &= \frac{1}{s}\sum_{n=0}^{\infty}\left(\frac{s}{r}\right)^n P_n(\cos\gamma) \\ P_n(\mu) &= \frac{1}{2^n n!}\frac{d^n}{du^n}(u^2-1)^n \end{aligned} \tag{4-4}$$

where,

$P_n(\mu)$ denotes the Legendre polynomial of degree n;

γ denotes the angle between r and s.

With longitude λ and geocentric latitude ϕ, the Earth's gravity potential can be written as:

$$U = \frac{GM}{r}\sum_{n=0}^{\infty}\sum_{m=0}^{n}\frac{R^n}{r^n}P_{nm}(\sin\phi)(C_{nm}\cos(m\lambda) + S_{nm}\sin(m\lambda)) \tag{4-5}$$

where,

U denotes the gravitational potential;

G denotes the earth Newton's universal gravitation constant;

M denotes the mass of the earth;

r denotes the distance from the earth to the point (p);

R denotes the mean equatorial radius of the Earth;

n denotes the degree of gravity field expansion;

m denotes the order of gravity field expansion;

P_{nm} denotes the associated Legendre polynomial;

ϕ denotes the geocentric latitude;

λ denotes geocentric longitude;

C_{nm} and S_{nm} denote the spherical harmonic coefficients.

4.1.1.2 Lunar and solar gravitation

The equation for the third body gravitation on GPS satellites can be written as,

$$a_i = -GM_i\left(\frac{r - r_i}{\left\|r - r_i\right\|^3} + \frac{r_i}{\left\|r_i\right\|^3}\right) \tag{4-6}$$

where,

M_i denotes the mass of the perturbing celestial body i;

r_i denotes the geocentric position vector of the celestial body i;

r denotes the geocentric position vector of the perturbing satellite i.

The second term on the right-hand side denotes the perturbing acceleration of the celestial body. The Jet Propulsion Laboratory (JPL) provides a series of solar system ephemerides in the form of Chebyshev approximations such as Development Ephemerides (DE), which are publicly available and have been the standard for high-precision planetary and lunar coordinates. For the position calculation of the Sun and Moon, the DE 405 or DE 421 (Folkner et al. 2008) can be used.

4.1.1.3 Solid Earth tide

The computation of the tidal contributions to the geopotential coefficients is most efficiently done by a three-step procedure (Gérard and Luzum 2010).

$$\Delta\bar{C}_{nm} - i\Delta\bar{S}_{nm} = \frac{k_{nm}}{2n+1}\sum_{j=2}^{3}\frac{GM_j}{GM_\oplus}\left(\frac{\mathrm{R_e}}{r_j}\right)^{n+1}\bar{P}_{nm}(\sin\Phi_j)e^{-im\lambda_j} \tag{4-7}$$

where,

k_{nm} denotes the nominal Love number for degree n and m;

$\mathrm{R_e}$ denotes the equatorial radius of the Earth;

$GM_\oplus$ denotes the gravitation parameter for the Earth;

GM_j denotes the gravitation parameter for the celestial body j;

r_j denotes the geocentric distance of the celestial body j;

Φ_j denotes the body-fixed geocentric latitude of the celestial body j;

λ_i denotes the body-fixed east longitude (from Greenwich) of the celestial body j;

While the contribution from a number of tidal constituents belonging to the respective bands can be written as:

$$\begin{aligned} &\mathrm{Re}\sum_{f(2,0)}(A_0\delta k_f H_f)e^{i\theta f} = \sum_{f(2,0)}[(A_0 H_f \delta k_f^R)\cos\theta_f - (A_0 H_f \delta k_f^I)\sin\theta_f] \\ &\Delta\bar{C}_{2m} - i\Delta\bar{S}_{2m} = \eta_m \sum_{f(2,m)}(A_m \delta k_f H_f)e^{i\theta f}\,(m=1,2) \end{aligned} \tag{4-8}$$

where,

$$\begin{aligned} &A_0 = \frac{1}{\mathrm{R}_e\sqrt{4\pi}} = 4.4228\times10^{-8}m^{-1} \\ &A_m = \frac{(-1)^m}{\mathrm{R}_e\sqrt{8\pi}} = (-1)^m(3.1274\times10^{-8})m^{-1}, (m\neq 0) \\ &\eta_1 = -i, \eta_2 = 1 \end{aligned} \tag{4-9}$$

δk_f denotes the difference between k_f and k_{2m} plus a contribution from ocean load;

δk_f^R denotes the real part of δk_f;

δk_f^I denotes the imaginary part of δk_f;

H_f denotes the amplitude of the term at a frequency f;

$$\begin{aligned} &\theta_f = \bar{n}\cdot\bar{\beta} = \sum_{i=1}^{6} n_i\beta_i or \\ &\theta_f = m(\theta_g + \pi) - \bar{N}\cdot\bar{F} \end{aligned} \tag{4-10}$$

where,

$\bar{\beta}$ denotes the six-vector of Doodson's fundamental arguments;

$\bar{n}$ denotes the six-vector of multipliers n_i;

$\bar{F}$ denotes the five-vector of fundamental arguments F_j;

$\bar{N}$ denotes the five-vector of multiples N_j;

θ_g denotes the Greenwich Mean Sidereal Time expressed in angle unit;

4.1.1.4 Ocean tide

The dynamic effects of ocean tides can be expressed as periodic variations in the normalized Stokes' coefficients of degree n and order m (Gérard and Luzum 2010), which can be expressed as:

$$[\Delta\bar{C}_{nm} - i\Delta\bar{S}_{nm}](t) = \sum_f \sum_+^- (C^{\pm}_{f,nm} \mp iS^{\pm}_{f,nm}) e^{\pm i\theta_f(t)} \tag{4-11}$$

where,

$C^{\pm}_{f,nm}$ and $S^{\pm}_{f,nm}$ denote the geopotential amplitudes for the tide constituent f;

$\theta_f(t)$ denotes the argument of the tide constituent f;

The geopotential harmonic amplitude can be expressed with largest wave ($C^{\pm}_{1,nm}$, $S^{\pm}_{1,nm}$) and second largest wave ($C^{\pm}_{2,nm}$, $S^{\pm}_{2,nm}$):

$$\begin{aligned} C^{\pm}_{f,nm} &= \frac{\dot{\theta}_f - \dot{\theta}_1}{\dot{\theta}_2 - \dot{\theta}_1} \cdot \frac{H_f}{H_2} C^{\pm}_{2,nm} + \frac{\dot{\theta}_2 - \dot{\theta}_f}{\dot{\theta}_2 - \dot{\theta}_1} \cdot \frac{H_f}{H_1} C^{\pm}_{1,nm} \\ S^{\pm}_{f,nm} &= \frac{\dot{\theta}_f - \dot{\theta}_1}{\dot{\theta}_2 - \dot{\theta}_1} \cdot \frac{H_f}{H_2} S^{\pm}_{2,nm} + \frac{\dot{\theta}_2 - \dot{\theta}_f}{\dot{\theta}_2 - \dot{\theta}_1} \cdot \frac{H_f}{H_1} S^{\pm}_{1,nm} \end{aligned} \tag{4-12}$$

4.1.1.5 Solar radiation pressure

Solar radiation pressure is the most significant perturbation apart from the gravitational forces for GPS satellites. It is very complicated to model SRP due to its dependence on satellite

structure, dimensions, optical surface properties and altitude. Nominal altitude of the GPS satellites meets two requests (Kouba 2009a):

a. The navigation antenna points to the center of the Earth.

b. The solar panels are perpendicular to the direction of the Sun.

Currently, the GPS SRP models can be summarized into two categories, namely the physical models derived from satellite surface properties and the empirical models derived from long history data analysis. For the first type, ROCK4 and ROCK42 models are designed for the Block I and Block II/IIA satellites. More advanced models such as ROCK-T series (T10, T20) are developed to include the additional thermal re-radiation of the satellites (Fliegel *et al.*, 1992). Empirical SRP models are used in the orbit determination process and the most commonly used empirical model is CODE (Center for Orbit Determination in Europe) orbit model (ECOM) at the University of Bern. The reference frame consists of three direction vectors, e_D pointing from the satellite to the Sun, the second vector e_Y pointing along the solar panel axis and e_B completing a right-handed triad. All three vectors can be derived by:

$$\begin{aligned} e_D &= \frac{r_s - r}{\|r_s - r\|}, \\ e_Y &= \frac{e_D \times r}{\|e_D \times r\|}, \\ e_B &= e_D \times e_Y \end{aligned} \tag{4-13}$$

where,

r denotes the geocentric position vector of the satellite;

r_s denotes the geocentric position vector of Sun.

The SRP in all three directions consists of one constant term and a harmonic sine-cosine-term with the latitude μ of the satellite (Beutler et al. 1994).

$$\begin{aligned} D(u) &= d \cdot (\lambda \cdot D_0 + D_c \cos\mu + D_s \sin\mu) \\ Y(u) &= d \cdot (Y_0 + Y_c \cos\mu + Y_s \sin\mu) \\ B(u) &= d \cdot (B_0 + B_c \cos\mu + B_s \sin\mu) \end{aligned} \tag{4-14}$$

where,

d denotes the theoretical value of the SRP acceleration calculated from the ROCK model;

λ denotes the Earth shadow factor;

And in the orbit determination or fitting process, the nine parameters D_0 , D_c , D_s , Y_0 , Y_c , Y_s , B_0 , B_c and B_s are estimated along with the satellite position and velocity. Due to the correlation between the periodic terms in D and Y direction, the ECOM model with 5 parameters (Springer and géodésique 2000) are brought out by some scholars.

The SRP acceleration in geocentric cartesian coordinate system can be presented as follows,

$$\ddot{r}_{srp} = \frac{a_u^2}{|r_s - r|} \cdot [D(\mu) \cdot e_D + Y(\mu) \cdot e_Y + B(\mu) \cdot e_B] \tag{4-15}$$

where，

a_u represents the length in astronomical unit;

r_s and r denote the positions of the Sun and satellite in an inertial system;

Another series of SRP models are developed by JPL, such as the GSPM97, GSPM04, GSPM10 and GSPM13 (Desai et al. 2014). The GSPM can be expressed as a function of Earth–satellite–Sun angle,

$$
\begin{aligned}
X(\varepsilon) &= X_1 \sin\varepsilon + X_2 \sin 2\varepsilon + X_3 \sin 3\varepsilon + X_5 \sin 5\varepsilon + X_7 \sin 7\varepsilon \\
Y(\varepsilon) &= Y_1 \cos\varepsilon + Y_2 \cos 2\varepsilon \\
Z(\varepsilon) &= Z_1 \cos\varepsilon + Z_3 \cos 3\varepsilon + Z_5 \cos 5\varepsilon
\end{aligned}
\tag{4-16}
$$

For the eclipse, both conical and cylinder model will be briefly introduced here.

First, we can calculate

$$
\begin{aligned}
s_\odot &= r_\odot - r_B \\
s &= r - r_B
\end{aligned}
\tag{4-17}
$$

where,

$r_\odot$ denotes the coordinate vector of the Sun in the inertial frame;

r denotes the coordinate vector of the satellite in the inertial frame;

r_B denotes the coordinate vector of the Earth in the inertial frame;

$s_\odot$ denotes the coordinate vector of the Sun with respect to the Earth in the inertial frame;

s denotes the coordinate vector of the satellite with respect to the Earth in the inertial frame;

For the conical model (Montenbruck and Gill 2000a), the following parameters need to be calculated,

$$
\begin{aligned}
a &= \arcsin\frac{R_\odot}{|r_\odot - r|} \\
b &= \arcsin\frac{R_B}{s} \\
c &= \arccos\frac{-s^T(r_\odot - r)}{s|r_\odot - r|}
\end{aligned}
\tag{4-18}
$$

where,

$R_{\odot}$ denotes the radius of the Sun;

R_B denotes the radius of the Earth;

a denotes the apparent radius of the Sun;

b denotes the apparent radius of the Earth;

c denotes the apparent separation of the Sun and the Earth;

The occultation occurs when

$$|a-b| < c < a+b \tag{4-19}$$

Then the occulted area can be written as following,

$$\begin{aligned} A &= a^2 \arccos(x/a) + b^2 \cdot \arccos((c-x)/b) - cy \\ x &= \frac{c^2 + a^2 - b^2}{2c} \\ y &= \sqrt{a^2 - x^2} \\ \lambda &= 1 - \frac{A}{\pi a^2} \end{aligned} \tag{4-20}$$

where,

A denotes the occulted area;

λ denotes the Earth shadow factor;

For the cylinder model (Montenbruck and Gill 2000a), which can be easily expressed as,

$$\lambda = \begin{cases} 0 & |\varphi| \le \pi/2 \, and \, |\sin\varphi| \le R_B / |r| \\ 1 & others \end{cases} \tag{4-21}$$

where,

φ denotes the angle between the geocentric vector of satellite and the opposite geocentric vector of the Sun;

λ denotes the Earth shadow factor;

4.3.7 Yaw attitude

The attitude of a GNSS satellite is determined by the need to point the navigation antenna toward the Earth and keeping the solar panels oriented to the Sun. There are two common modes for GNSS satellite altitude, namely yaw-steering (YS) and Orbit-Normal (ON). For YS, the spacecraft rotates about the Earth-pointing ("yaw") axis to make the solar panel axis perpendicular to the Sun direction. For ON, the spacecraft body is fixed in the local orbital frame and the solar panel rotation axis is kept perpendicular to the orbital plane (Montenbruck et al. 2015a). In some cases, both attitude modes may be employed on the same satellite, and the details are shown in the following Table 4-1.

Table 4-1 General characteristics of GNSS orbit and attitude

Constellation	Type	Inclination	Period	Attitude
GPS		55^0	11^h58^m	YS
GLONASS		65^0	11^h16^m	YS
Galileo		56^0	14^h05^m	YS
BeiDou-2	MEO	55^0	12^h53^m	YS, ON (near-zero β)
	IGSO	55^0	23^h56^m	YS, ON (near-zero β)
	GEO	$\approx 0^0$	23^h56^m	ON
QZSS		43^0	23^h56^m	YS, ON (low β)
	IGSO	29^0	23^h56^m	Biased YS
IRNSS	GEO	$\approx 0^0$	23^h56^m	Biased YS

The yaw angle (Kouba 2009a) can be calculated as shown in the following Equation (4-22),

$$\psi = \text{atan}\,2(-\tan\beta, \sin\mu) \tag{4-22}$$

where

β denotes the Sun elevation above the orbit plane;

μ denotes the orbit angle relative to the midnight point.

The nominal yaw rate is

$$\dot{\psi}_n = \dot{\mu}\tan\beta\cos\mu(\sin^2\mu + \tan^2\beta) \tag{4-23}$$

By substituting the maximum yaw rates R and set $\mu = 0$ in the above equation, the β angle limit can be obtained as follows,

$$\beta_0 = \tan^{-1}(\dot{\mu} / R) \tag{4-24}$$

By applying some approximation with small angle, the orbit angle at the maneuver start time can be computed for noon and midnight turns correspondingly,

$$\begin{aligned} \mu(ts) &= \boldsymbol{\pi} - \sqrt{\beta_0 |\beta| - \beta^2} \quad , noon \\ \mu(ts) &= -\sqrt{\beta_0 |\beta| - \beta^2} \quad , midnight \end{aligned} \tag{4-25}$$

With the above two equations, the starting time of a turning maneuver can be calculated as follows,

$$t_s = t_m - \sqrt{\beta_0 |\beta| - \beta^2} \,/\, \dot{\mu} \tag{4-26}$$

One key point for generating the low update rate orbit IP is the calculation of the forces on navigation satellites and the dynamic models that consist of a set of force models, which can be expressed as the acceleration components:

$$\vec{\boldsymbol{a}} = \sum \vec{\boldsymbol{a}}_i \tag{4-27}$$

where the acceleration components include the Earth's gravitational acceleration, the gravitational acceleration of the Moon and the Sun, the SRP acceleration, and any other independent accelerations acting on the satellite that can be modeled (Montenbruck and Gill 2000b). As shown in Table 5-2, the Earth's gravitational acceleration has the largest effect on

satellite motion, and the magnitude can be several 1×10^{-1} m/s^2. At the same time, the solar and lunar gravitational acceleration also have a significant effect on satellite orbit, with a magnitude both at several 1×10^{-6} m/s^2. The SRP acceleration is quite stable over one day, with a magnitude at 1×10^{-7} m/s^2.

Table 4-2 Effects of perturbing forces on GPS satellites and the models applied

Items	Models	Acceleration (m/s^2)
Earth gravitation	EGM2008 with degree 12 and order 12 with tide models	1×10^{-1}
Solar gravitation	The law of gravity and solar position from DE405	1×10^{-6}
Lunar gravitation	The law of gravity and lunar position from DE405	1×10^{-6}
SRP	ECOM with 9 parameters	1×10^{-7}
Numerical integrator	7/8 order single-step Runge-Kutta (75 s)	Not applicable
	12 order multi-steps Adams-Bashforsh-Moulton (900 s)	Not applicable
Arc length	24 h	Not applicable
Sample rate	900 s	Not applicable

The current active GPS constellation (up to 18th April 2017) consists of 12 Block II Replenishment (IIR) satellites, 7 Block II Replenishment-Modernized (IIR-M) satellites, and 12 Block II Follow-on (IIF) satellites for a total of 31 satellites, which is under full operational capability. As shown in Table 5-3, there are four different categories of satellites according to the block and satellite clock type, so four different satellites (Pseudo-Random Noise (PRN) 2 IIR/Rubidium (Rb), PRN 5 IIR-M/Rb, PRN 3 IIF/Rb, PRN 8 IIF/Cesium (Cs)) will be used to represent all the GPS satellites.

Table 4-3 Block type, PRN and clock type of GPS (up to 18th April 2017)

	Satellite Space Vehicle Numbers (SVN)/PRN
IIR/Rb	43/13, 46/11, 51/20, 44/28, 41/14, 54/18, 56/16, 45/21, 47/22, 59/19, 60/23, 61/2
IIR-M/Rb	53/17, 52/31, 58/12, 55/15, 57/29, 48/07, 50/5
IIF/Rb	62/25, 63/1, 66/27, 64/30, 67/6, 68/9, 69/3, 71/26, 73/10, 70/32
IIF/Cs	65/24, 72/08

The Earth's gravitational acceleration varies between 0 to ± 0.6 m/s^2, and the values for different satellite are similar. For lunar gravitational acceleration, the absolute value peaks around 4×10^{-6} m/s^2 and varies with the motion of the GPS satellites. The maximum absolute solar gravitational acceleration is around 2×10^{-6} m/s^2, which is the same magnitude as the lunar gravitational acceleration. For the SRP acceleration, the magnitude is between 1×10^{-8} m/s^2 and 1×10^{-7} m/s^2; the SRP plot for PRN 2 and PRN 5 overlaps due to the small difference of SRP acceleration leveled at 1×10^{-11} m/s^2.

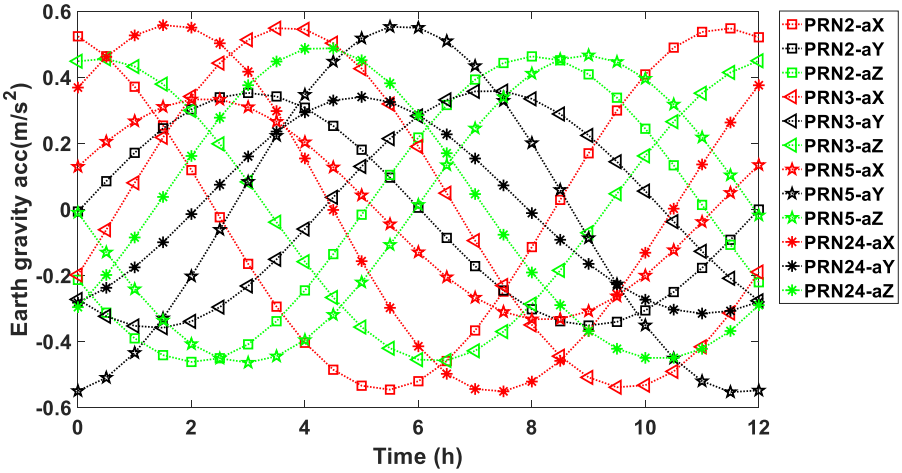

a. Earth gravitational acceleration

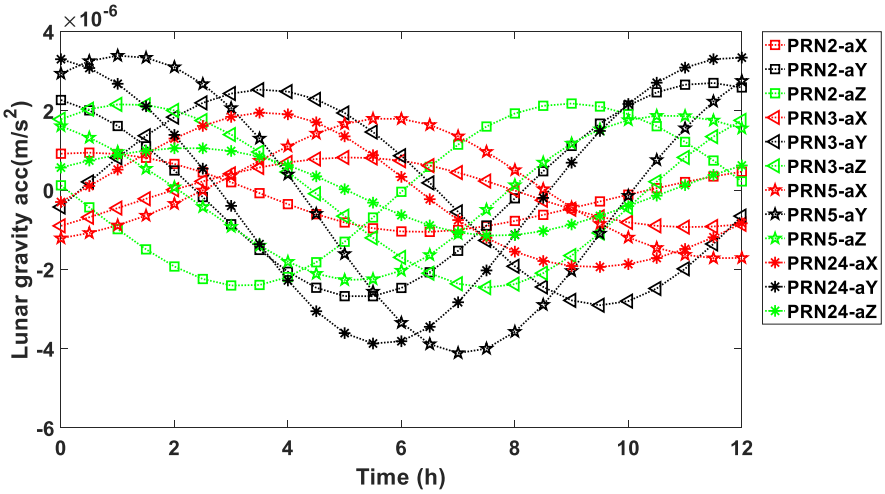

b. Lunar gravitational acceleration

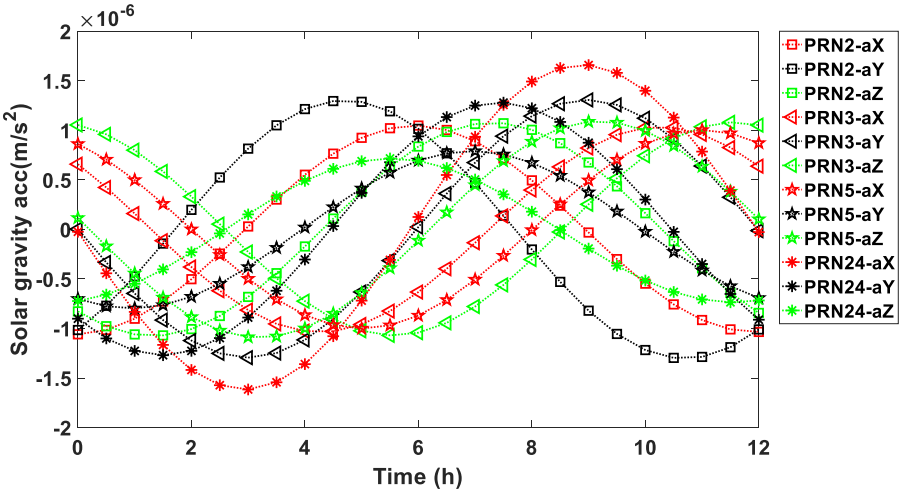

c. Solar gravitational acceleration

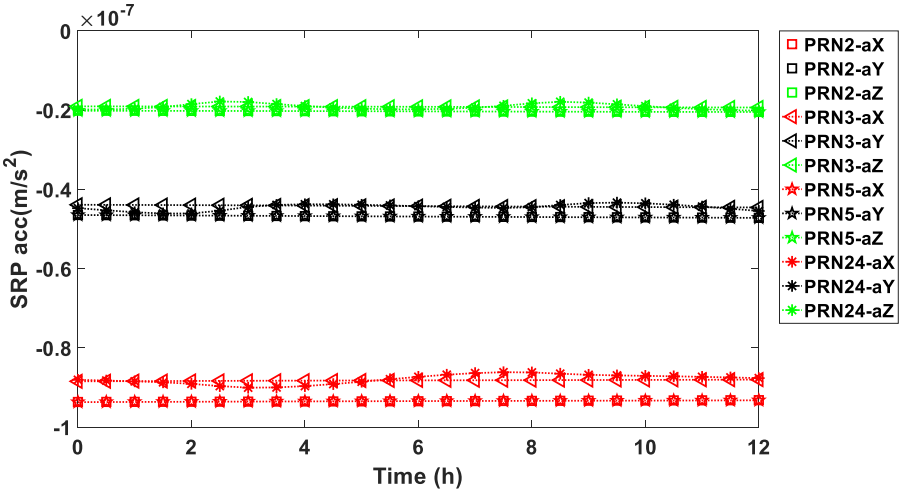

d. SRP acceleration

Figure 4-1 Earth gravitational acceleration, lunar gravitational acceleration, solar gravitational acceleration, and SRP acceleration over 12 hours for GPS satellites PRN2, PRN 3, PRN 5, and PRN 24.

4.1.2 Variation equations

The orbit IP $x_0 = \left[r_{3*1}^0, v_{3*1}^0, p_{9*1}^0 \right]$ at specific epoch describes the satellite orbit and velocity in space. Any change of these IP at reference epoch will affect the predicted orbit and velocity at epoch t. The relation can be presented by transition matrix and sensitivity matrix (Montenbruck and Gill 2000a) as following;

$$\left(\frac{\partial y(t)}{\partial y(t_0)} \right)_{6\times 6} = \Phi(t, t_0) \tag{4-28}$$

$$\left(\frac{\partial y(t)}{\partial P} \right)_{6\times 9} = S(t) \tag{4-29}$$

If the state vector is described as:

$$y(t) = \begin{pmatrix} r(t) \\ v(t) \end{pmatrix} \tag{4-30}$$

The first order differential equation over time is

$$\frac{d}{dt} y(t) = f(t,y) = \begin{pmatrix} v(t) \\ a(t,r,v) \end{pmatrix} \tag{4-31}$$

Take the derivation over $y(t_0)$, and the equation turns to

$$\frac{\partial}{\partial y(t_0)} \frac{d}{dt} y(t) = \frac{\partial f(t, y(t))}{\partial y(t_0)} = \frac{\partial f(t, y(t))}{\partial y(t)} \cdot \frac{\partial y(t)}{\partial y(t_0)} \tag{4-32}$$

The equation can be rewritten as:

$$\frac{d}{dt}\Phi(t,t_0)=\frac{\partial f(t,y(t))}{\partial y(t)}\cdot\Phi(t,t_0)$$
$$=\begin{pmatrix}0_{3\times3} & 1_{3\times3}\\ \dfrac{\partial a(r,v,t)}{\partial r(t)} & \dfrac{\partial a(r,v,t)}{\partial v(t)}\end{pmatrix} \tag{4-33}$$

And the initial transition matrix is a unit matrix $\Phi(t_0,t_0)=I_{6\times6}$.

Looking at the differential equation of the sensitivity matrix presenting the partial derivations of the state vector with respect to the force model parameters, which is shown as :

$$\frac{d}{dt}\frac{\partial y(t)}{\partial p}=\frac{\partial f(t,y(t),P)}{\partial y(t)}\cdot\frac{\partial y(t)}{\partial p}+\frac{\partial f(t,y(t),P)}{\partial P} \tag{4-34}$$

The equation can be expressed in the following form as well.

$$\frac{d}{dt}S(t)_{6\times n_p}=\begin{pmatrix}0_{3\times3} & I_{3\times3}\\ \dfrac{\partial a(t,r,v,p)}{\partial r(t)} & \dfrac{\partial a(t,r,v,p)}{\partial v(t)}\end{pmatrix}_{6\times6}\cdot S(t)+\begin{pmatrix}0_{3\times n_p}\\ \dfrac{\partial a(t,r,v,p)}{\partial p}\end{pmatrix}_{6\times n_p} \tag{4-35}$$

The initial sensitive matrix is $S(t_0)=\mathbf{0}$.

By combining differential equations for the state transition matrix and sensitive matrix, one can obtain the following variation equation:

$$\frac{d}{d(t)}(\Phi,S)=\begin{pmatrix}\mathbf{0}_{3\times3} & \mathbf{1}_{3\times3}\\ \dfrac{\partial a}{\partial r} & \dfrac{\partial a}{\partial v}\end{pmatrix}_{6\times6}\cdot(\Phi,S)+\begin{pmatrix}\mathbf{0}_{3\times6} & \mathbf{0}_{3\times n_p}\\ \mathbf{0}_{3\times6} & \dfrac{\partial a}{\partial p}\end{pmatrix}_{6\times(6+n_p)} \tag{4-36}$$

4.1.3 Numerical integrator

The orbit numerical integration is used to find numerical approximations to the solutions of ordinary differential equations, which will be applied in the generation of high-precision orbit. A

first-order differential equation is an initial value problem of the form as shown in the following Equation (4-37),

$$y'(t) = f(t, y(t)), \qquad y(t_0) = y_0 \tag{4-37}$$

Various numerical methods have been developed to solve the above equation, such as Euler's, the Modified Euler, Midpoint, Runge–Kutta (Munthe-Kaas 1999), and Adams–Bashforth–Moulton methods (Nordsieck 1962). In this experiment, the Runge–Kutta and Adams–Bashforth–Moulton methods are applied. First, the single step Runge–Kutta method is applied to obtain the start points; then, the Adams–Bashforth–Moulton multi-step method is used to predict forwards. The general expression of the Runge–Kutta method can be expressed as the following Equation (4-38):

$$\begin{aligned}
y_{n+1} &= y_n + h\sum_{i=1}^{s} b_i k_i \\
k_1 &= f(t_n, y_n) \\
k_2 &= f(t_n + c_2 h, y_n + h(a_{21} k_1)) \\
k_2 &= f(t_n + c_3 h, y_n + h(a_{31} k_1 + a_{32} k_2)) \\
&\vdots \\
k_s &= f(t_n + c_s h, y_n + h(a_{s1} k_1 + a_{s2} k_2 + \cdots + a_{s,s-1} k_{s-1}))
\end{aligned} \tag{4-38}$$

To specify a specific method, one needs to provide the integer s (the number of orders), and the coefficients a_{ij} (for $1 \le j < i \le s$), b_i (for $i = 1, 2, \ldots s$) and c_i (for $i = 2, 3, \ldots s$). If we assume that several start points have been obtained by carrying out the Runge–Kutta in a row, then we can come to the Adams–Bashforth–Moulton method, which consists of predictor (Adams–Bashforth) and corrector (Adams–Moulton) parts. Adams–Bashforth and Adams–Moulton can be expressed as the Equation (4-39) and Equation (4-40) correspondingly:

$$
\begin{aligned}
y_n &= y_{n-1} + h\sum_{s=0}^{n-1} b_s f(t_s, y_s) \\
b_{s-j-1} &= \frac{(-1)^j}{j!(s-j-1)!}\int_0^1 \prod_{\substack{i=0 \\ i\neq j}}^{s-1} (u+i)du, \quad for \quad j = 0,\ldots,s-1.
\end{aligned}
\tag{4-39}
$$

$$
\begin{aligned}
y_n &= y_{n-1} + h\sum_{s=0}^{n} b_s f(t_s, y_s) \\
b_{s-j} &= \frac{(-1)^j}{j!(s-j)!}\int_0^1 \prod_{\substack{i=0 \\ i\neq j}}^{s-1} (u+i-1)du, \quad for \quad j = 0,\ldots,s.
\end{aligned}
\tag{4-40}
$$

The difference between the predictor and corrector is the former utilizes only $f(t_1, y_1) \cdots f(t_{n-1}, y_{n-1}), y_1 \cdots y_{n-1}$ to derive the value of y_n, while the latter also makes use of $f(t_n, y_n), y_n$ to obtain y_n. When the multi-step predictor and corrector are implemented together, accuracy will be improved. The implementation of the integrator (Yang and Gao 2017)is presented in Fig. 4-2.

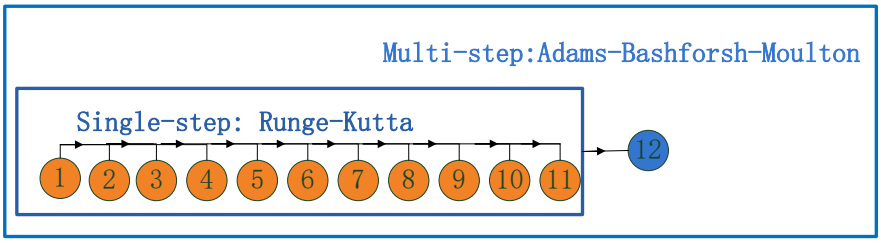

Figure 4-2 Implementation of the numerical integrator for orbit prediction

In terms of orbit generation, the y can be set as the (r, V) where r and V are satellite position and velocity in three different directions. Then, $f(t_s, y_s) = (V, \alpha)$, where α is the acceleration in three different directions. If y_0 and the expression of $f(t_s, y_s)$ are known, then the orbit prediction can be carried out forwards or backwards. Here to note, the numerical integrator for orbit prediction is carried out in the ICRF and need to be transformed to ITRF afterwards.

4.1.4 Estimation of satellite orbit IP

Orbit fitting is another crucial step for generating satellite orbit IP. First, setting a priori orbit IP $x_0 = [r^0_{3\times1}, v^0_{3\times1}, p^0_{9\times1}]$, including three position parameters, three velocity parameters, nine SPR parameters, and the orbit error function at time t_k, will have the following form:

$$\overrightarrow{\boldsymbol{v}_k} = \boldsymbol{h}(t_k, \vec{\boldsymbol{a}}, \boldsymbol{x}_0) - \vec{\boldsymbol{r}}_k, \quad \boldsymbol{P}_k \tag{4-41}$$

where

$\vec{\boldsymbol{v}}_{\boldsymbol{k}}$ denotes the residual;

$\vec{\boldsymbol{r}}_{\boldsymbol{k}}$ denotes the observation;

$\boldsymbol{P}_{\boldsymbol{k}}$ denotes the weight matrix.

After linearization by calculating the partial derivation of $\boldsymbol{h}(t_k, \vec{\boldsymbol{a}}, \boldsymbol{x}_0)$ with respect to x_0, Equation (4-41) transforms into the following Equation (4-42).

$$\begin{aligned} \overrightarrow{v_k} &= H\Delta x_0 - \vec{l}, P_k \\ H &= \frac{\partial h(t_k, \vec{a}, x_0)}{\partial x_0} \text{ and } \vec{l} = \overrightarrow{r_k} - h(t_k, \vec{a}, x_0) \end{aligned} \tag{4-42}$$

where,

H denotes the design matrix,

Δx_0 denotes the corrections for a priori IP,

$\vec{l}$ denotes the misclosure vector and the other symbols denote the same value as above.

Once Equation (4-42) has been constructed at all the selected epochs, then the LS can be carried out to calculate the Δx_0 as:

$$\Delta \boldsymbol{x}_0 = \left(\sum_{k=1}^{m} \boldsymbol{H}_k^T \boldsymbol{P}_k \boldsymbol{H}_k\right)^{-1} \cdot \sum_{k=1}^{m} \boldsymbol{H}_k^T \boldsymbol{P}_k l_k \tag{4-43}$$

Finally, the refined $\hat{x}_0$ is obtained as $\hat{x}_0 = x_0 + \Delta x_0$. With the estimated $\hat{x}_0$, the orbit can be predicted to the specific epoch by applying numerical integration.

4.2 Satellite Clock IP Generation at Server End

In this section, the atomic clocks onboard GPS satellites are first introduced in Section 4.2.1 focusing on types, ages and stability. Current satellite clock offsets prediction models are introduced in Section 4.2.2, in which the IGU-P model is demonstrated in detail. Date prediction depends on both the raw data and prediction algorithm. With different latencies of satellite clock offset products, prediction can be divided into the post-mission mode and real-time mode. The satellite clock offset prediction in post-mission is discussed as the background for real-time prediction. In Section 4.2.3, a new satellite clock offset prediction method based on IGS RTS is proposed.

4.2.1 Atomic clocks onboard GPS satellites

Currently, the GPS constellation is a mix of old and new satellites and thus the onboard clocks are of different types. As the last GPS IIA satellite (PRN32/ SVN23) became unusable on January 25th, 2016, the current satellite clocks in orbits include only IIR/Rb, IIR-M/Rb, IIF/Rb and IIF/Cs and the details are listed in Table 4-4. The ages of clocks onboard GPS satellites are shown in the following Fig. 4-3, as we can see, the oldest satellite clock is around 20 years old.

Table 4-4 Block-type, PRN and clock type of GPS (up to 21st Aug of 2017)

	Satellite PRN
IIR/Rb	16,28,20,19,2,21,11,22,18,14,23,13
IIR-M/Rb	31,7,12,29,17,5,15
IIF/Rb	30,25,26,27,1,6,3,10,9,32
IIF/Cs	24,8

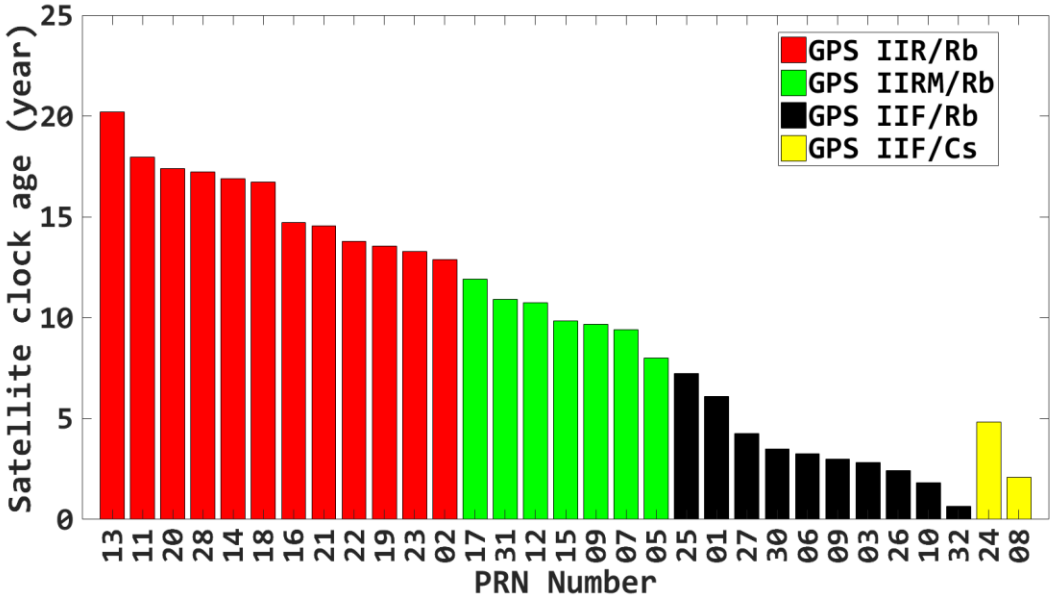

Figure 4-3 The ages of the GPS satellite clocks (calculated on 21st Aug of 2017)

The Allan variance (AVAR), also known as two-sample variance, is a measure of frequency stability in clocks, oscillators and amplifiers. The Allan deviation (ADEV), also known as sigma-tau, is the square root of Allan variance. At very short observation time τ, the Allan deviation is high due to noise. At longer τ, it decreases because the noise averages out. At still longer τ, the ADEV starts increasing again, suggesting that clock frequency is gradually drifting due to temperature changes, aging of components, or other such factors. The Modified AVAR (MVAR) is commonly used as a tool to measure the frequency stability in oscillators and its main advantage relative to Allan variance is its ability to separate white phase noise from flicker phase noise (Allan and Barnes 1981).

In this section, the MVAR is utilized to measure the stability of different types of satellite clocks. The IGU observed clock offsets for Day 360 of 2015 are utilized for the investigation and the results are shown in the Fig. 4-4.

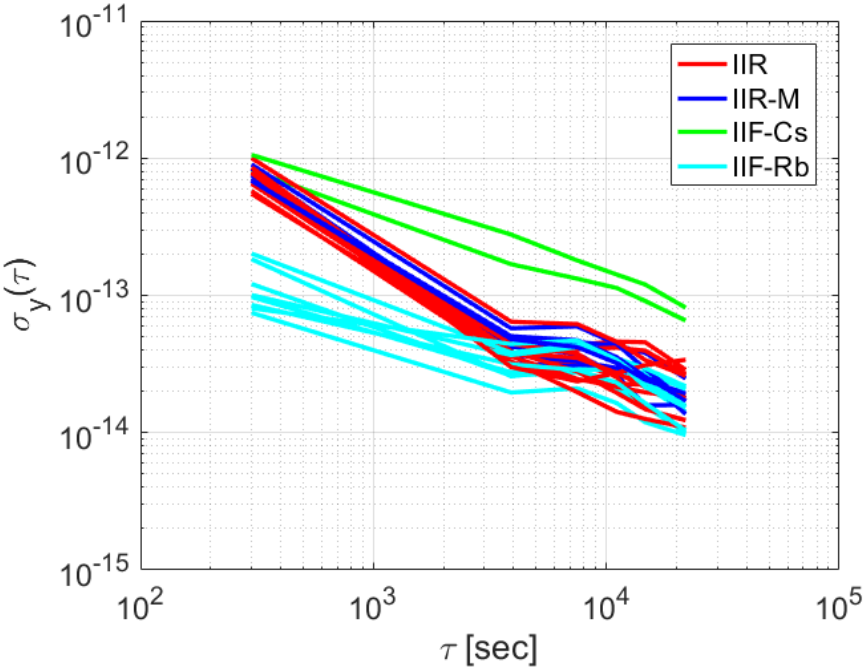

Figure 4-4 The MVAR for all GPS satellites clock offsets

As shown in Fig. 4-4, the IIF/Rb clocks are of highest stability while the IIR and IIR-M are comparable to each other, and IIF/Cs clocks have the poorest stability. The stability of the satellite clock is not only related to the satellite type but also significantly affected by the clock type. Meanwhile, the MVAR indicates that the optimum satellite clock offsets prediction error can be described by the following equation (Allan 1987; Bhattarai 2015):

$$\sigma_p(\tau_p) = \sigma_y(\tau_p)\tau_p \tag{4-44}$$

where,

σ_p denotes the prediction error deviation;

τ_p denotes the length of the prediction;

$\sigma_y(\tau_p)$ denotes the Allan deviation;

The average prediction errors of the four different types of satellite clocks are presented in Table 4-5, which shows that the largest prediction errors belong to the IIF/Cs clocks and the Rb clocks can be predicted at a better accuracy around 0.2 ns for 6 hours.

Table 4-5 Average optimum prediction errors of four different types of satellite clock offsets (ns)

	$\tau_p = 1\ hour$	$\tau_p = 2\ hours$	$\tau_p = 3\ hours$	$\tau_p = 6\ hours$
IIR/Rb	0.15	0.17	0.18	0.20
IIR-M/Rb	0.17	0.22	0.22	0.23
IIF/Rb	0.12	0.17	0.17	0.17
IIF/Cs	0.87	1.54	1.66	1.75

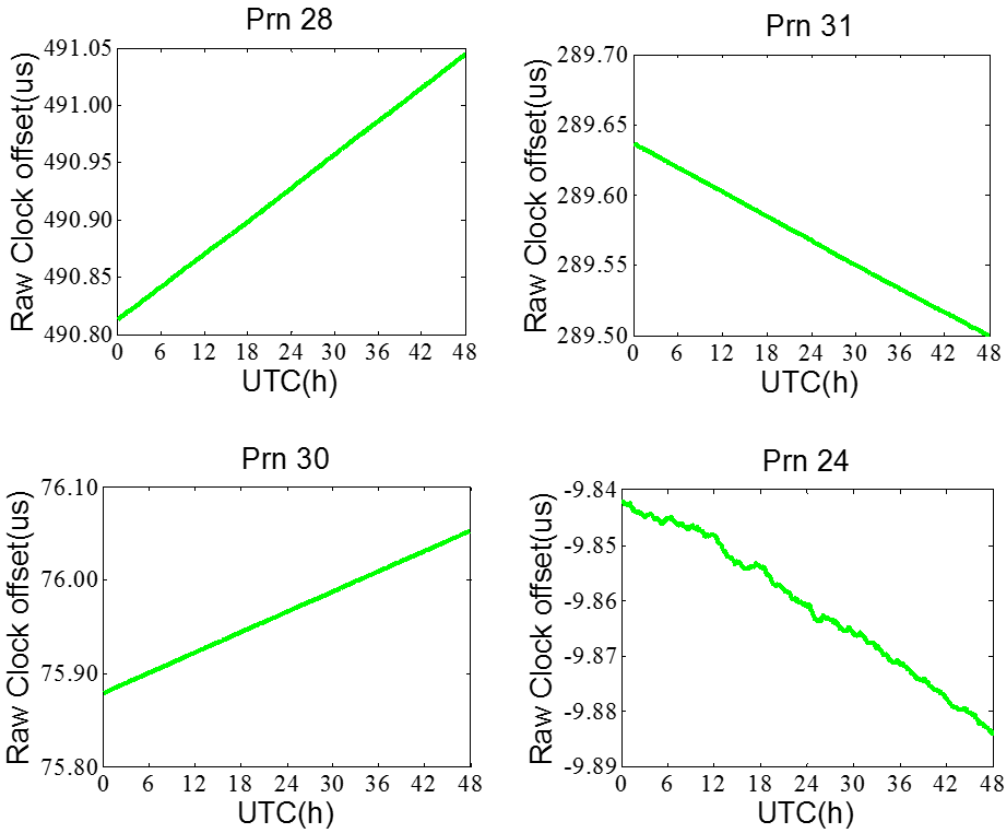

Figure 4-5 The raw satellite clock offset data in two consecutive days (Day 360 and 361 of 2015)

Four GPS satellites with different types of satellite clocks, namely PRN 28 (IIR/Rb), PRN 31 (IIR-M/Rb), PRN 30 (IIF/Rb) and PRN 24 (IIF/Cs), are selected in this section to represent all the GPS satellites. The data used here is the IGU observed clock offsets (Day 360 and 361 of 2015). As shown in Fig. 4-5, the linear trend is evident for all four selected satellites and the magnitudes of the satellite clock offsets variation over 48 hours are different. Therefore, the linear terms are assumed as the primary parts in most satellite clock offset prediction models, such as IGU-P model.

4.2.2 Satellite clock offsets prediction models

Currently, the IGU-P model given in Equation (4-45) is considered the most accurate one for satellite clock offset prediction (Huang et al. 2014). The model includes both the polynomial terms and the periodic terms. The periodic terms are reported at four different frequencies, at 12h, 6 h, 4 h and 3h, which are directly related to the orbit errors in the radial direction (Arnold et al. 2015). All four harmonics are much smaller for the IIR and IIR-M satellites than for the older blocks (Senior et al. 2008).

$$x(t) = x_0 + y_0 t + \frac{\beta z_0 t^2}{2} + \sum_{l=0}^{k} A_l \sin(\omega t + \varphi_l) + \Psi(t),$$
$$\beta = \begin{cases} 1\ , \ \text{IIA(Rb)} \\ 0\ , \ \text{IIA(Cs)} / \text{IIR} / \text{IIR} - \text{M} \end{cases} \tag{4-45}$$

where

x_0, y_0 and z_0 denote time offset, frequency offset and frequency drift;

β denotes a selective factor;

k denotes the number of periodic terms;

A_l denotes the amplitude;

ω denotes the frequency;

φ_l denotes the phase shift of the sinusoidal variation;

$\Psi(t)$ denotes the generic random noise process.

The IGU-P model does not include GPS IIF satellite clocks. To study the latest GPS IIF satellite clock offset prediction model, the linear fitting and quadratic fitting are compared for both the fitting residuals and clock prediction accuracy. The fitting residuals on Day 360 of 2015 are shown in Fig. 4-6, for the four selected GPS IIF clocks.

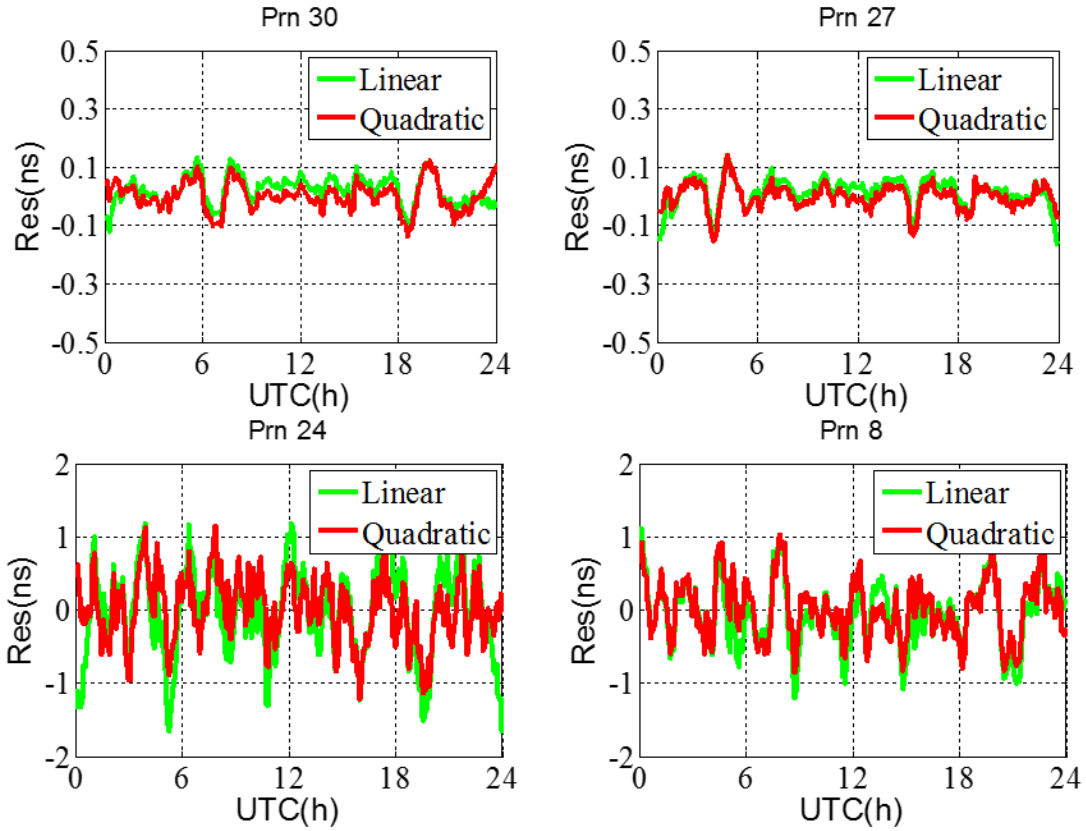

Figure 4-6 The residual after linear and quadratic fitting for PRN 30, PRN 27, PRN 24 and PRN 8

As shown in Fig. 4-6 the residuals of the IIF-Rb clocks (PRN 30 and PRN 27) are mostly at several tens of picoseconds, which are much smaller than that of the IIF-Cs clocks (PRN 24 and

PRN 8) which are mostly at several hundreds of picoseconds. The differences between the linear fitting and quadratic are summarized in Table 4-6.

Table 4-6 RMS of Block IIF satellite clock residuals after linear and quadratic fitting (ns)

PRN	1	3	6	8	9	24	25	26	27	30
Linear	0.05	0.04	0.06	0.44	0.04	0.63	0.04	0.04	0.05	0.05
Quadratic	0.05	0.04	0.05	0.40	0.04	0.45	0.05	0.04	0.04	0.05

Table 4-6 demonstrates that almost all the residuals after quadratic fitting are smaller than that with linear fitting, and the differences between these two different fitting models are tiny at several picoseconds for the GPS IIF/Rb clocks. At this point, it cannot be confirmed that the quadratic fitting is more suitable for the GPS IIF satellite clocks. Stochastic noise in the satellite clock is reportedly able to cause this difference (Hackman 2012), and more investigation should be done regarding the accuracy of the prediction. After prediction with linear and quadratic models, the statistics of the average prediction accuracy of the GPS IIF clocks with prediction lengths of 1 hour, 2 hours, 3 hours and 6 hours is shown in Table 4-7.

Table 4-7 Prediction errors for IIF/Rb and IIF/Cs clocks with different fitting models and update intervals (ns)

	$\tau_p = 1\ hour$	$\tau_p = 2\ hours$	$\tau_p = 3\ hours$	$\tau_p = 6\ hours$
IIF/Rb-Linear	0.21	0.26	0.33	0.64
IIF/Rb- Quadratic	0.21	0.25	0.30	0.63
IIF/Cs-Linear	1.60	1.79	1.53	1.86
IIF/Cs- Quadratic	1.12	1.46	1.25	1.83

As shown in Table 4-7, there is a small difference between the prediction errors among the GPS IIF/Rb clocks and both of them can reach 0.6ns for prediction with a prediction length of 6 hours. But for the IIF/Cs clocks, the prediction error of the IIF/Cs clocks after the quadratic fitting is smaller than that with linear fitting. According to the above data analysis, an initial conclusion can be drawn that for GPS IIF/Rb clocks, both linear and quadratic fitting can be utilized and the

quadratic fitting is slightly better, meanwhile quadratic fitting is recommended for GPS IIF/Cs clocks according to the above fitting and prediction results.

According to satellite clock models described in Equation (4-45), the satellite clock offset fitting can be carried out in two steps, namely polynomial fitting and periodic terms extraction. The polynomial fitting model can be presented by

$$V = BX - L \ , \mathrm{P} \tag{4-46}$$

where

- X denotes the satellite clock offset polynomial parameter vector;
- B denotes the design matrix;
- L denotes the observation vector of satellite clock offset;
- V denotes the residual vector of the observations;
- P denotes the weight matrix of the observations;

The LS method or Kalman filter can be utilized to estimate polynomial parameter vector X, and after that, the prediction of the polynomial can be carried out with the estimated X and the prediction epoch. After removing the polynomial terms, the Discrete Fast Fourier Transform (DFFT) will be used to extract the largest four periodic terms through spectrum analysis (Bergland 1969), in which the frequency is not constrained to any specific value. To better fit the satellite clock offsets, the LS and FFT are carried out successively for the IGU observed clock offset (Day 360 of 2015). The fitting residuals after LS and LS+FFT are shown in Fig. 4-7.

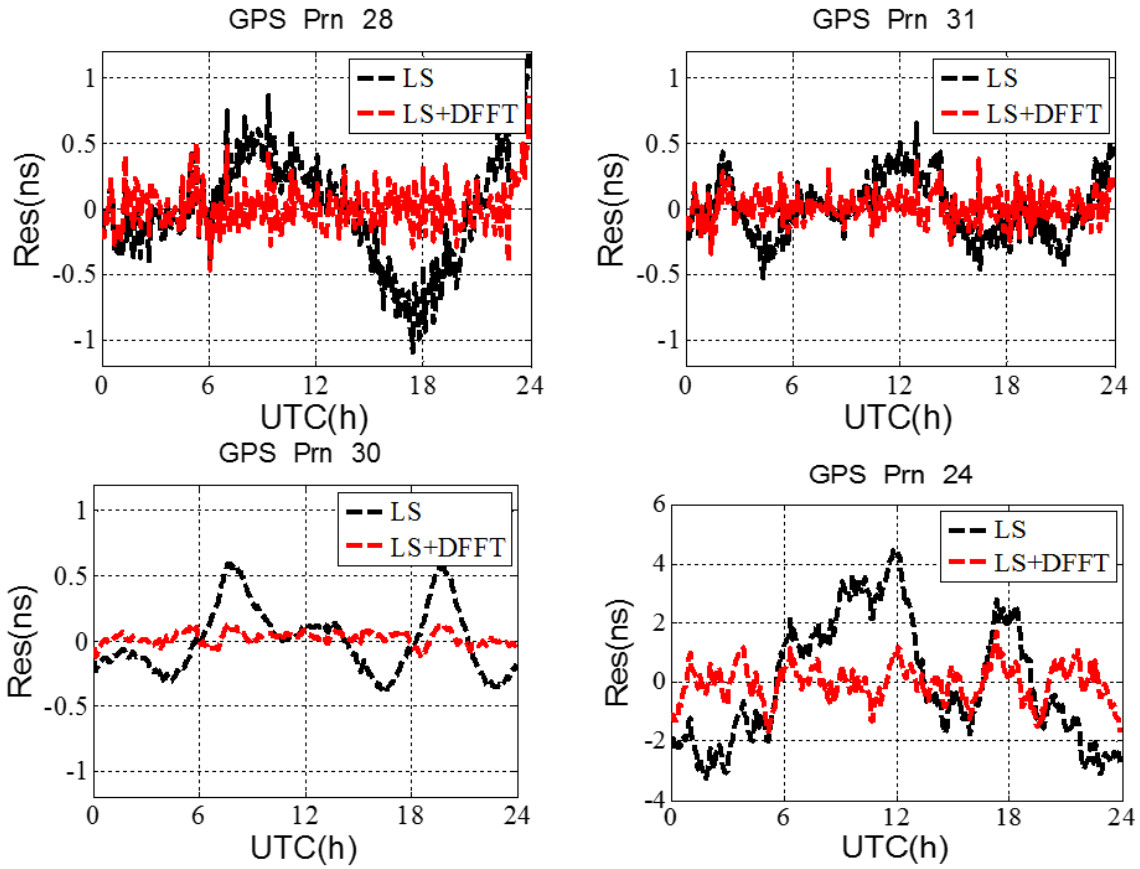

Figure 4-7 Residual after LS and FFT for PRN 28, PRN 31, PRN 30 and PRN 24

As shown in Fig. 4-7, the polynomial terms in the satellite clock offset can be fitted very well and the residuals are smaller than 1ns for most satellites. The influences of the periodic terms for most satellites are at several hundreds of picoseconds but can reach several nanoseconds for PRN 24. The periodic terms can also be extracted effectively by DFFT and the residuals after LS and DFFT are smaller than 0.5 ns for most satellites. Not surprisingly, the final residuals of the PRN 24 tend to be much larger than the other satellites. The results of FFT for the periodic terms extraction are given in Fig. 4-8 to show the satellite clock offsets in the frequency domain after removing the polynomial trend terms.

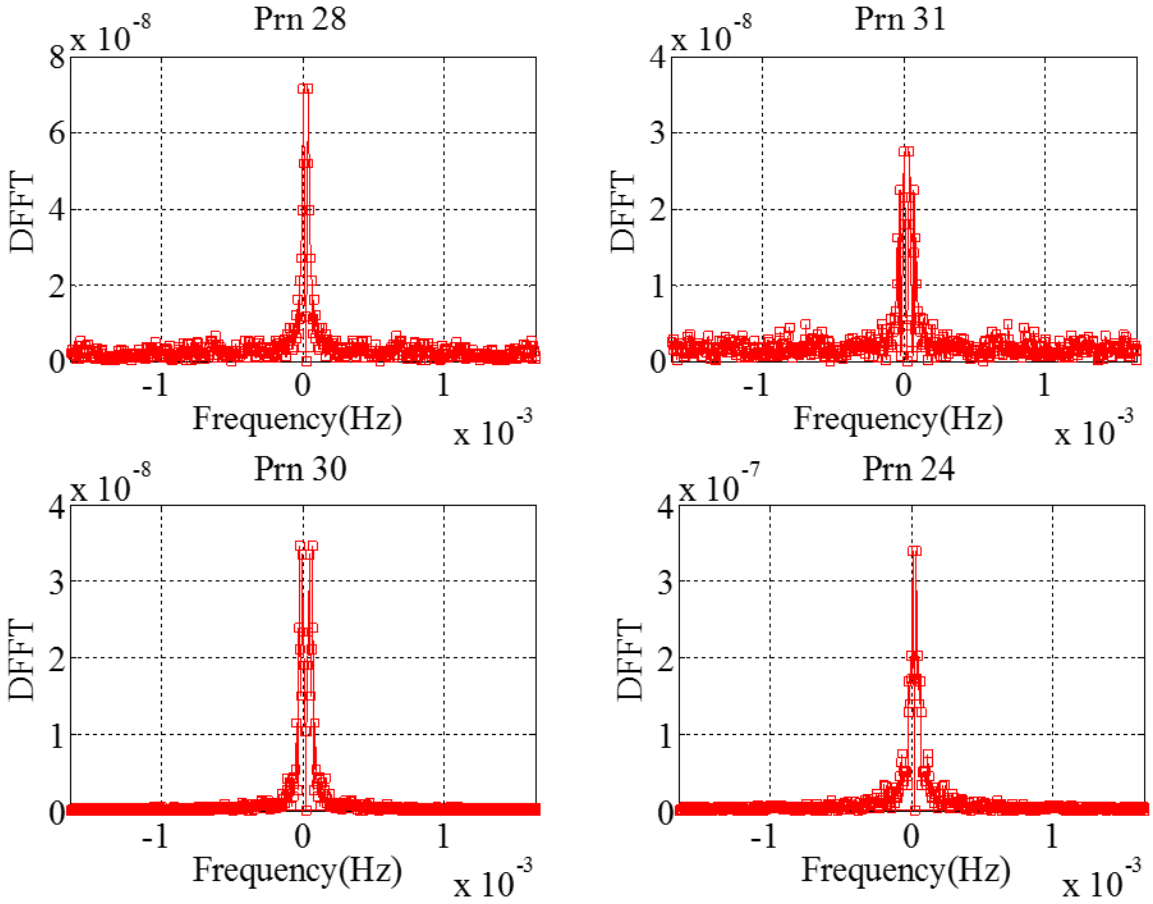

Figure 4-8 Satellite clock offsets in the frequency domain for PRN 28, PRN 31, PRN 30 and PRN 24

There are some high-power terms over the frequency domain and the highest four terms will be selected to do the IDFFT later. Using PRN 28 as an example, the four periods are 14.2 hours, 21.3 hours, 10.7 hours and 8.5 hours correspondingly. The four periods are not exactly the same for all the GPS satellites due to the clock noise in the data used for periodic terms extraction. To investigate whether the largest four terms can represent the satellite clock offsets, the power ratio of the largest four terms ove rall frequency points are calculated as shown in Equation (4-47).

$$R = \frac{\sum_{i=1}^{4} P_i}{\sum_{i=1}^{n} P_i} \tag{4-47}$$

where,

R denotes the power ratio of the four largest terms over all frequency points;

P_i denotes the power of each frequency point in descending order;

The power ratio results of GPS satellites are summarized in Fig. 4-9. Most of the power ratio is over 60% and the average power ratio is about 80.61%, which proves that the selected four terms can effectively recover most of the periodic terms.

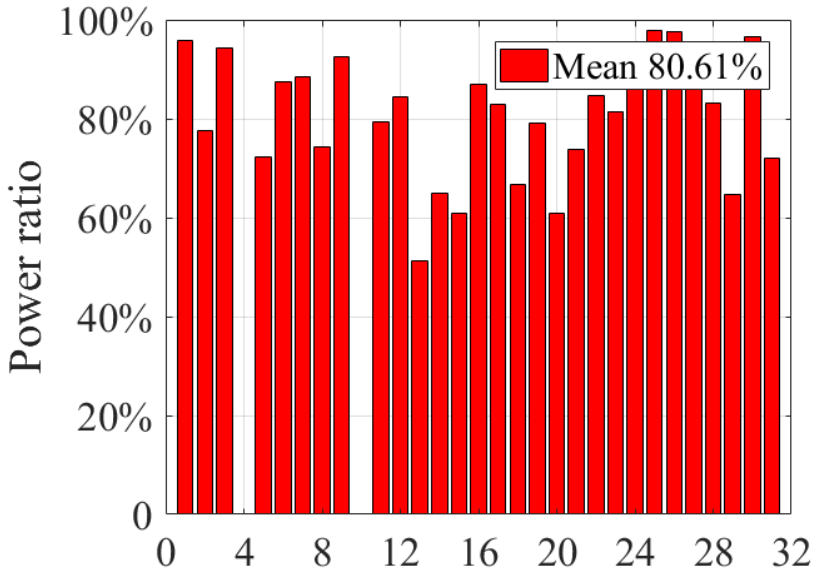

Figure 4-9 Power ratio of all the GPS satellites

Apart from the above analysis, investigation with longer data is carried out. The IGS final clock products for the whole year of 2016 are downloaded from the CDDIS. First, the polynomial fitting is carried out to remove trend terms; Afterwards, the residual check is carried out to prevent outliers; Then the FFT is carried out to investigate periodic terms with such a long

dataset. Correspondingly, after removing the trend, the residual terms are shown for PRN 31, PRN 30, PRN 28 and PRN 24.

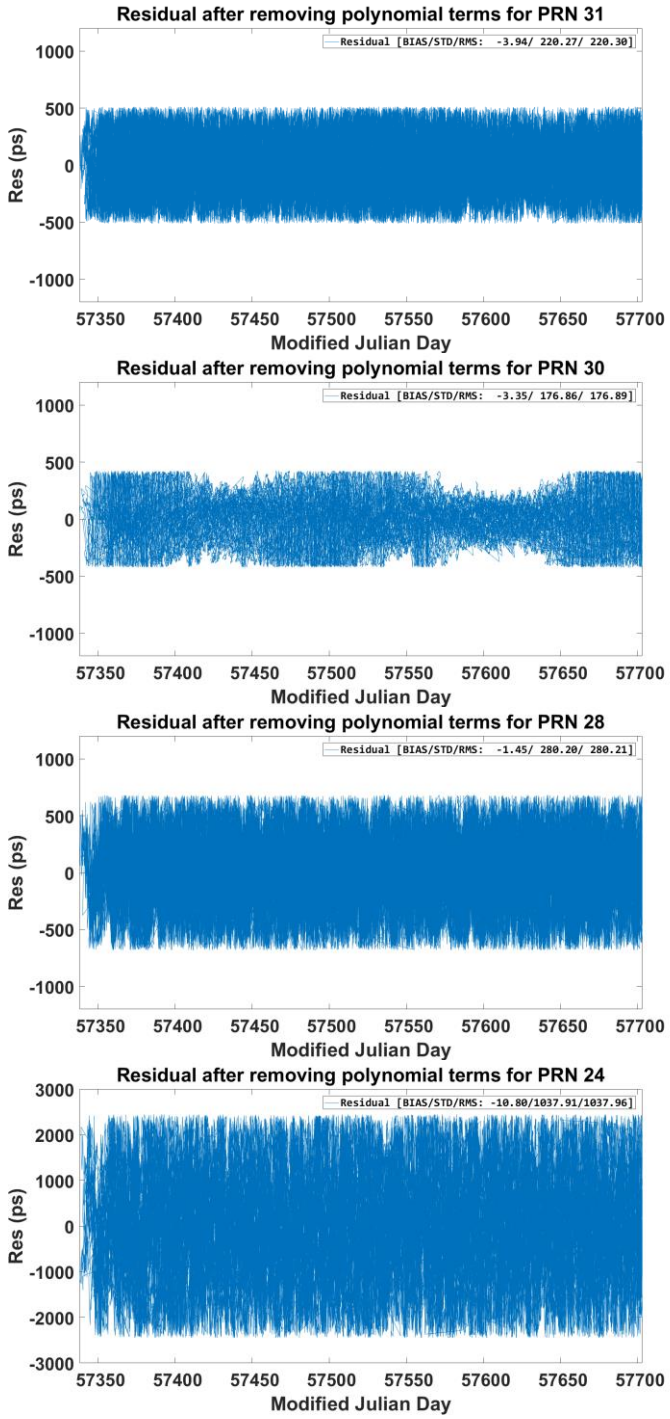

Figure 4-10 The residuals after removing polynomial terms for PRN 31, PRN 30, PRN 28 and PRN 24

The residuals after removing the polynomial terms for PRN 31, PRN 30 and PRN 28 are quite close and the maximum values are around 500 picoseconds, while the maximum residual for PRN 24 is more than 2000 picoseconds. This proves the poor stability of the Cs clocks onboard GPS Block IIF again. The following figure shows the clock offset data without trend terms in frequency domain for the selected four satellites:

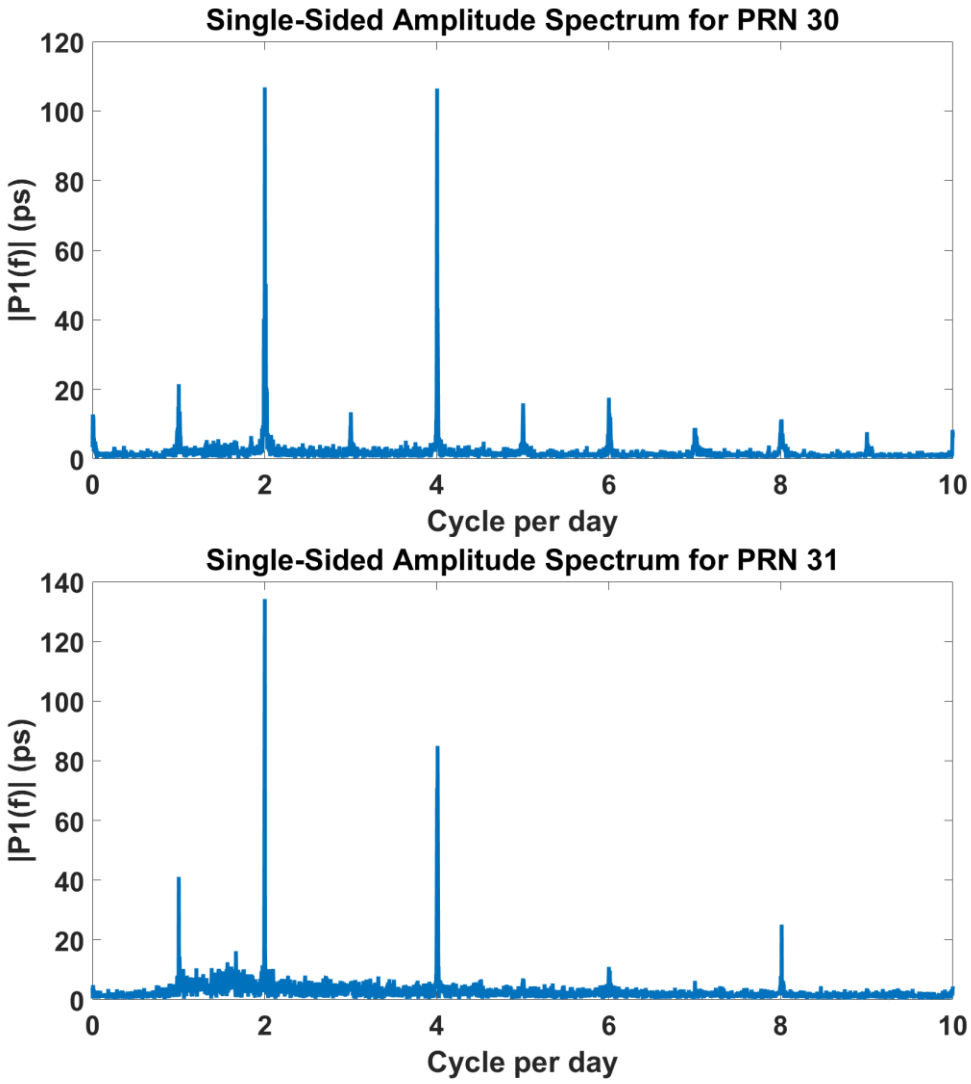

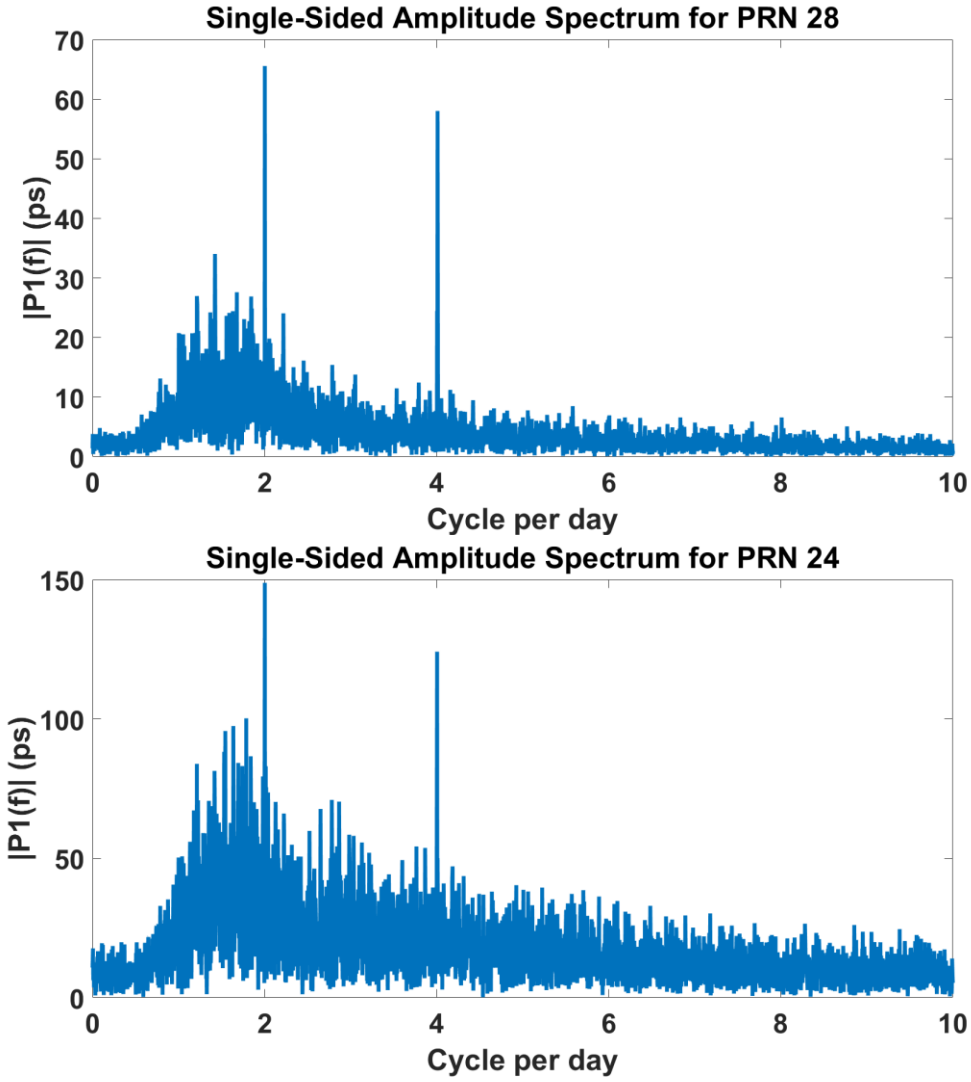

Figure 4-11 Single-sided amplitude spectrum for PRN 31, PRN 30, PRN 28 and PRN 24

The largest two periods with a data length of one year are 12 hours and 6 hours correspondingly for PRN 28, PRN 31, PRN 30 and PRN 24. The magnitude of these two periods can reach 100 picoseconds approximately. There are also other periods, such as 3 hours, 4 hours and 24 hours and so on, but the magnitude is relatively smaller and may not be included by all the satellites. The six largest periodic terms are shown as following Table 4-8 for each GPS satellite, as wen

can see, for all GPS satellite clocks, the dominant periods under 24 hours are around 12 hours and 6 hours.

Table 4-8 The six largest periodic peaks for the amplitude spectrum

PRN	1st	2nd	3rd	4th	5th	6th
1	11.9836	5.9918	23.9346	15.8556	13.1694	7.9927
2	5.9837	11.9673	15.1972	3.9945	13.3699	17.6386
3	11.9836	5.9918	23.9346	19.3480	15.8843	3.9982
5	11.9836	5.9837	23.9346	3.9909	13.9873	7.9927
6	11.9836	5.9918	23.9346	3.9982	7.9927	13.3699
7	11.9836	5.9918	23.9346	16.0879	3.9945	7.9927
8	11.9836	5.9918	17.1898	13.9208	10.0274	9.3051
9	11.9836	5.9837	23.9346	3.9982	7.9710	2.9939
10	11.9835	5.9918	23.9342	3.9982	13.4194	8.0000
11	11.9836	23.9346	5.9837	16.5736	13.6398	7.9927
12	11.9836	5.9918	23.9346	3.9945	7.9927	2.9959
13	11.9835	5.9835	23.9341	2.9938	13.4031	16.4068
14	5.9832	11.9832	23.9328	14.8850	10.0518	17.7261
15	11.9836	5.9837	23.9346	3.9945	8.0073	15.1710
16	11.9832	5.9916	23.9328	3.9944	2.9958	7.9925
17	11.9836	5.9918	23.9346	3.9945	2.9959	14.7383
18	11.9836	5.9837	23.9346	0.2500	7.9927	14.5914
19	11.9836	5.9837	23.9346	2.9959	14.7630	9.6105
20	5.9837	11.9836	14.9642	23.7405	2.9939	13.2289
21	11.9836	5.9837	23.9346	2.3954	2.9939	3.9982
22	11.9836	5.9837	23.9346	16.1471	13.6398	19.0957
23	11.9836	5.9837	23.9346	13.1300	15.3835	18.2620
24	11.9836	5.9918	15.5469	13.4312	19.7838	8.3737
25	5.9918	11.9836	23.9346	3.9982	2.9959	8.0073
26	5.9918	12.0164	23.8049	3.9982	2.9959	8.0219
27	11.9836	5.9918	23.9346	3.9982	7.9927	2.9959
28	11.9836	5.9837	16.8599	14.3062	19.7838	10.8177
29	11.9836	5.9918	23.9346	2.9959	3.9945	7.9927
30	5.9918	11.9836	23.9346	3.9982	7.9927	2.9959
31	11.9836	5.9837	23.9346	2.9959	14.4000	16.3271
32	5.9835	11.9834	23.9339	3.9908	7.9926	4.7921

Usually, the FFT can be quickly realized to obtain the periods, and we can then linearize the periodic terms and use the LS to estimate. The equation can be written as following,

$$R = \sum_i (A_i \sin(\frac{2\pi}{T_i} t) + B_i \cos(\frac{2\pi}{T_i} t)) \tag{4-48}$$

where,

R denotes the residual after removing the trend terms;

A_i and B_i denote the amplitudes for sin and cos function;

T_i denote the periods of the signal, which can be obtained from FFT;

t denotes the reference time.

Another experiment is carried out to confirm the equality of the prediction with above parameters derived by LS and FFT. The following figure demonstrates that these two methods show exactly the same results,

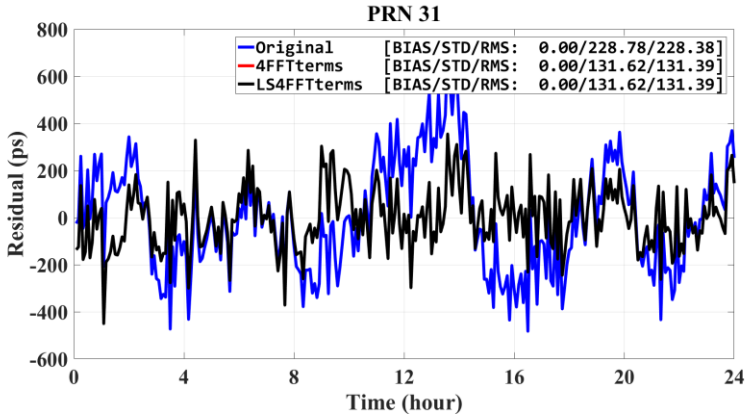

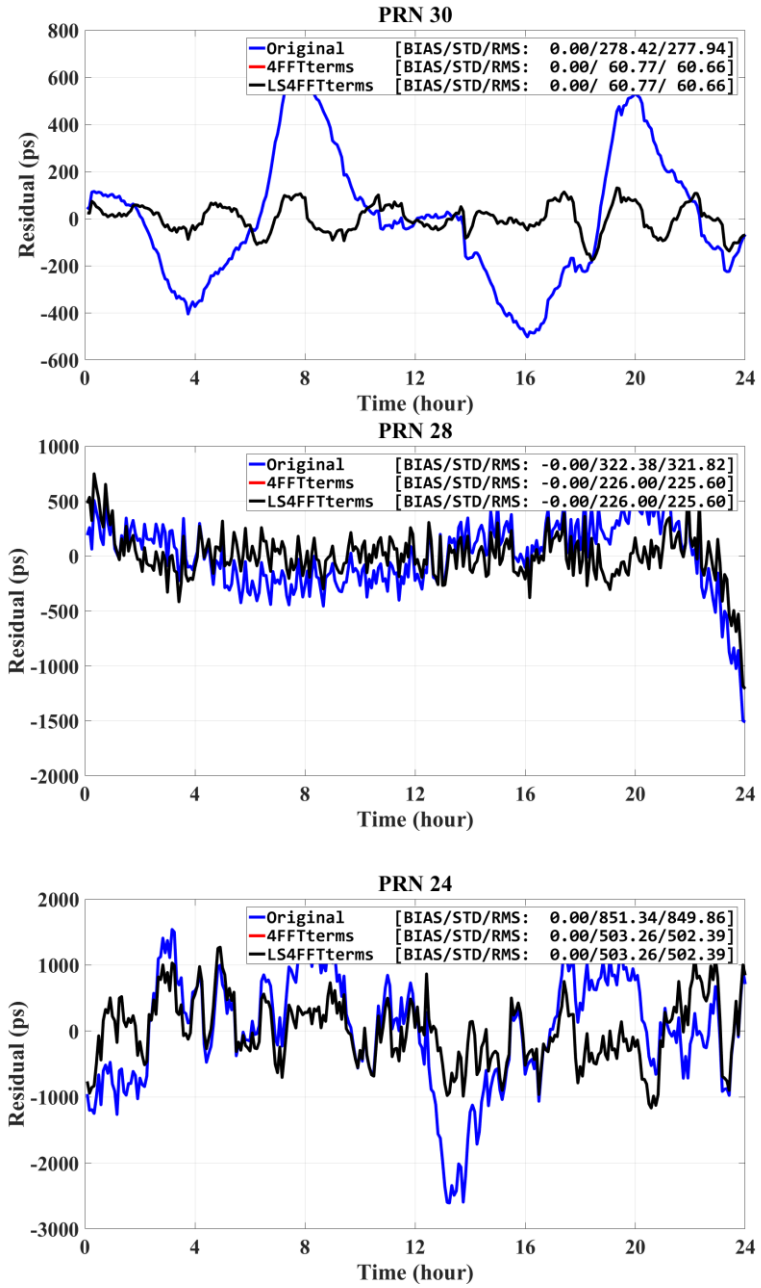

Figure 4-12 The residual after removing the polynomial terms and periodic terms PRN 31, PRN 30, PRN 28 and PRN 24

The blue line shows the first residual after the polynomial terms, while the red and black line coincides with each other, representing the second residual by removing the periodic terms from the first residual using different methods. The red line shows the results from the LS and the

black line shows the results from FFT. The results of two methods are the same for the presentation of the periodic terms.

The clock day boundary jump issue (Fritsche et al. 2014) needs to be addressed for the raw data spanning more than one day. Four GPS satellites with different types of satellite clocks, namely PRN 28 (IIR/Rb), PRN 31 (IIR-M/Rb), PRN 30 (IIF/Rb) and PRN 24 (IIF/Cs), are selected to show the day boundary jump issue. The data used here is the IGU observed clock offset (Day 360 and 361 of 2015). At the nanosecond level, the day boundary jump in Fig. 4-13 indicates that the average day boundary jump value is 0.44 ns. According to the stratagem proposed above, when the fitting arc spans over two days, the day boundary jump values will be used to shift the raw satellite clock offset of the previous day.

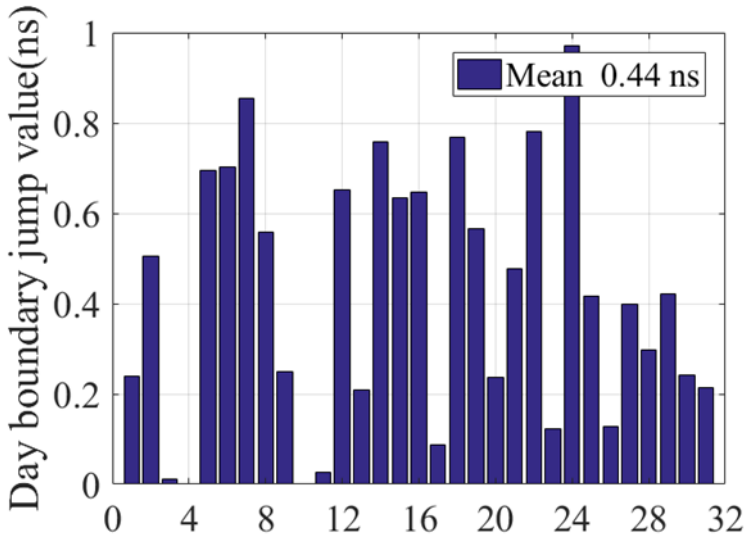

Figure 4-13 Day boundary jump values for all GPS satellites clock offsets

The method used to mitigate the day boundary jump (Yang et al. 2017b)is described as below:

$$\begin{aligned} \Delta_{Gi} &= L_{bi} - X_i \\ \dot{L}_{ai} &= L_{ai} + \Delta_{Gi} \end{aligned} \tag{4-49}$$

where

Δ_{Gi} denotes the day boundary jump for the satellite with PRN i;

L_{ai} and L_{bi} denote the satellite clock offsets of Day 1 and Day 2 correspondingly;

X_i denotes the predicted satellite clock offset for the first epoch of day 2 of PRN i;

$\dot{L}_{ai}$ denotes the satellite clock offsets of Day 1;

First, the gap value is obtained by comparing the predicted clock offset with the raw clock offsets at the first epoch of Day 2; then the gap value is applied to the raw clock offsets of Day 1 to eliminate the effect of the day boundary jump.

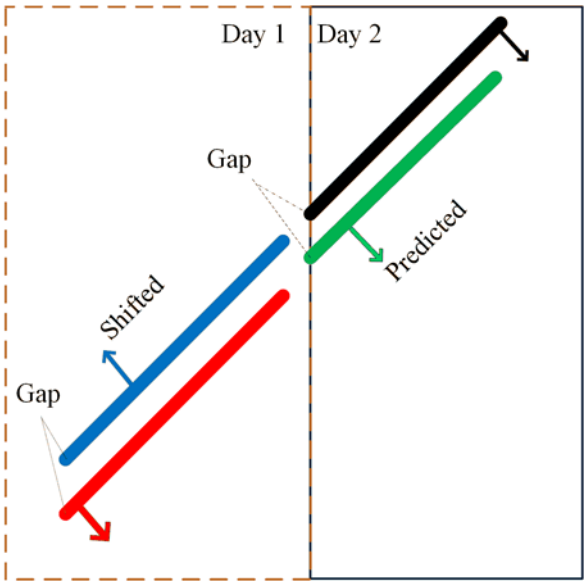

Figure 4-14 The scheme for day boundary jump mitigation

During the combination process, the satellite clock offset can be modeled as the follows,

$$Offset_{AC}^{Sat}(t) = O_{AC} + I_{AC}^{Sat} + V_{AC}^{Sat}(t) \tag{4-50}$$

in which,

O_{AC} denotes the AC specific time offset;

I_{AC}^{Sat} denotes the initial satellite specific clock offset;

$V_{AC}^{Sat}(t)$ denotes the clock offset at the time t.

For the clock corrections in IGS01, it is a single-epoch combination solution, which is completely independent. For the clock corrections in IGS03, a Kalman filter is used to combine the satellite clock corrections from various ACs.

For satellite clock product comparisons, Equation (4-50) can also be used for the explanation. First, the same reference satellite needs to be chosen to form the single difference between satellite in each product. The AC Specific O_{AC} is eliminated by this difference as shown by Equation (4-51).

$$Offset_{AC_1}^{Sat(i)}(t) - Offset_{AC_1}^{Sat(ref)}(t) = (I^{Sat(i)} - I^{Sat(ref)}) + (V_{AC_1}^{Sat(i)}(t) - V_{AC_1}^{Sat(ref)}(t)) \quad (4\text{-}51)$$

Then the difference between different products can be formed, and the equation can be written as Equation (4-52). The first part of the equation is the double-differenced satellite initial clock offset, which is interpreted as bias of the clock comparison and can be absorbed by phase ambiguities in PPP and affects the convergence by acting on the pseudo range. STD is the focus and represents the comparison results.

$$\begin{aligned}
&(Offset_{AC_1}^{Sat(i)}(t) - Offset_{AC_1}^{Sat(ref)}(t)) - (Offset_{AC_2}^{Sat(i)}(t) - Offset_{AC_2}^{Sat(ref)}(t)) \\
&= (I_{AC_1}^{Sat(i)} - I_{AC_1}^{Sat(ref)}) + (V_{AC_1}^{Sat(i)}(t) - V_{AC_1}^{Sat(ref)}(t)) - ((I_{AC_2}^{Sat(i)} - I_{AC_2}^{Sat(ref)}) + (V_{AC_2}^{Sat(i)}(t) - V_{AC_2}^{Sat(ref)}(t))) \quad (4\text{-}52) \\
&= ((I_{AC_1}^{Sat(i)} - I_{AC_1}^{Sat(ref)}) - (I_{AC_2}^{Sat(i)} - I_{AC_2}^{Sat(ref)})) + ((V_{AC_1}^{Sat(i)}(t) - V_{AC_1}^{Sat(ref)}(t)) - (V_{AC_2}^{Sat(i)}(t) - V_{AC_2}^{Sat(ref)}(t)))
\end{aligned}$$

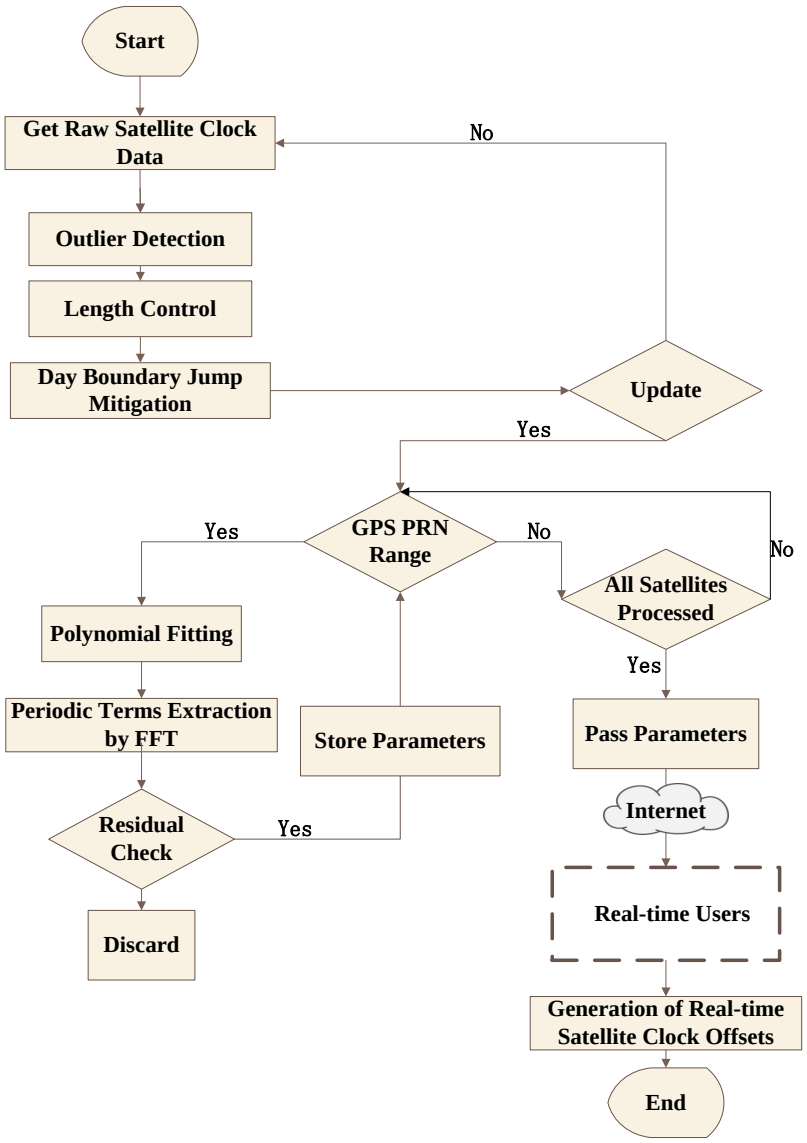

Figure 4-15 The flowchart of the satellite clock offsets prediction

The satellite clock offset prediction scheme is shown in Fig. 4-15. The first step is to obtain the raw data, which can be realized either by real-time estimating the satellite clock offsets or by receiving the IGS real-time products. The raw data will then be edited to exclude outliers, and the length of the raw data is controlled between 24 hours to 48 hours, in which the day boundary jump will be addressed later. Thirdly, for the new satellite clock offset prediction scheme, the update interval is optional, which can be flexibly set as 1 hour, 2 hours or 6 hours. The update

control is used to determine whether to predict the satellite clock offsets at the current epoch. If so, all the GPS satellites clock offsets are fitted, in which the polynomial fitting and periodic terms extraction based on the state-of-art prediction model, are carried out to generate the fitting parameters and the last epoch of raw data will be set as the reference epoch. The residual check is then implemented for each satellite clock to guarantee accuracy. If the residual check is passed, the fitting parameters are stored and then pass to the real-time users once all the GPS satellites have been processed. Finally, the high frequency satellite clock offsets can be generated.

4.2.3 New method with BRDC for RTS based prediction

In order to investigate the stability of the IGS RTS clock products, the real-time raw satellite clock offsets on July 7th of 2017 from IGS01 and IGS03 were collected and stored. Four satellites with different types of clocks are selected to present all the 31 active clocks onboard the GPS satellites, namely PRN 16, PRN 31, PRN 30 and PRN 8. The raw satellite clock offsets are shown in Fig. 4-16. The IGS03 clock products are more stable than the IGS01 clock products and the linear trend is obvious, while for IGS01 clock products, there are lots of jumps for all types of clocks.

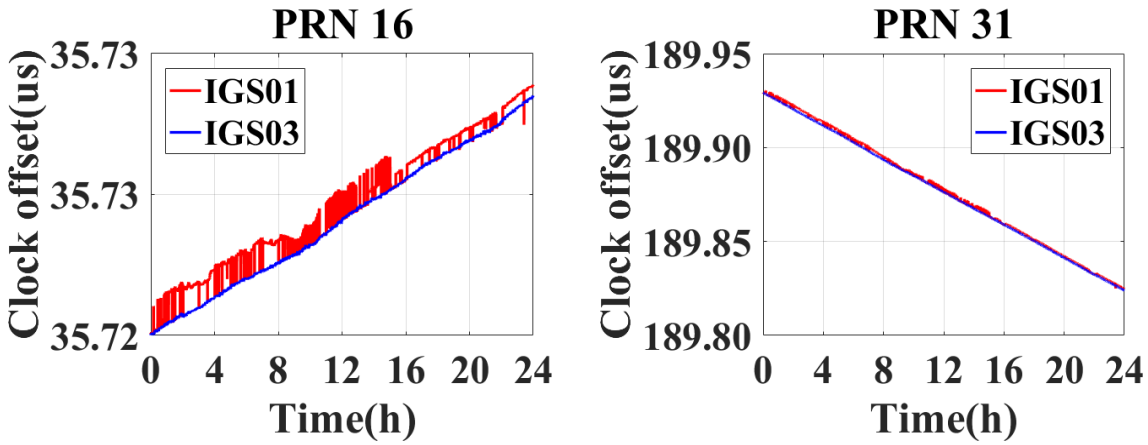

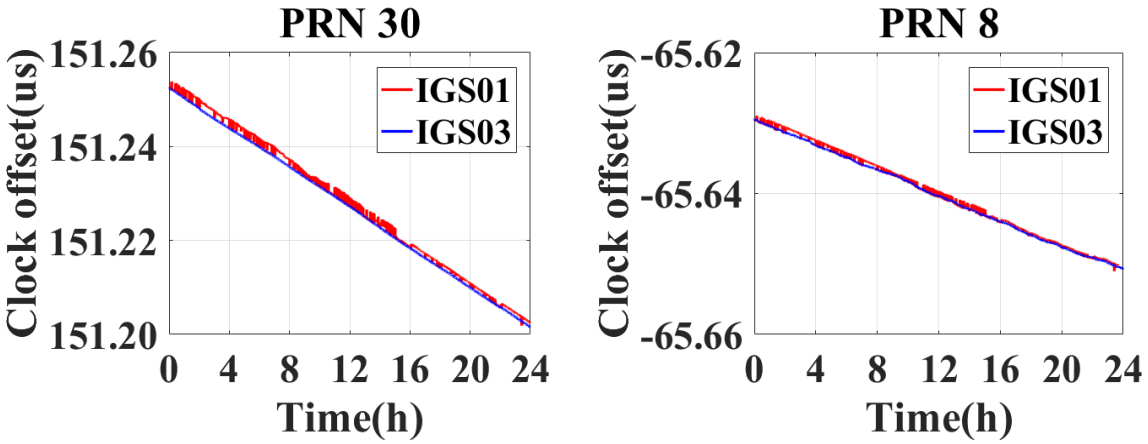

Figure 4-16 IGS01 (in red) and IGS03 (in blue) satellite clock offsets for PRN 16, PRN 31, PRN 30 and PRN 8 with one-day length

The mean offset rate for the above four satellites clocks is also calculated by differencing satellite clock offsets between consecutive epochs, as shown in Fig. 4-17. The IGS final clock products with a sample rate at 30 seconds for the same day are downloaded and used here as the reference. The magnitude of the mean offset rate for IGS01 can be more than 1 ns per second due to the jump, which is much larger than that of IGS03. The mean offset rates for the IGS03 and the IGS final clock products have the same magnitude at a level of several tens ps per second. Another phenomenon which should be mentioned is that the big jumps for different satellites seem to occur at the same time, which may be due to different strategies adopted for IGS clock combinations.

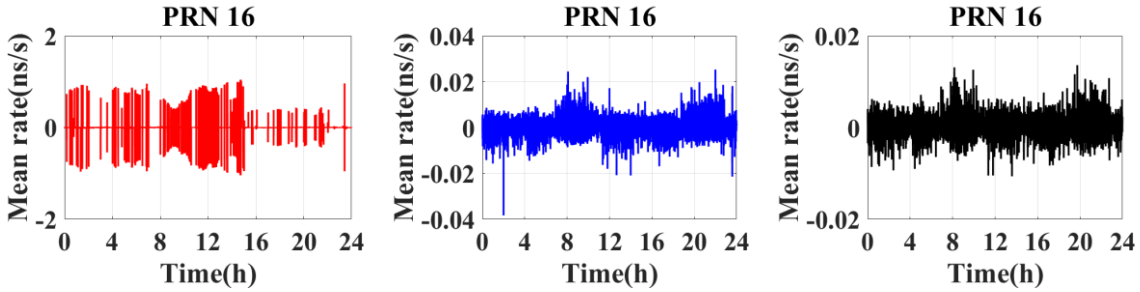

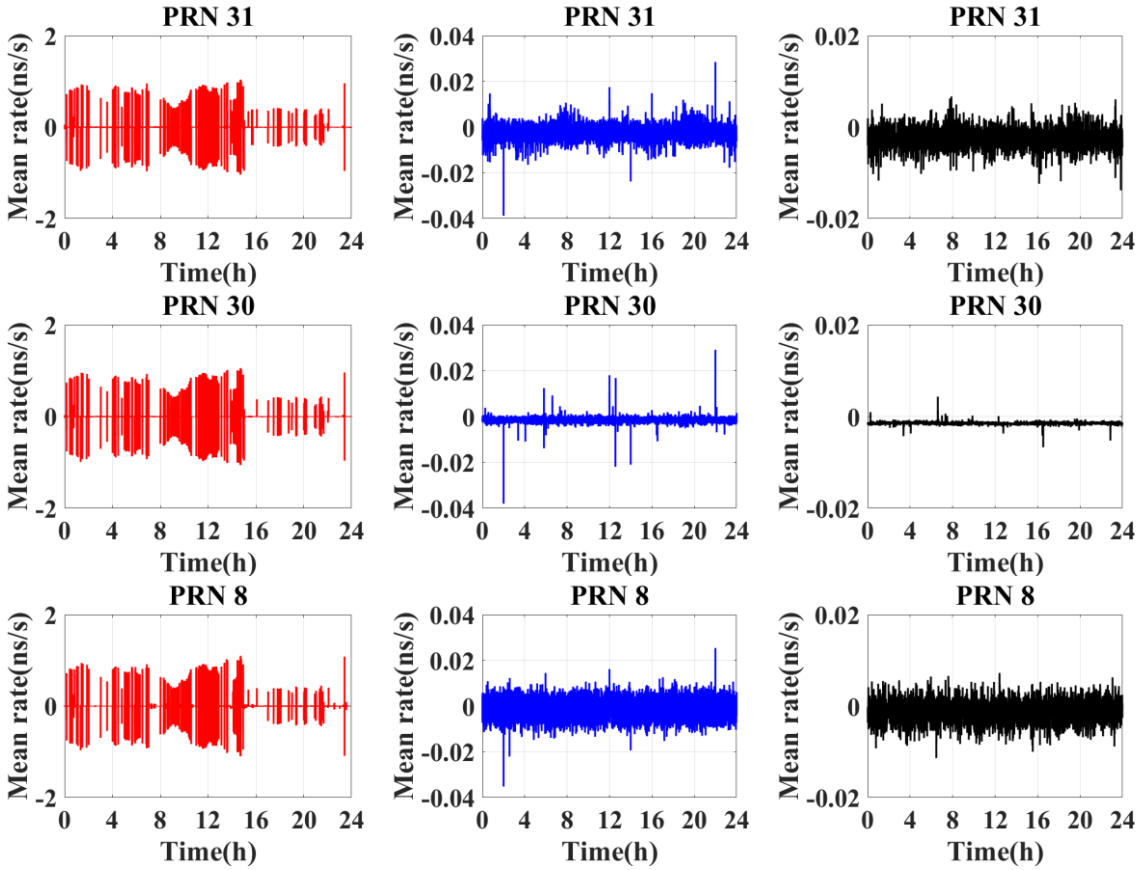

Figure 4-17 Mean clock offset rates of IGS01, IGS03 and IGS final products for PRN 16, PRN 31, PRN 30 and PRN 8

Additionally, the Allan Variance is applied to analyze the stability of different clock products. The Allan Variances of the PRN 16, PRN 31, PRN 30 and PRN 8 from IGS01, IGS03 and IGS final products are shown in Fig. 4-18. It is obvious the IGS01 has the poorest stability while the performance of the IGS03 and the IGS final products are quite similar in terms of the Allan Variance. The Cs clocks onboard GPS IIF satellites show the poorest stability among the four selected satellite clocks.

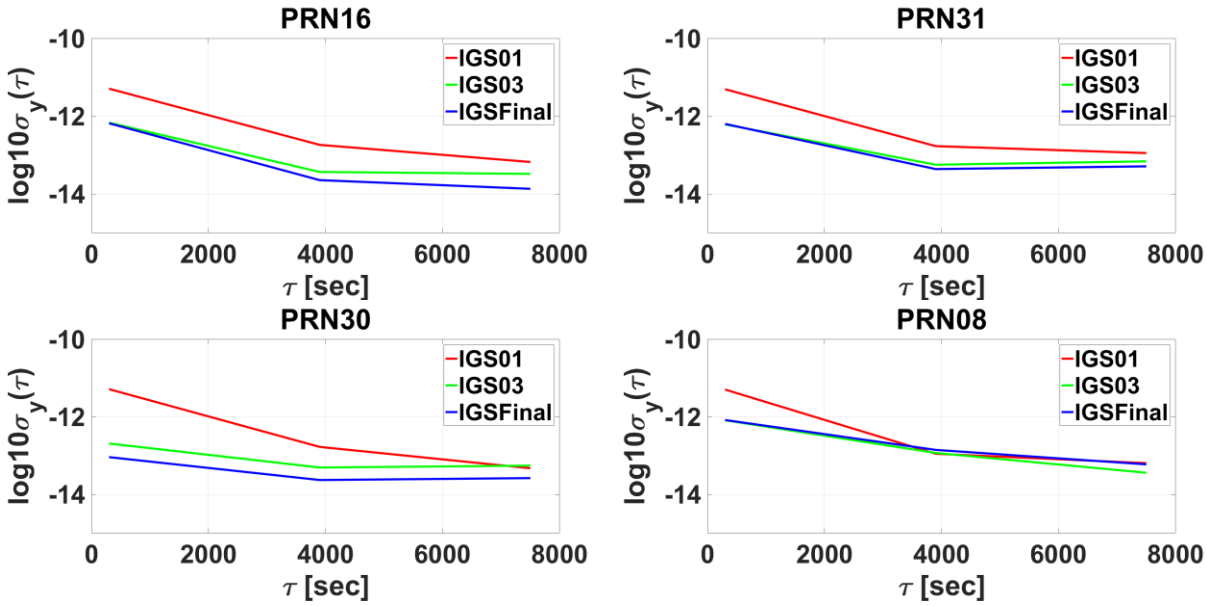

Figure 4-18 Allan Variance of PRN 16, PRN 31, PRN 30 and PRN 8 from IGS01, IGS03 and IGS final products

A new satellite clock offsets prediction method is proposed below based on the IGS RTS products and the prediction model for each satellite clock can be expressed as,

$$x(t)^j - x_{tref}{}^j = y_0{}^j t + \frac{\beta z_0{}^j t^2}{2} + \sum_{l=0}^{k} A_l{}^j \sin(\omega t + \varphi_l{}^j) + \Psi(t)^j \qquad (4\text{-}53)$$

$$y_{Brdc}{}^j = y_0{}^j, \qquad \delta^{j2}$$

where,

y_{Brdc} denotes the satellite clock drift from the latest broadcast ephemeris;

x_{tref} denotes the satellite clock offset from RTS;

δ denotes the standard deviation term for y_{Brdc};

j denotes the GPS PRN.

The other parameters have the same meanings as in Equation 4-46. In this new prediction model for each satellite, the first polynomial term is not included in the estimation and the satellite

clock offset at the epoch closest to the current epoch will be directly used. The clock drift from the broadcast ephemeris is used in the estimation process as pseudo-observations. All the satellite clocks are predicted together and the actual prediction model for all satellites can be expressed as:

$$\begin{aligned}
x(t)^1 - x_{tref}{}^1 &= O_{AC} + y_0{}^1 t + \frac{\beta z_0{}^1 t^2}{2} + \sum_{l=0}^{k} A_l^1 \sin(\omega t + \varphi_l^1) + \Psi(t)^1, \\
y_{Brdc}{}^1 &= y_0{}^1, \qquad \delta^{1^2} \\
x(t)^2 - x_{tref}{}^2 &= O_{AC} + y_0{}^2 t + \frac{\beta z_0{}^2 t^2}{2} + \sum_{l=0}^{k} A_l^2 \sin(\omega t + \varphi_l^2) + \Psi(t)^2, \\
y_{Brdc}{}^2 &= y_0{}^2, \qquad \delta^{2^2} \\
&\vdots \\
x(t)^j - x_{tref}{}^j &= O_{AC} + y_0{}^j t + \frac{\beta z_0{}^j t^2}{2} + \sum_{l=0}^{k} A_l^j \sin(\omega t + \varphi_l^j) + \Psi(t)^j, \\
y_{Brdc}{}^j &= y_0{}^j, \qquad \delta^{j^2}
\end{aligned} \tag{4-54}$$

The above equations indicate that all GPS satellite clocks are predicted together while O_{AC} is added in the estimation process to mitigate the jump issue. The jump is assumed to be caused by datum change in the combination process for all satellite clocks in the same epoch. O_{AC} is the same for all satellite clocks at the same epoch but varies over different epochs. In the filter, each satellite clock is modeled by two polynomial parameters and 2*k periodic parameters (k is usually set as 2 or 4). O_{AC} is estimated as random walk parameters. When the total epoch number is m and satellite number at an epoch in the RTS products is n, the filter can be solved as long as the following requirement can be met.

$$m \times n > m + n \times (2 + 2 \times k) \tag{4-55}$$

For example, if k equals to 4 and n equals to 31, the epoch number will be larger than 11. For IGS01 and IGS03, the minimum lengths for fitting are 11*5 seconds and 11*10 seconds, respectively.

The proper weighting for broadcast satellite clock drifts as pseudo-observations are essential in the new method. In order to investigate the accuracy of the satellite clock drift from broadcast ephemeris, the broadcast ephemeris and IGS final clock products for the whole year of 2016 are downloaded. The satellite clock drifts calculated from the IGS final clock products are used as a reference. The satellite clock drifts from both broadcast ephemeris and IGS final clock products for PRN 16, PRN 31, PRN 30 and PRN 8 are shown in Fig. 4-19. As shown, the satellite clock drifts have a linear trend for PRN 16, PRN 31 and PRN 30. PRN 30 has the largest drift rate and the clock drift over one year is more than 4 picoseconds per second. For GPS PRN 8, the satellite clock drift does not have linear trend and the value ranges in -2 picoseconds per second to -1 picoseconds per second. The satellite clock drifts from broadcast ephemeris can maintain the same value for several days.

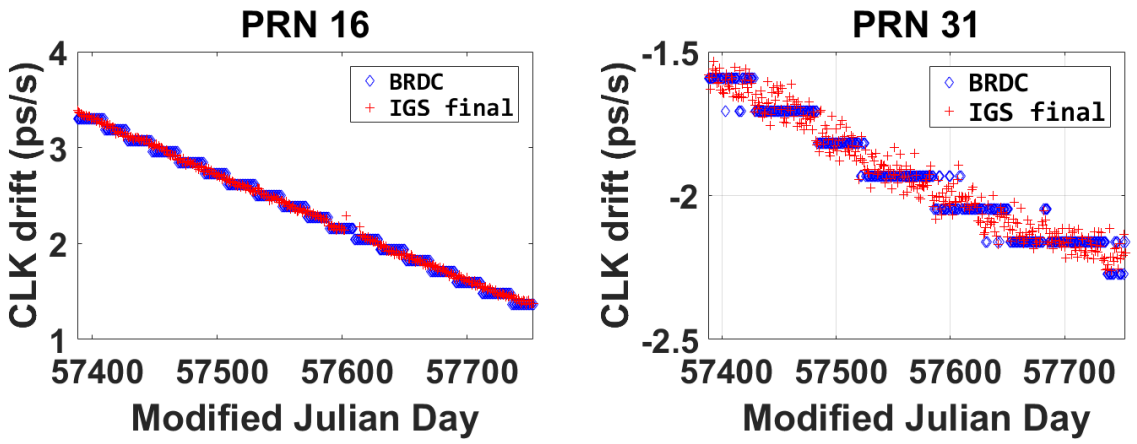

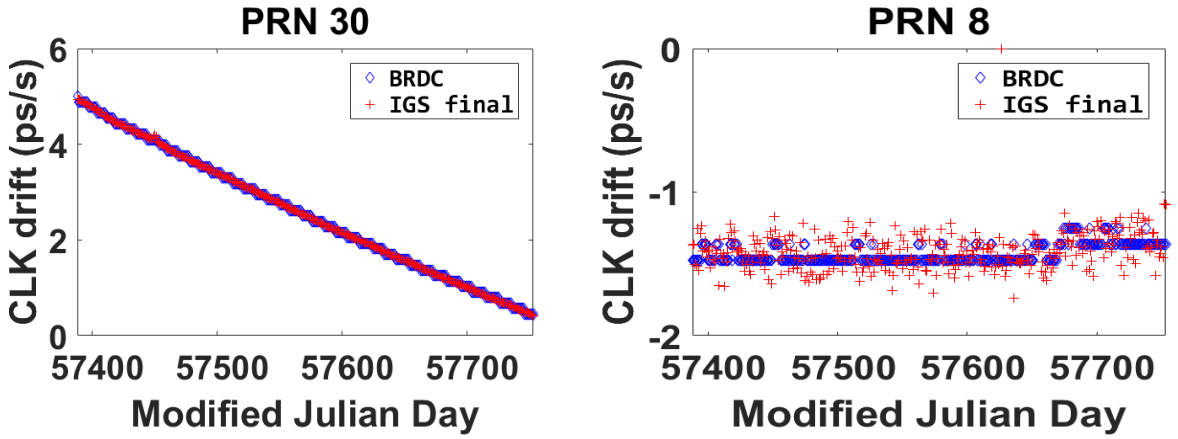

Figure 4-19 Satellite clock drifts of PRN 16, PRN 31, PRN 30 and PRN 8 from broadcast ephemeris and IGS final clock products over 2016

The differences between satellite clock drifts from the broadcast ephemeris and IGS final clock products are calculated over the year 2016 and the RMS are computed accordingly for each satellite, as shown in Fig. 4-20. The RMS for most satellite clocks are smaller than 0.05 picosecond per second and the average RMS of all satellites is 0.05 picosecond per second. The RMS for GPS PRN 8, PRN 24, PRN 28 and PRN 32 are larger than 0.1 picosecond per second. The RMS for each satellite will be used for the weighting of the satellite clock drifts from broadcast ephemeris as pseudo-observations.

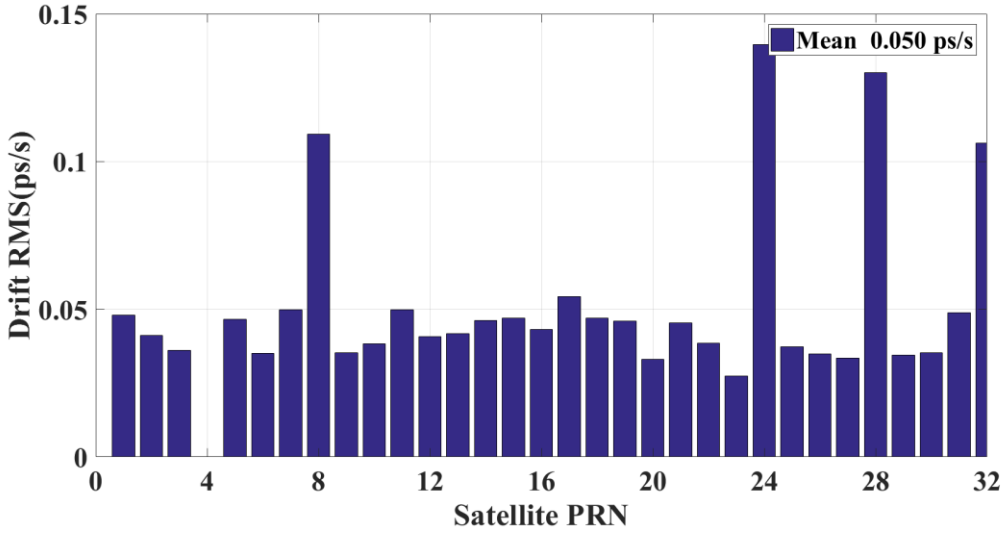

Figure 4-20 Satellite clock drifts RMS of broadcast ephemeris for all GPS satellites

4.3 Summary

In Chapter 4, the methods and algorithms for the generation of satellite orbit and clock IP at the server end are described. For the satellite orbit IP generation, the primary forces models are introduced, including Earth gravitation, lunar and solar gravitation, solid Earth tide, ocean tide and solar radiation pressure. Regarding to the magnitudes, the Earth's gravitational acceleration has the largest effect on satellite motion, and the magnitude can be several 1×10^{-1} m/s^2. The solar and lunar gravitational acceleration also have significant effects on satellite orbit, with a magnitude both at several 1×10^{-6} m/s^2. The SRP acceleration is quite stable over one day, with a magnitude at 1×10^{-7} m/s^2. The variation equations with respect to the orbit IP is then explained, followed by the single-step and multi-step numerical integrators. The estimation of the orbit IP is then introduced. For the satellite clock IP generation, the current clocks onboard GPS satellites are introduced and compared for ages and stabilities. The results indicate Cs clocks onboard GPS IIF satellites have the lowest stability. The satellite clock offsets prediction

models are introduced, in which the effects of the periodic terms are investigated. The results indicate 12 h and 6 h are the two main periods for all the satellites. A new satellite clock offsets prediction model is proposed in this chapter as well, in which the broadcast ephemeris is used as a constraint and all the satellite clocks are predicted together.

CHAPER FIVE: PRECISE ORBIT AND CLOCK OFFSETS PREDICTION USING IP AT USER END

In this chapter, the precise satellite orbit and clock offset prediction are carried out at user end with received IP products, which is generated at the server end. In Section 5.1, the method for precise satellite orbit prediction with orbit IP is presented and the predicted orbits are evaluated. The precise satellite clock offsets prediction with clock IP is carried out in Section 5.2. The prediction with clock IP of scalable update rates is investigated.

5.1 Precise Satellite Orbit Prediction with Orbit IP at User end

Once the orbit IP, including position $r^0_{3\times 1}$, velocity $v^0_{3\times 1}$ and SRP vector $p^0_{9\times 1}$ are known, the satellite orbit at time t_{k} can be generated with the abovementioned numeric integrator, which can also be expressed as a function of all the related parameters:

$$\tilde{\boldsymbol{r}}_k = \boldsymbol{h}(t_k, \vec{\boldsymbol{a}}, r^0_{3\times 1}, \boldsymbol{v}^0_{3\times 1}, \boldsymbol{p}^0_{9\times 1}) \tag{5-1}$$

The real-time satellite orbits from the day of the year (DOY) 105 to 111 of 2017 are obtained from IGS RTS through the Internet. The stream used in the experiment is the IGS01 with 5 seconds update rate for satellite orbit (encoded in RTCM message type 1060). The IGS final products from DOY 106 to 112 of year 2017 are downloaded via ftp as the reference. Additionally, the satellite reference center for IGS01 is transferred from the antenna phase center to the satellite center of mass before the prediction, with the phase center offsets derived from the IGS antenna files. In this section, satellites with PRN 2, PRN 3, PRN 5, and PRN 24 representing different kinds of GPS satellites, are selected to make the orbit prediction on DOY 109 of 2017. As shown in Fig. 5-1, the orbit prediction error over 12 hours is smaller than 5 cm

for all four satellites in the radial, along-track, and cross-track directions. The average RMSE of the predicted orbit over 12 h for all four satellites is 0.027 m, 0.024 m, and 0.032 m for the radial, along-track and cross track directions, respectively.

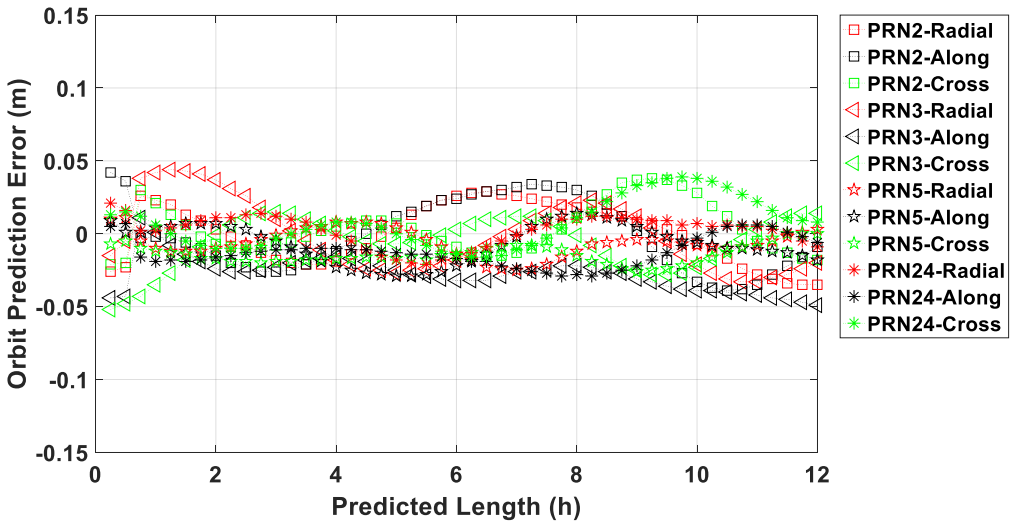

Figure 5-1 Orbit prediction error in the radial, along-track and cross-track directions over 12 h on DOY 109 of 2017 for GPS satellite PRN 2, PRN 3, PRN 5 and PRN 24.

The GPS satellite orbit prediction is then carried out from DOY 106 to 112 of year 2017. For each day, the satellite orbit is predicted for 12 h, and then the average RMSE values for the whole week are calculated. The average RMSE of the orbit prediction is shown in Fig. 6-2. The average RMSE values in all three directions are smaller than 0.060 m for all GPS satellites, and the average RMSE in three directions are similar. The average RMSE values of the 31 satellites are 0.031 m, 0.032 m, and 0.033 m for the radial, along-track and cross-track directions.

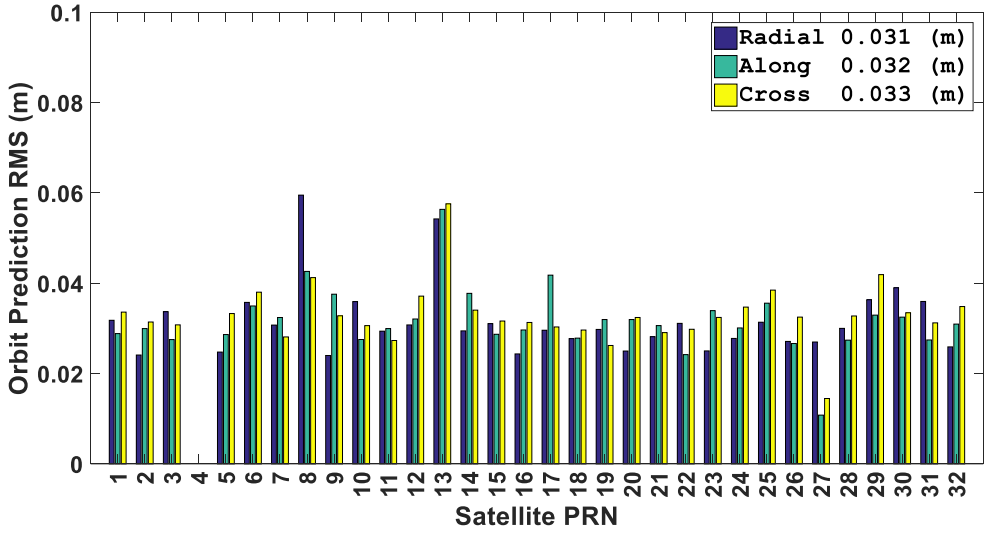

Figure 5-2 Average orbit prediction RMSE over 12 h of all GPS satellites from DOY 106 to 112 of 2017.

To investigate the effects of the orbit on positioning, the SISRE (orb) are calculated according to the following equation.

$$\text{SISRE(orb)} = \sqrt{w_R^2 \cdot R^2 + w_{A,C}^2 \left(A^2 + C^2\right)} \tag{5-2}$$

where

w_R denotes the statistical constribution of radial (R);

$w_{A,C}^2$ denotes the statistical constribution of along-track (A) and cross-track (C) errors to the line-of-sight ranging error.

For GPS, w_R and $w_{A,C}^2$ are 0.98 and 1/49 respectively (Montenbruck et al. 2015b). The average RMSE of all satellites and SISRE over different periods, from 1 h to 12 h, is plotted in Fig. 5-3.

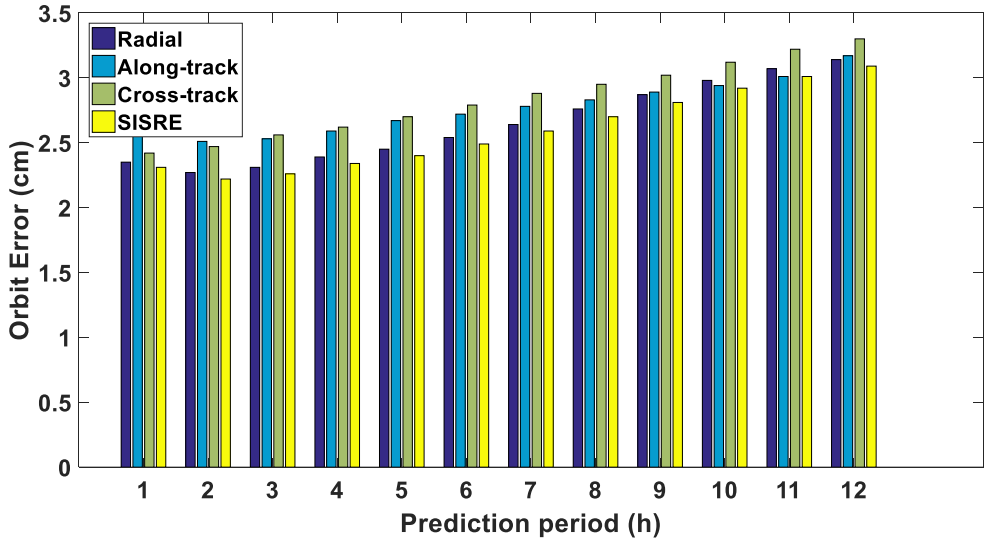

Figure 5-3 Average RMSE of the predicted GPS satellite orbit over 12 h

The primary trend of the RMSE of the predicted orbit increases gradually with the prediction periods. The average RMSE is 2.35 cm, 2.58 cm, and 2.42 cm for the predicted orbit over 1 h in radial, along-track, and cross-track directions, respectively. For predictions over 6 h, the average RMSE increases slightly to 2.54 cm, 2.72 cm, and 2.79 cm in each of the three directions. Even for predictions over 12 h, the average RMSE is 3.14 cm, 3.17 cm, and 3.30 cm. For the SISRE(orb), the value increases from 2.31 cm to 3.09 cm with the prediction periods. To investigate the accuracy of the predicted orbit more thoroughly, experiments in positioning domain are carried out.

For the static PPP, the GPS observation data from 32 globally distributed stations are downloaded through ftp on DOY 108 of 2017, as shown in Fig. 5-4.

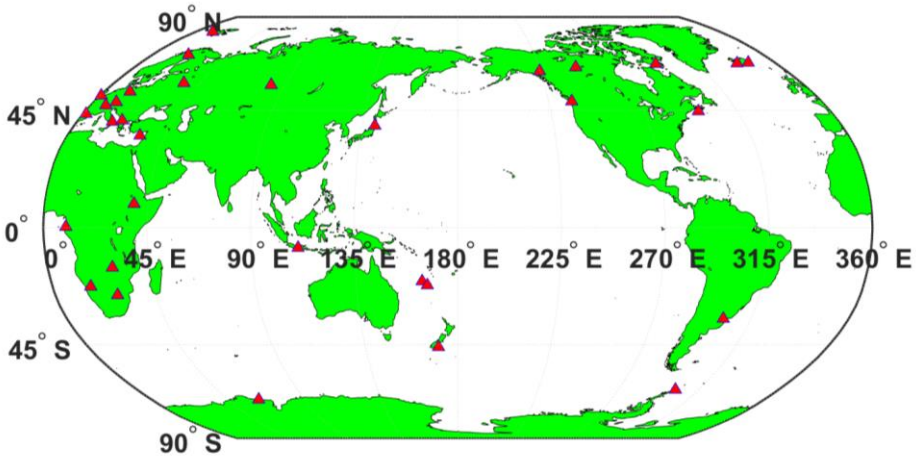

Figure 5-4 The distribution of the selected IGS stations for static PPP tests

The static PPP experiment is carried out on 18th April 2017 for 12 hours and the predicted satellite orbit and the IGS final clock products with 30 s sample rate are used. The detailed settings of the PPP filter are listed in Table 5-1.

Table 5-1 Filter settings for the PPP.

	Settings
Constellation	GPS satellites
Combination mode	Ionosphere-free phase and code combinations
Signal selection	GPS L1/L2
Sampling rate	1 s
Elevation mask	7°
Observation weight	Elevation dependent weight
Tropospheric zenith hydrostatic delay	GPT model
Tropospheric zenith wet delay	Initial model + estimated
Troposphere mapping function	GMF
Phase wind-up	Corrected
Sagnac effect, relativistic effect	IS-GPS-200
Satellite/receiver phase center	Corrected with IGS absolute correction model
Solid tides effect	IERS conventions (Gérard and Luzum 2010)
Receive clock	Estimated, white noise
Station coordinates	Estimated

The basic filter settings for the PPP are listed in the following table, and the station coordinates are estimated along with the receiver clock, tropospheric zenith wet delay, and ambiguity parameters. The reference coordinates for all the IGS stations are obtained from the Scripps Orbit and Permanent Array Center. The static PPP accuracy is shown in Fig. 5-5 and the RMSE values for all the selected stations are less than 5 cm in all three directions. The variety in positioning accuracy is due to different visibility of the satellites as well as the geometry. For stations like MAW1, the positioning RMSE values are around 1 cm for all three directions, while the vertical positioning RMSE of WIND station can reach around 4 cm. When all stations are averaged, the positioning RMSE values are 0.012 m, 0.015 m, and 0.021 m for the north, east and vertical directions, respectively.

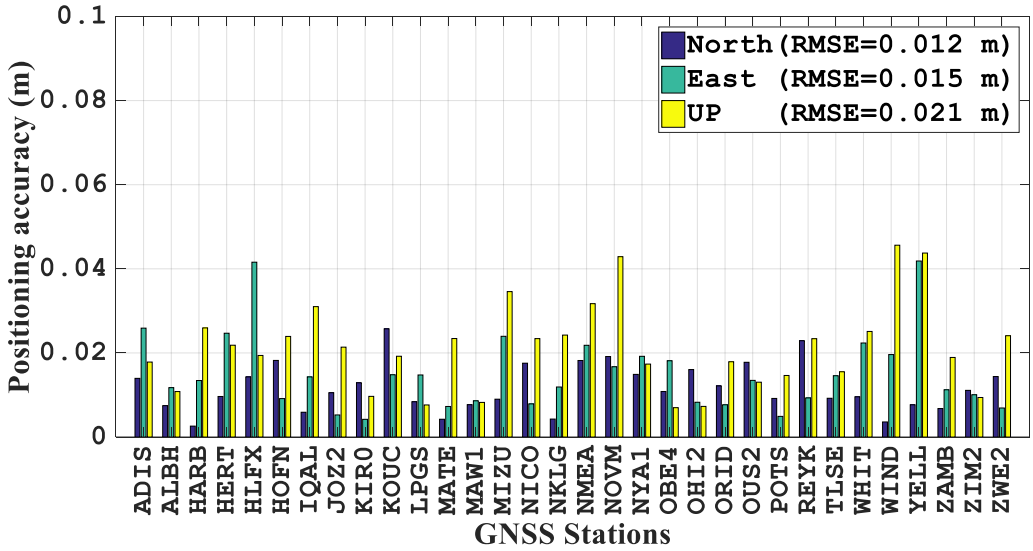

Figure 5-5 Positioning accuracy of 32 globally distributed IGS stations on 18 April 2017 with the predicted GPS orbit

5.2 Precise Satellite Clock Offsets Prediction with Clock IP at User End

To assess the effectiveness of the satellite clock offsets prediction scheme and the model introduced above, the tests results are first verified by comparing to an external reference, and then the predicted satellite clock offsets are applied to a real-time PPP system. The comparison is carried out between the predicted clock offsets, with an update interval of 24 hours, and the IGU observed clock offset over the whole GPS week 1877. The accuracies of the predicted satellite clock offsets are shown in Fig. 5-6.

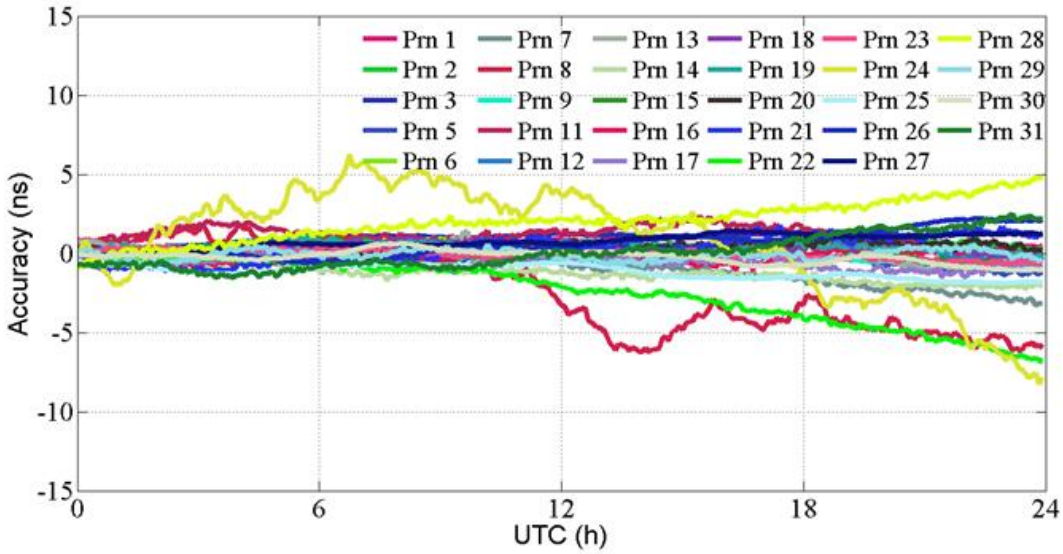

Figure 5-6 The predicted satellite clock offsets of all the GPS satellites

The prediction errors grow with the prediction period and can be around 5 ns for some satellites with prediction over one day. The prediction error of IIF/Cs clock diverges quickly to more than 5 ns, which further confirms the instability of the satellite IIF/Cs clock. Statistics are provided in Table 5-2. For prediction over 1 hour, the STD of IIR/Rb, IIR-M/Rb, IIF/Rb and IIF/Cs clocks is 0.17 ns, 0.22 ns, 0.09 ns and 0.90 ns. For prediction over 6 hours, the STD of IIR/Rb, IIR-M/Rb and IIF/Rb is smaller than 0.40 ns while the STD of IIF/Cs is 2.04 ns.

Table 5-2 The statistics of the prediction error of different types of satellite clocks (ns)

	$\tau_p = 1\ hour$	$\tau_p = 3\ hours$	$\tau_p = 6\ hours$
	RMS/STD	**RMS/STD**	**RMS/STD**
IIR/Rb	0.41/0.17	0.47/0.27	0.62/0.30
IIR-M/Rb	0.35/0.22	0.42/0.26	0.61/0.39
IIF/Rb	0.24/0.09	0.39/0.20	0.60/0.38
IIF/Cs	1.12/0.90	1.25/1.17	1.83/2.04

To demonstrate the advantages of prediction with short update intervals over the IGU products further, the kinematic PPP is carried out and the settings are shown in Table 6-3.

Table 5-3 Satellite orbit and clock products utilized in the kinematic real-time PPP

Experiments	**Clock Update Interval**	**Predicted Orbit**	**Predicted Clock**
Set 1	1h	From IGU	From clock model
Set 2	No update	From IGU	From IGU

The observation data of the 22 IGS stations globally distributed as shown in Fig. 5-7 are downloaded from the CDDIS to investigate the kinematic positioning performance for 6 hours. Then the kinematic PPP results of 6 hours for all the stations are presented in Fig. 5-8.

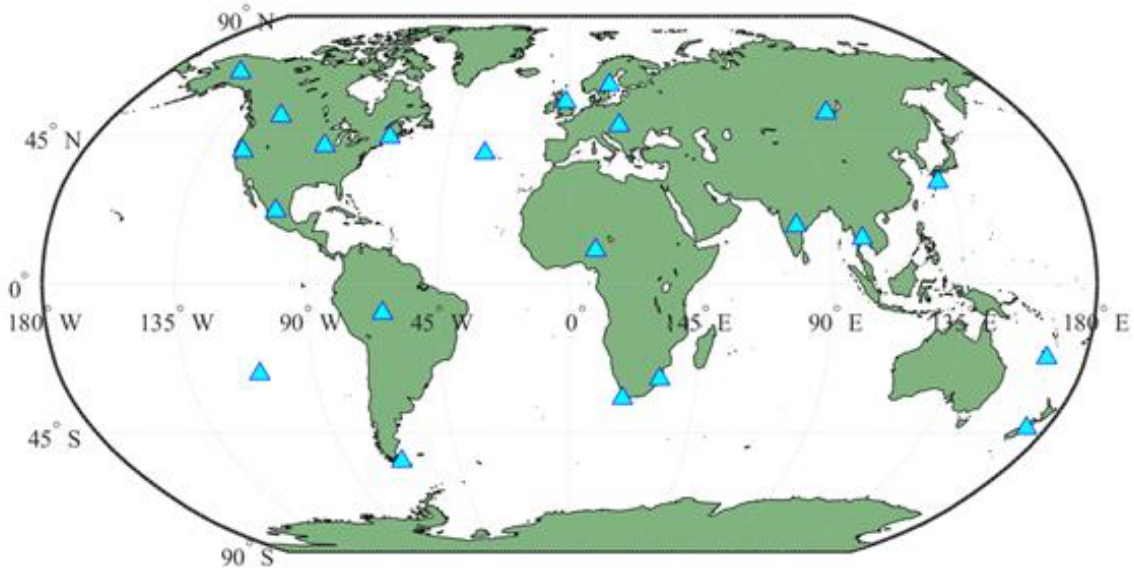

Figure 5-7 The distribution of the 22 selected IGS stations

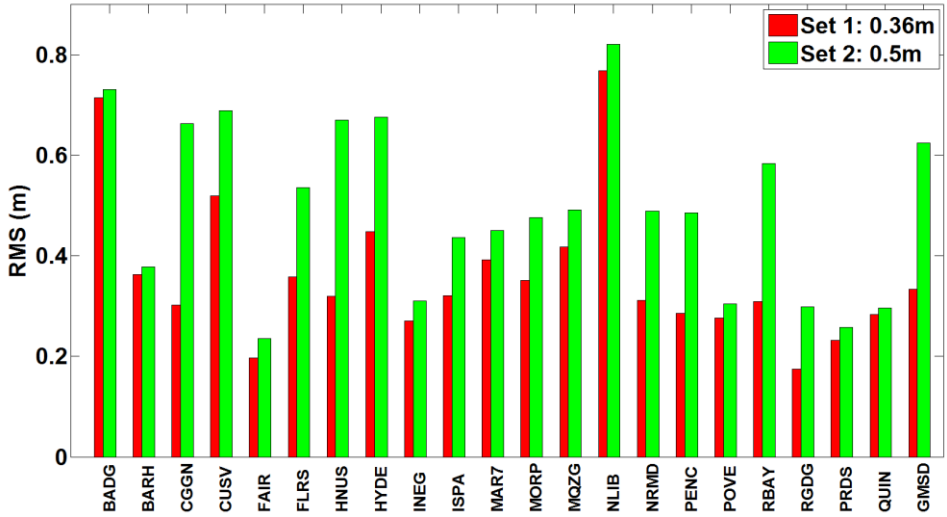

Figure 5-8 The RMS of kinematic PPP result for two different sets over 6 hours

As shown in Fig. 5-8 that the proposed satellite clock offsets prediction scheme with update interval at 1 hour outperforms the IGU products at all the stations. The positioning results vary with the location of observation stations for the visible satellites are different. The average RMS of the kinematic PPP with all stations is 0.360 m with updating every hour while the average RMS of the kinematic PPP results utilizing the IGU products is 0.500 m, with improvement as high as 28%. More detailed statistics in horizontal and vertical directions are given in Table 5-4. As shown, the best positioning accuracy can reach 0.196 m for stations like FAIR while some are over 0.769 m for stations like NLIB. For some stations, such as FAIR, INEG, ISPA and POVE and so on, the kinematic PPP RMS in the horizontal direction can reach centimeter level with one-hour update interval. When comparing Set 1 with Set 2, the accuracy improvement also differs for the selected stations, and the largest improvement is 0.361 m obtained at CGGN while the smallest improvement is 0.016 m at BADG, the main reason for the difference is due to the

various improvements for different satellite clocks and visible satellites are different for the selected stations.

Table 5-4 RMS of the kinematic PPP with 22 IGS stations

	Horizontal (m)		Vertical (m)		Three Dimension (m)	
Stations	1 h	IGU	1 h	IGU	1 h	IGU
BADG	0.187	0.203	0.690	0.702	0.715	0.731
BARH	0.305	0.302	0.196	0.227	0.363	0.378
CGGN	0.122	0.145	0.276	0.647	0.302	0.663
CUSV	0.227	0.235	0.467	0.648	0.519	0.689
FAIR	0.085	0.121	0.177	0.203	0.196	0.236
FLRS	0.174	0.232	0.313	0.483	0.358	0.535
HNUS	0.146	0.259	0.284	0.619	0.320	0.671
HYDE	0.289	0.399	0.343	0.545	0.449	0.676
INEG	0.063	0.157	0.263	0.267	0.270	0.310
ISPA	0.079	0.139	0.311	0.414	0.321	0.437
MAR7	0.182	0.266	0.347	0.364	0.392	0.456
MORP	0.105	0.202	0.335	0.431	0.351	0.476
MQZG	0.209	0.234	0.362	0.433	0.418	0.492
NLIB	0.469	0.518	0.609	0.637	0.769	0.821
NRMD	0.109	0.199	0.292	0.447	0.312	0.489
PENC	0.097	0.157	0.269	0.459	0.286	0.485
POVE	0.086	0.186	0.263	0.241	0.277	0.304
RBAY	0.199	0.285	0.236	0.509	0.309	0.584
RGDG	0.059	0.109	0.164	0.279	0.174	0.299
PRDS	0.183	0.191	0.141	0.174	0.231	0.258
QUIN	0.155	0.167	0.238	0.244	0.284	0.296
GMSD	0.113	0.301	0.314	0.548	0.333	0.625

In this section, the satellite clock offsets prediction will be carried out with the proposed method mainly focused on IGS RTS clock products. The satellite clock products of IGS01 and IGS03 on July 7th of 2017 are used for prediction. The IGS final clock products at the same period are used as reference of the evaluation. The satellite clock offsets data from 12:30 pm to 12:36 pm are used for fitting, which is shown in Fig. 5-9.

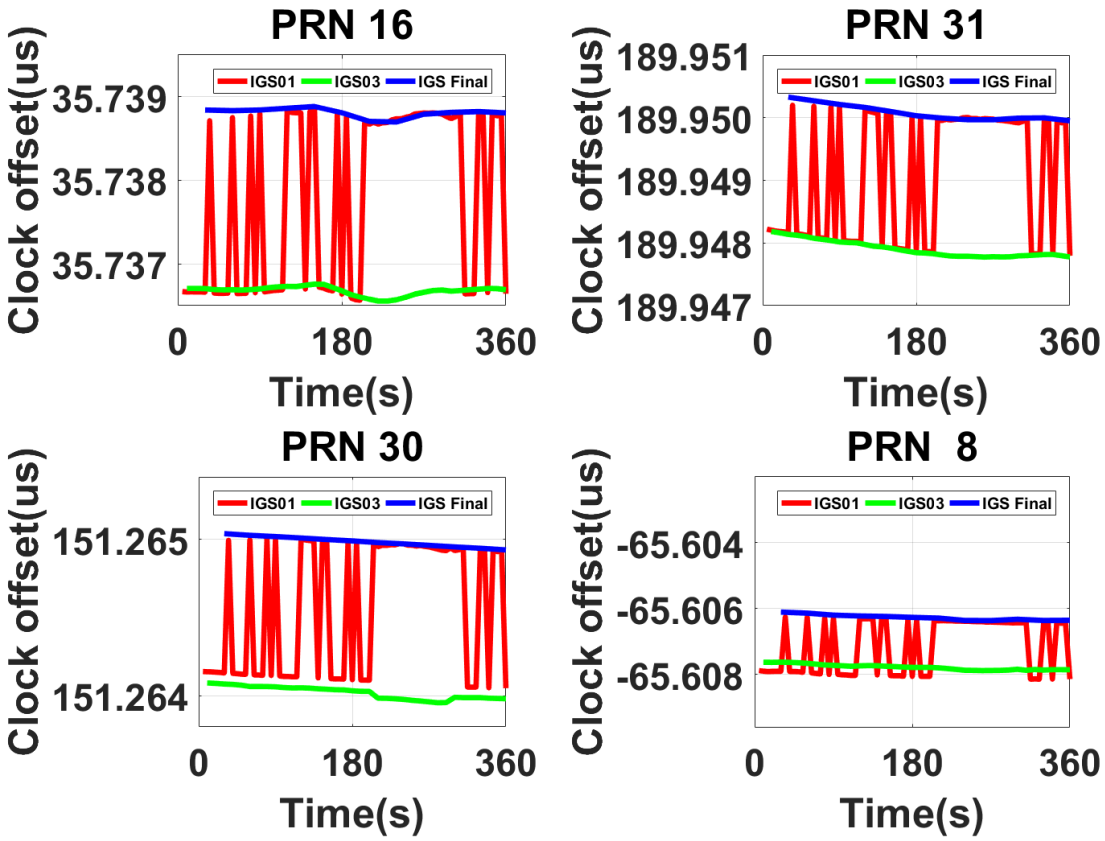

Figure 5-9 Satellite clock offsets of IGS01, IGS03 and IGS final products for fitting

As shown in Fig. 5-9, the IGS03 and IGS final have quite a similar trend over time and the bias between them is at nanosecond level for the four selected satellites clocks. The satellite clock offsets from IGS01 showed different characters and frequently jumped during the selected 6 minutes. The total epoch numbers of the IGS01, IGS03 and IGS final are 72, 36 and 12 correspondingly with different sample rates at 5 seconds, 10 seconds and 30 seconds, respectively. The satellite clock offsets prediction with the traditional method and proposed method are compared for IGS01, IGS03 and IGS final. The satellite clock drifts of IGS01, IGS03 and IGS final derived from the traditional method are shown in Fig. 5-10.

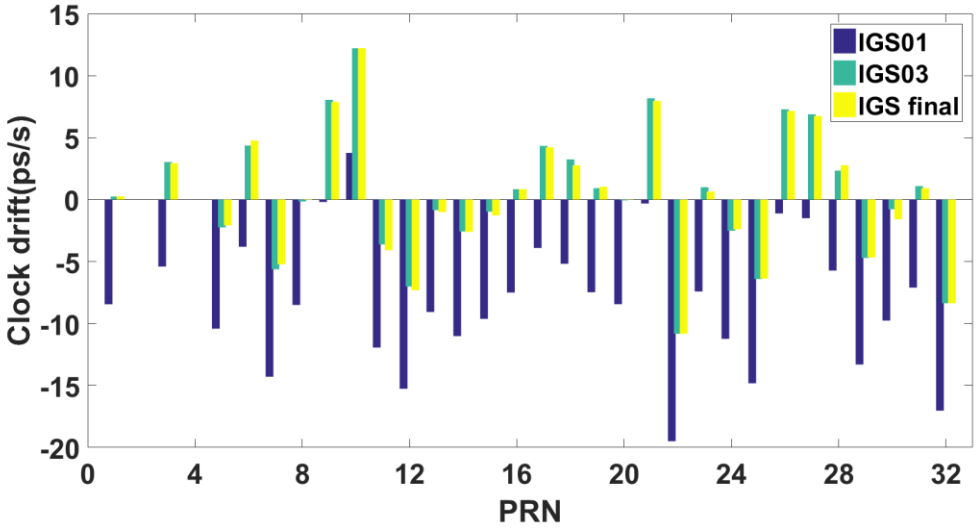

Figure 5-10 Satellite clock drifts obtained with traditional prediction method for IGS01, IGS03 and IGS final products

As shown in Fig. 5-10, the satellite clock drifts for IGS03 and IGS final products with the traditional satellite clock offsets prediction method are similar while the results of IGS01 are quite different. The main reason for the differences is the jumps in the satellite clock offsets data from IGS01. For satellites such as PRN 1 and PRN 5, the clock drifts differences between IGS01 and IGS final products can be more than 5 picoseconds per second, which equals to 4.5 ns difference with prediction over half hour. Meanwhile, the residuals of IGS01, IGS03 and IGS final after fitting are shown in Fig. 5-11. The residuals of IGS01 products are very large, which presents poor internal reliability. The residuals of IGS03 and IGS final products are much smaller and the values are less than 1 ns.

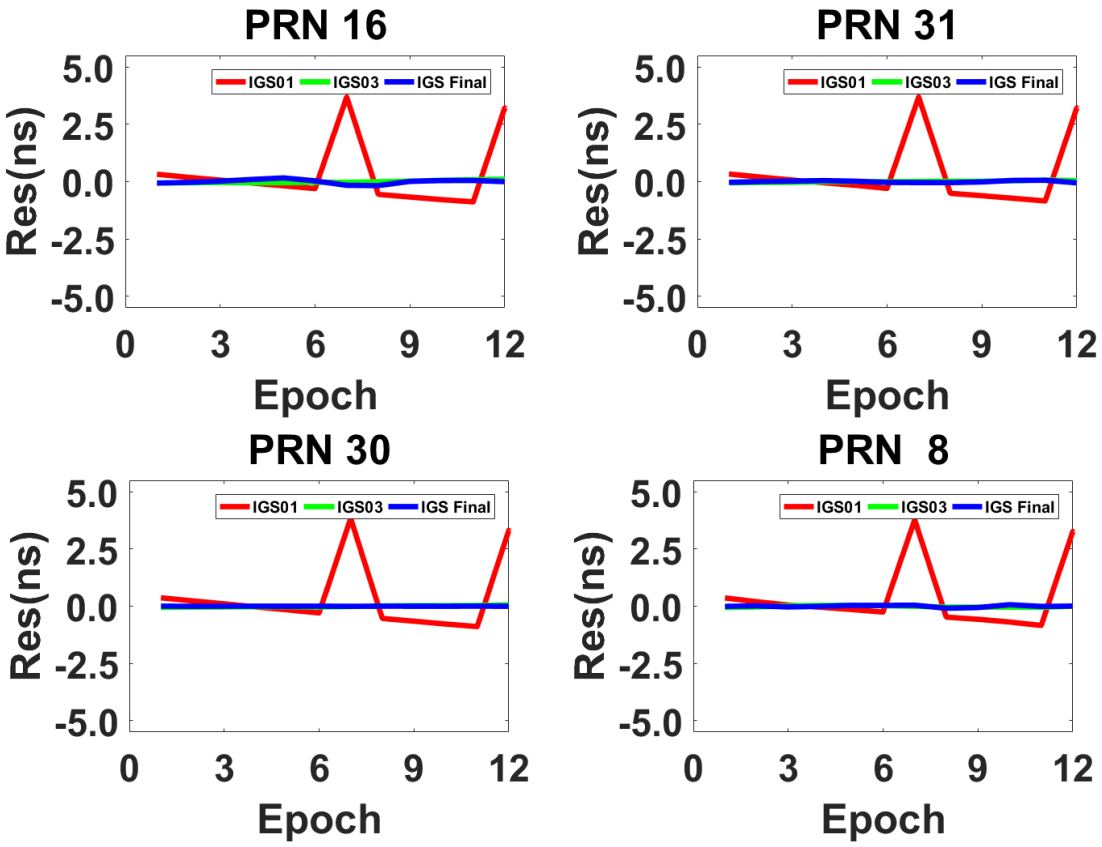

Figure 5-11 Residuals of satellite clocks of PRN 16, PRN 31, PRN 30 and PRN 8 after fitting with the traditional method for IGS01, IGS03 and IGS final products

The proposed method is then applied and the satellite clock drifts are shown in Fig. 5-12. The satellite clock drifts from IGS01, IGS03 and IGS final products with the proposed method are quite similar. Meanwhile, the fitting residuals are shown in Fig. 5-13. The residuals for IGS01 are at the same level with IGS03 and IGS final products. When compared to the traditional method, the residuals for IGS01 are much smaller, which means the internal reliability is better with the proposed method.

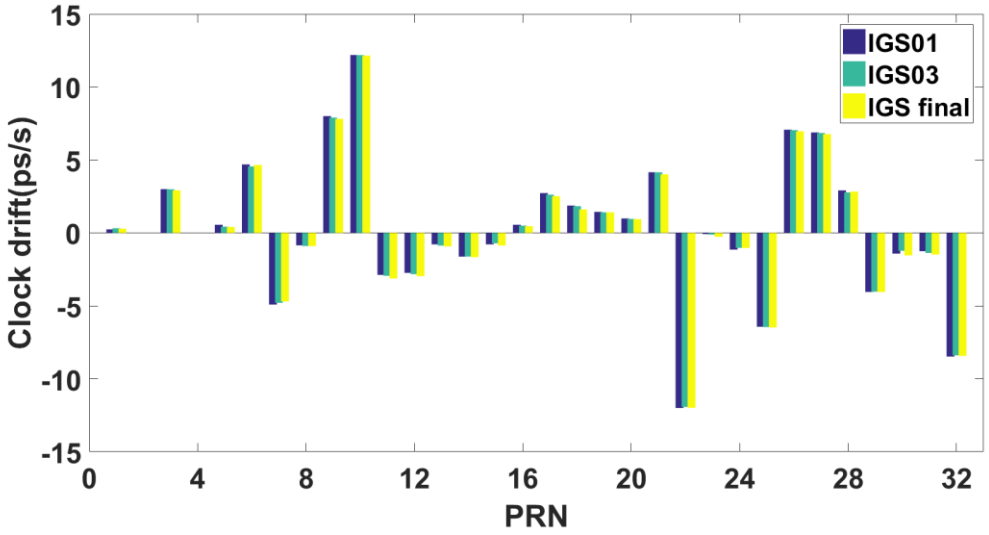

Figure 5-12 Satellite clock drifts obtained with proposed prediction method for IGS01, IGS03 and IGS final products

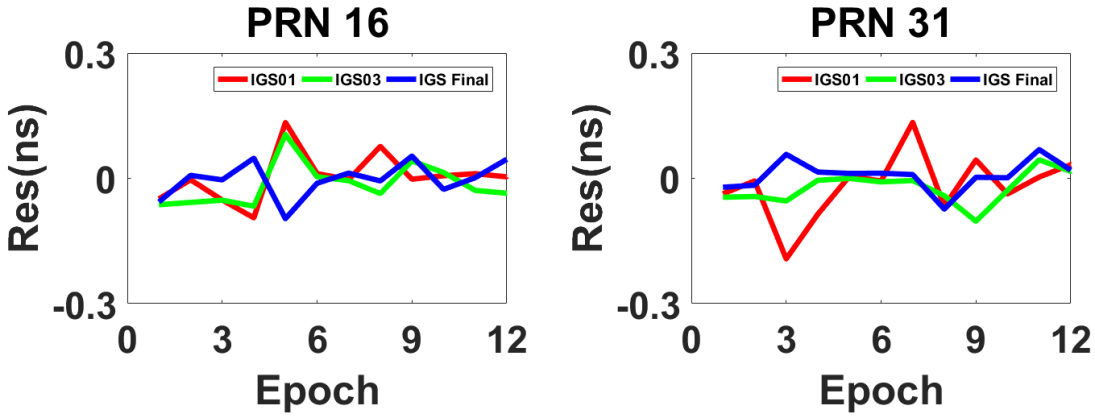

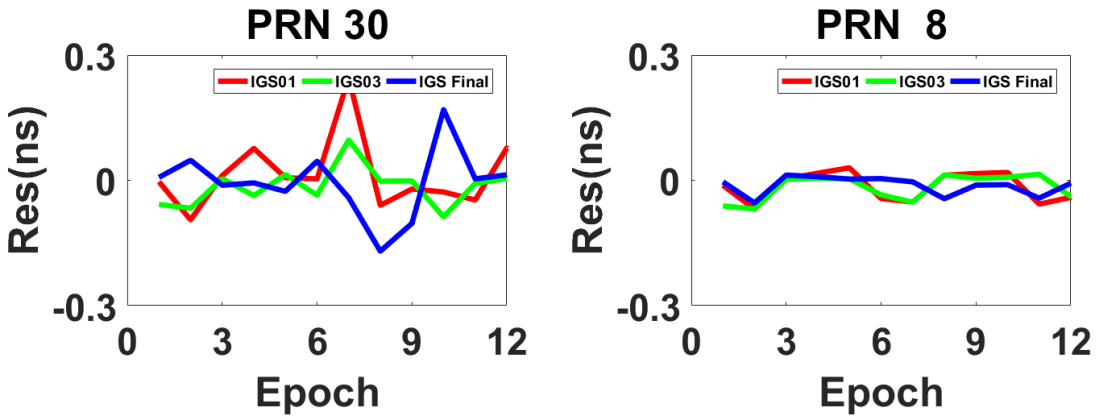

Figure 5-13 Residuals of satellite clocks of PRN 16, PRN 31, PRN 30 and PRN 8 after the new prediction method for IGS01, IGS03 and IGS final products

Apart from the above comparisons, the external reliability is investigated in this section. Both the traditional method and the proposed method are applied for IGS01 and IGS03. The reference is the IGS final clock products and STD of the predicted satellite clock offsets over ten minutes are shown in Fig. 5-14. As we can see, the improvement for IGS01 is obvious for all the satellites. The improvements can be more than 2 ns for satellites such as PRN 5 and PRN 12. The average STD of the traditional method for IGS01 is 1.408 ns while that with the proposed new method is 0.079 ns. When comes to IGS03, the average STD of the traditional method is 0.243 ns and that with the proposed new method is 0.080 ns. Thus, the external reliability of the proposed method is also proved.

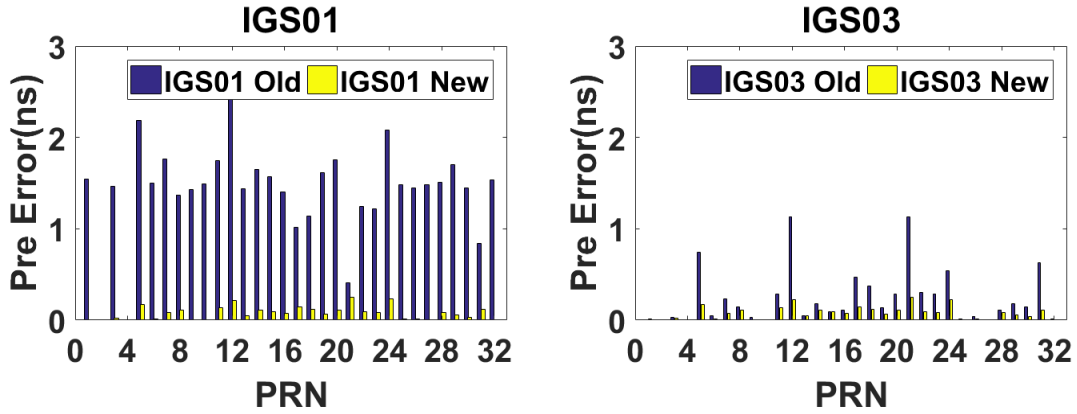

Figure 5-14 Comparison of the proposed (new) and traditional (old) method for satellite clock offset prediction with IGS01 and IGS03 products

5.3 Summary

In this chapter, precise satellite orbit and clock offsets prediction using IP products at the user end are investigated. For precise orbit prediction based on IP, the average orbit prediction RMSE values of the 31 satellites over 12 hours are 0.031 m, 0.032 m, and 0.033 m for the radial, along-track and cross-track directions. With the predicted orbit, the static PPP of 32 globally distributed stations is carried out, and the average RMSE for all stations are 0.012 m, 0.015 m, and 0.021 m for the north, east and vertical directions. For satellite clock offsets prediction, the STD of IIR/Rb, IIR-M/Rb, IIF/Rb and IIF/Cs clocks is 0.17 ns, 0.22 ns, 0.09 ns and 0.90 ns for prediction over 1 hour. For prediction over 6 hours, the STD of IIR/Rb, IIR-M/Rb and IIF/Rb are smaller than 0.4 ns while the STD of IIF/Cs is 2.04 ns. The clock IP with one-hour update rate is compared with IGU products in PPP. The results indicate that average RMS of the kinematic PPP with all stations is 0.360 m for updating IP every hour while the average RMS of the kinematic PPP results utilizing the IGU products is 0.500 m, with improvement as high as 28%. The proposed new method is compared with the traditional method. With 6 minutes of data for

fitting, the average STD of the traditional prediction method for IGS01 is 1.408 ns while that with the proposed new prediction method is 0.079 ns. When comes to IGS03, the average STD of the traditional method is 0.243 ns and that with the proposed new method is 0.080 ns.

CHAPER SIX: PROTOTYPE SYSTEM DEVELOPMENT AND PERFORMANCE ANALYSIS

The prototype of the new real-time PPP system has been developed and is introduced, consisting of server end, user end and some interfaces in Section 6.1. In Section 6.2, the positioning performances are analyzed, focusing on the key features of the new real-time PPP system - scalable update rates and mitigation of communication connection outages.

6.1 System Prototype

A prototype was built for the proposed real-time PPP system. The server for the new real-time PPP system is an ASUS laptop. The processor is an Intel (R) Core (TM) i7-6700HQ CPU @ 2.60GHz. The public Internet protocol address was set as fixed for broadcasting the IP products.

Figure 6-1 Server of the real-time PPP system

The codes at the user end are designed as cross-platform, so they can be executed both in Windows or Linux environments. Normally, the Raspberry PI 3 was used for the test and one

LCD was attached for the display. The following figures shows some scenarios of the user end for the land vehicle tests.

Figure 6-2 Vehicle and antenna for the real-time PPP at user end

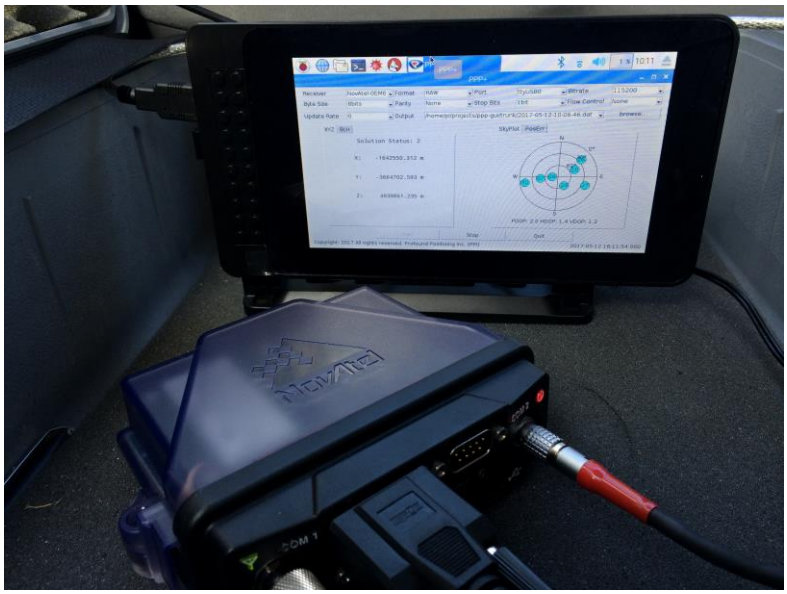

Figure 6-3 Testing units for the real-time PPP at user end

The following GUI is designed and implemented on Raspberry PI 3, which is shown in Fig 6-4

and Fig 6-5. The GUI consists of the configuration for receivers, solutions, update rate settings, DOP, the skyplot, positioning error, output directory, and control buttons.

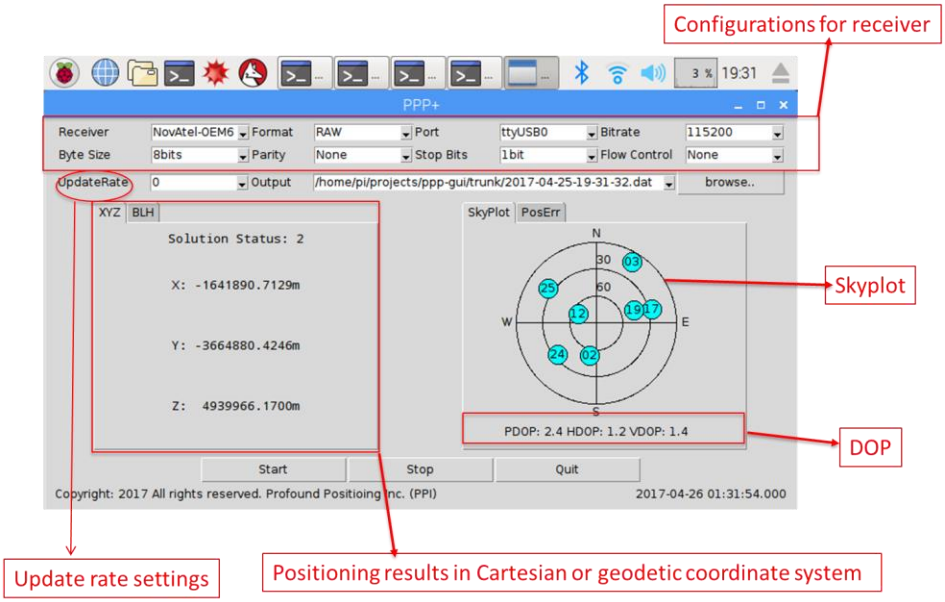

Figure 6-4 The GUI for the real-time PPP user end (1)

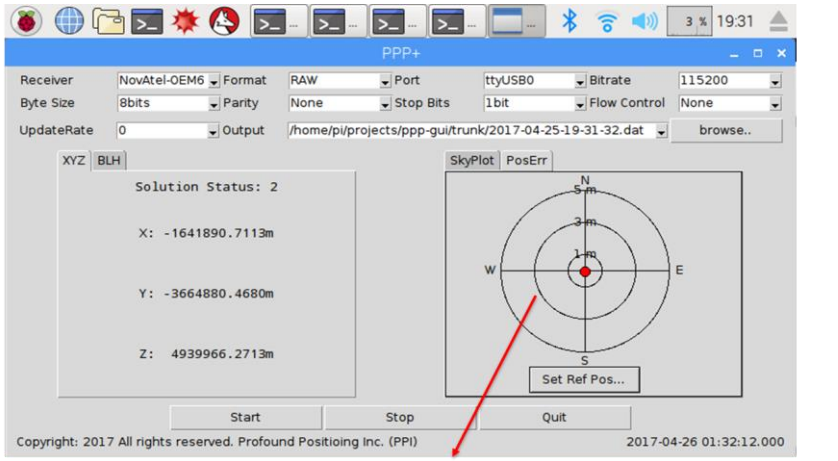

Figure 6-5 The GUI for the real-time PPP user end (2)

IP products can be broadcast to users in different modes as discussed in Section 3.1 and the extended SSR are used for the experiments here. The contents of the current SSR and extended SSR (Yang 2017; Yang et al. 2017a) are shown in Table 6-1 and Table 6-2.

Table 6-1 Contents of current SSR for orbit and clock

RTS parameters	Specific parameters
Satellite orbit	Delta radial, Delta Along track, Delta Cross track Dot Delta radial, Dot Delta Along track, Dot Delta Cross track
Satellite clock	Delta Clock C0, Delta Clock C1, Delta Clock C2

Table 6-2 Contents of extended SSR for orbit and clock

RTS parameters	Specific parameters
Satellite orbit	Delta radial, Delta Along track, Delta Cross track Dot Delta radial, Dot Delta Along track, Dot Delta Cross track Satellite SRP parameters for each satellite
Satellite clock	Delta Clock C0, Delta Clock C1, Delta Clock C2 Periodic coefficients for each satellite

For the satellite clock, the extended part is the periodic terms and the effects have been discussed in Section 4.2.2. With the satellite clock IP, the precise satellite clock offset can be easily calculated by combining the polynomial terms and periodic terms. For the satellite orbit, the extended content is the SRP for each satellite. The first step is to apply the traditional SSR to obtain the precise orbit; then the numerical integrator is carried out based on the orbit and the SRP.

6.2 Positioning Performance Analysis

In this section, positioning results of the new real-time PPP system are analyzed, focusing on the two key features. The first feature is that the new system can operate with IP products at scalable update rates, thus the users can subscribe to the proper update rates according to the accuracy requirements of their applications. The second feature is the ability to mitigate outage, which is not uncommon in real-time applications. Several experiments including static PPP and kinematic PPP tests are carried out to evaluate the new system.

6.2.1 Positioning with IP products of scalable update rates

Convergence time is a crucial element for both kinematic and static PPP. In this section, the outage is assumed to occur at the very beginning of positioning and different sets are listed in Table 6-3. Taking Set 1 as an example, the update rate is 5 minutes. In this case, the extended SSR package is received at the first second so that the remaining 4 minutes and 59 seconds can be considered as outage period. The extended SSR package will be received again for one epoch followed by outage of 4 minutes and 59 seconds. This process will repeat during the whole positioning process in Set 1.

Table 6-3 Settings for simulated outages with different length

Set 1	The extended SSR package is updated once for 5 minutes, static PPP
Set 2	The extended SSR package is updated once for 10 minutes, static PPP
Set 3	The extended SSR package is updated once for 15 minutes, static PPP

Table 6-4 Filter settings for the RTPPP

	Settings
Constellation	GPS satellites
Combination mode	Ionosphere-free phase and code combinations
Signal selection	GPS L1/ L2
Sampling rate	1s
Elevation mask	7°
Observation weight	Elevation dependent weight
Troposphere ZHD	GPT model
Troposphere ZWD	Initial model + Estimated (random walk process)
Troposphere mapping function	GMF
Phase wind-up	Corrected
Sagnac effect, relativistic effect	IS-GPS-200
Satellite/receiver phase center correction	Corrected with IGS absolute correction model
Solid tides effect	IERS conventions (Gérard and Luzum 2010)
Receive clock	Estimated, white noise
Station coordinates	Estimated

The observation data from FFMJ of 10th January of 2017 is downloaded from IGS and the settings of the static PPP are listed in Table 6-4. The dual frequency ionosphere free model will be used in this experiment and only the GPS observations are used. The static PPP results for the above three settings are presented in Fig. 6-6. The different update rates of IP affect the convergence of the PPP. For Set 1 with 5 minutes' update rate, the convergence is the fastest. The convergence is much slower when comes to the update rate of 15 minutes.

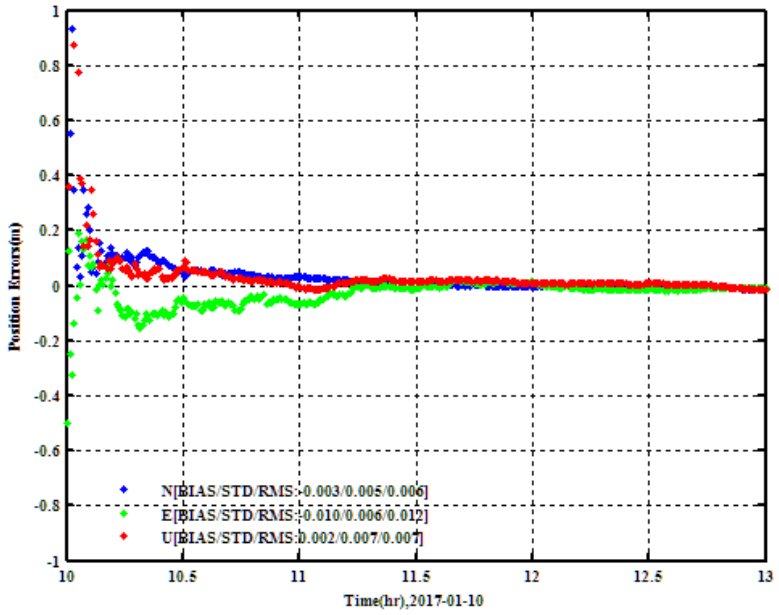

a. Static PPP result for Set 1

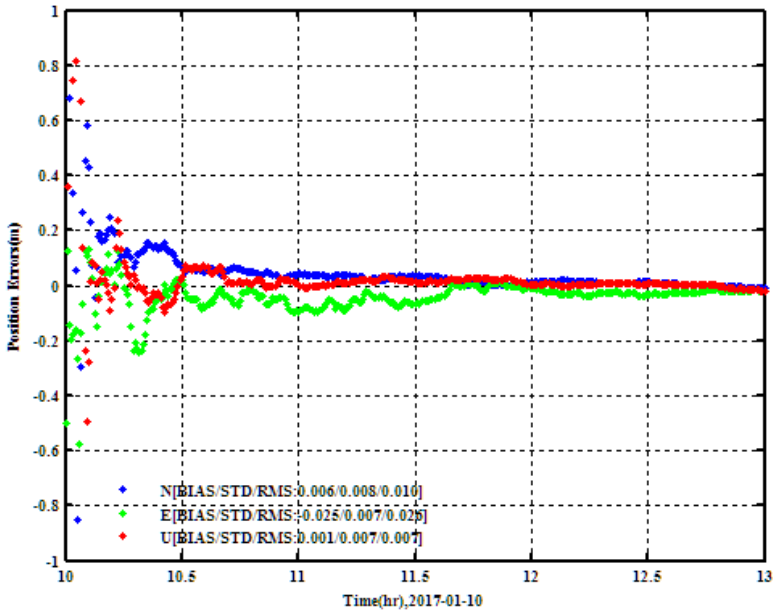

b. Static PPP result for Set 2

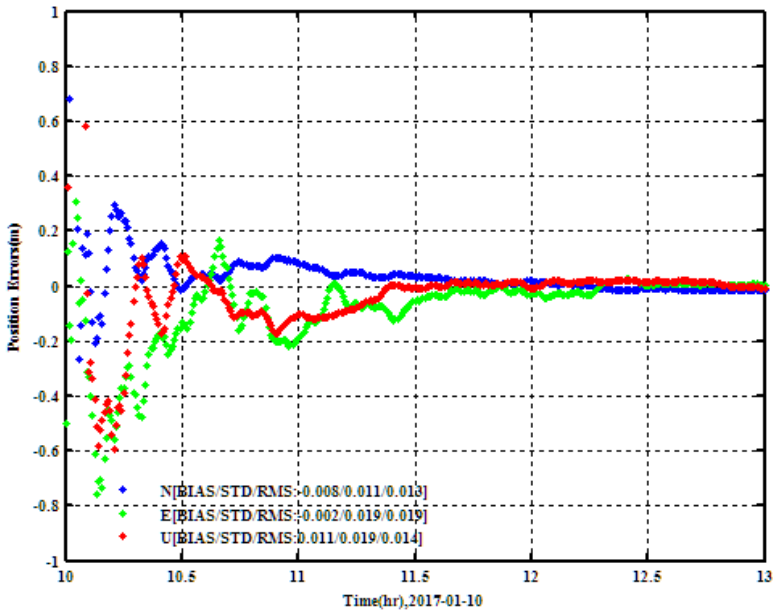

c. Static PPP result for Set 3

Figure 6-6 Static PPP results for above three different settings (a for Set 1, b for Set 2 and c for Set 3)

The statistics after convergence are summarized in Table 6-5. The three-dimension RMS for all three sets is less than 3 cm. With the IP connected once in five minutes, the RMS of Set 1 is the smallest and the RMS of the north, east and vertical direction reach 0.006 m, 0.012 m and 0.007 m correspondingly. For Set 2 and Set 3, the IP is received once in 10 minutes and 15 minutes respectively, the RMS is little larger than Set 1, but the static PPP RMS is still less than 2 cm in each direction.

Table 6-5 The PPP RMS for above different settings

	RMS of static PPP (m)			
	North	East	Vertical	3-D
Set 1	0.006	0.012	0.007	0.015
Set 2	0.010	0.025	0.007	0.028
Set 3	0.013	0.019	0.014	0.027

To investigate the effects of different IP update rates after convergence, observation data on 18th September of 2017 with 1 Hz from 144 IGS stations are downloaded and applied. The experiment begins with IP at high update rates for four hours to ensure the convergence. Afterwards, IP products with different update rates are applied for the next two hours. The following Fig. 6-9 shows the effects of the update rates on PPP after convergence, starting from 1 minute to 30 minutes. Generally, the positioning RMS degrades with the update rates in north, east and vertical directions. The degradation rate is faster in the first 10 minutes for all three directions. With update rates larger than 10 minutes, the difference becomes smaller. Both the RMS and the degradation rate in the vertical direction are a little larger than the north and east direction. The main reason for this is the coupling of the satellite clock errors and the positioning error in the vertical direction.

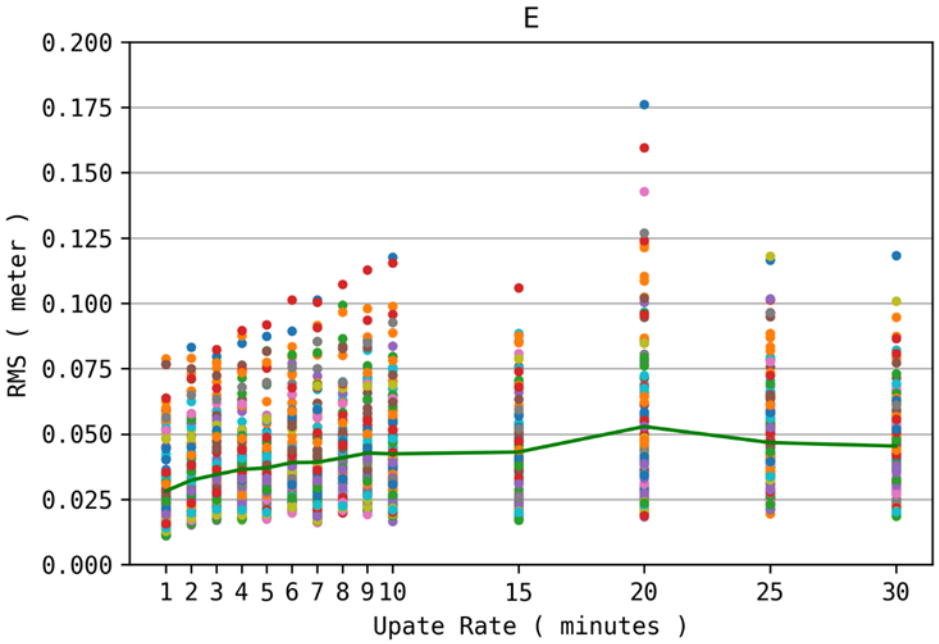
E
0.200
0.175
0.150
0.125
0.100
0.075
0.050
0.025
0.000
RMS (meter)
1 2 3 4 5 6 7 8 9 10 15 20 25 30
Upate Rate (minutes)

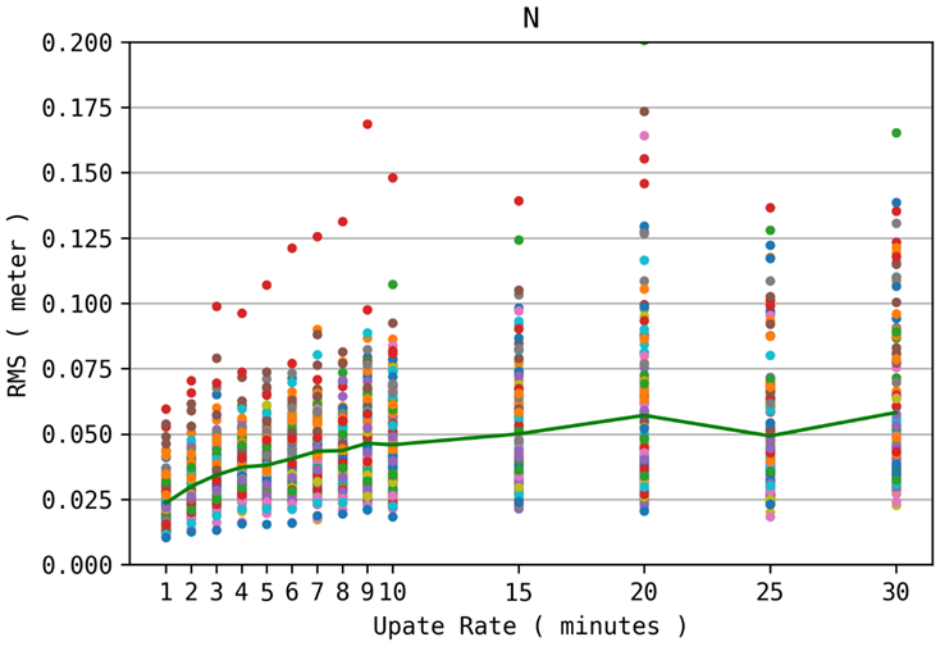
N
0.200
0.175
0.150
0.125
0.100
0.075
0.050
0.025
0.000
RMS (meter)
1 2 3 4 5 6 7 8 9 10 15 20 25 30
Upate Rate (minutes)

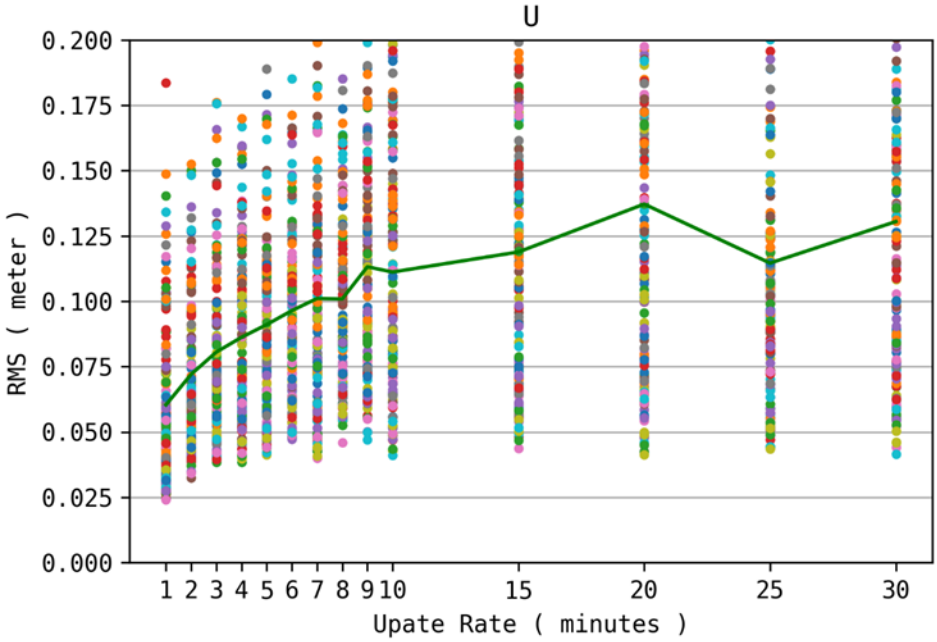

Figure 6-7 The PPP RMS with different IP update rates

Real-time static PPP experiments are carried out. The observations with 1 Hz are real-time received through the Internet from IGS stations such as PRDS (Calgary, Canada) and NRL1 (Washington, America). The external environments of the PRDS and NRL1 stations are shown in Fig. 6-8.

Figure 6-8 The surrounding environments for PRDS (left) and NRL1 (right)

The Raspberry Pi designated as 104 receives in real-time the satellite clock IP products with 10 seconds update rate and orbit IP products with 60 seconds update rate. While the Raspberry Pi designated as 107 is real-time receiving the satellite clock IP products at 1minute update rate and orbit IP products at 6 hours update rate. The PPP experiments are carried out in kinematic mode.

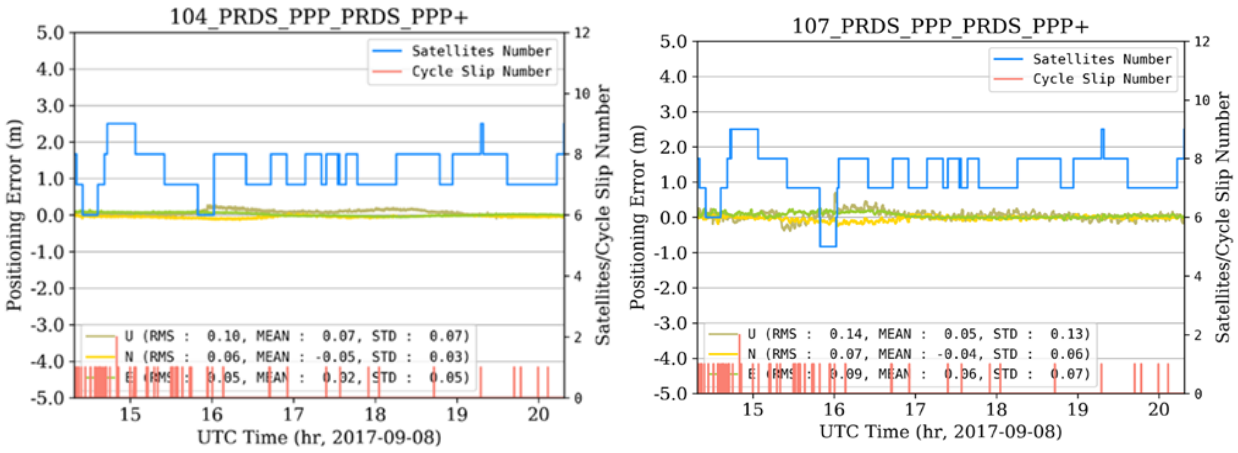

Figure 6-9 New real-time PPP with different update rates on Sep 8th of 2017 for PRDS

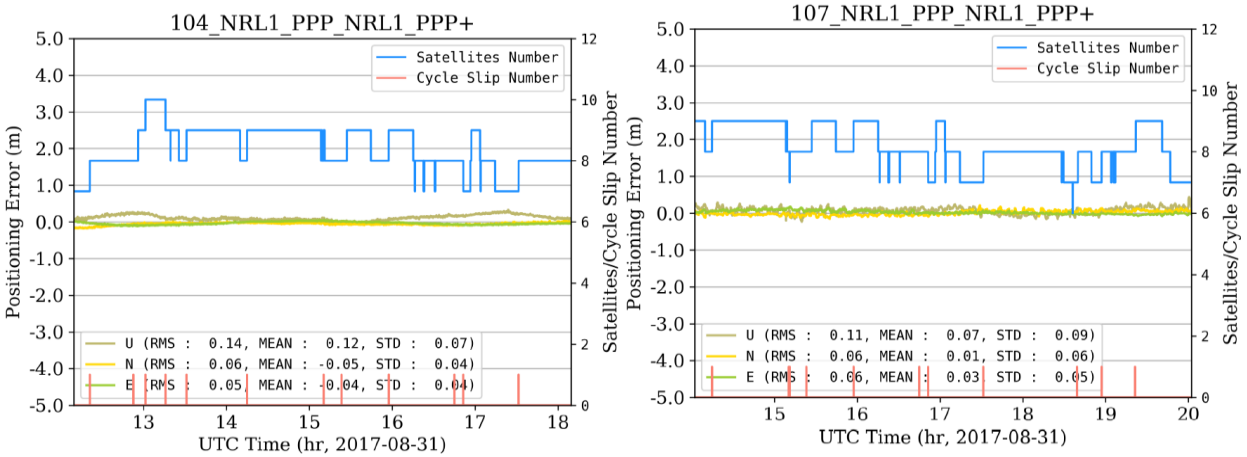

Figure 6-10 New real-time PPP with different update rates on Aug 31st of 2017 for PRDS

As shown in Fig. 6-9 and Fig. 6-10, the real-time PPP system can work with the clock IP updating every 60 seconds and orbit IP updating every 6 hours, and the positioning performances are quite close, with difference at centimeter level, to the one using the high update rates used by

current IGS RTS products. For both PRDS and NRL1, the RMS over 6 hours is centimeter level in the horizontal direction and less than 2 dm in the vertical direction.

For the kinematic PPP, the field test around 70 minutes was carried out in the vicinity of the Children's Hospital in Calgary, Canada. The sample rate for the GNSS observation was 1 second. The IGS station (UCAL) located 3 km away from the rover was used as the base station for Real-Time Kinematic (RTK). During the field test, the speed limit for the road section was 40 km/h, and several red lights were experienced at intersections. The following Fig. 6-11 shows the trajectory of the field test for kinematic PPP, in which the red dots represent the PPP solutions, while the blue dash lines denote the RTK results.

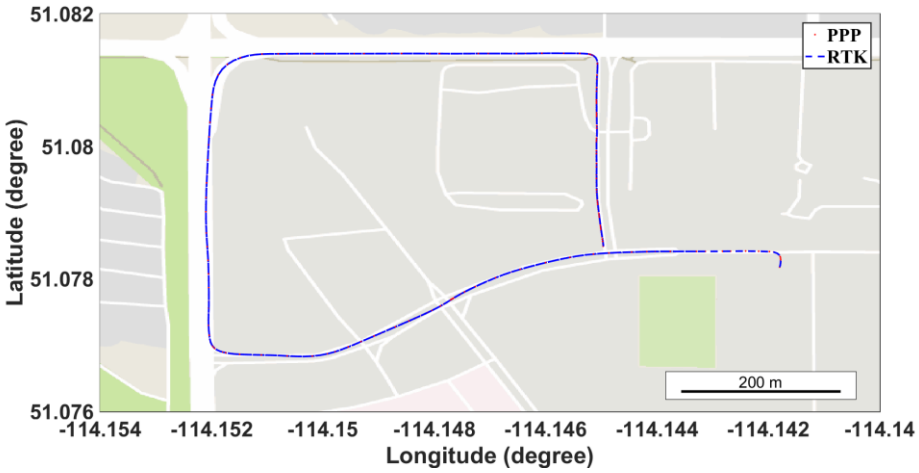

Figure 6-11 Trajectory of the kinematic PPP testing around the Alberta Children's hospital

Two Raspberry Pis are used in this test with IP products at different update rates. For the communication, Raspberry Pi is connected to the hot spot provided by cellphone. The Raspberry Pi designated as 101 is receiving the satellite clock IP products in real-time at 10 seconds update rate and orbit IP products at 60 seconds update rate. While the Raspberry Pi designated as 104 is receiving the satellite clock IP products in real-time at 1minute update rate and orbit IP products

at 6 hours update rate. As we can see that, the RMS in the east, north and vertical directions is quite close from the two different settings. Meanwhile, the convergence time for both settings is similar as well. The RMS of Raspberry Pi designated as 104 are 0.08 m, 0.12 m and 0.14 m in the north, east and vertical directions correspondingly. As we can see that, the new real-time PPP system can operate with scalable updates in kinematic mode as well.

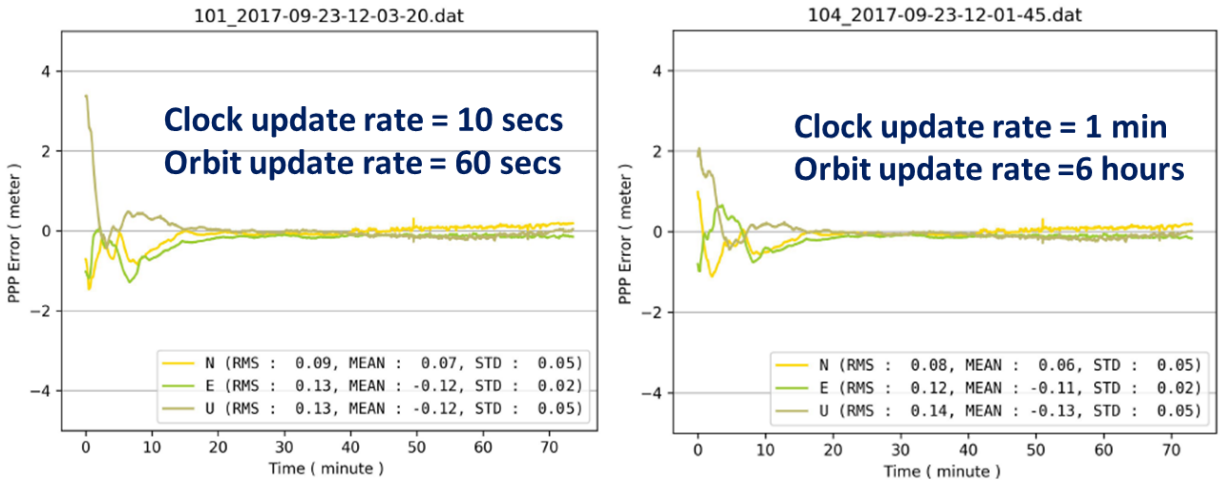

Figure 6-12 Field test of the new real-time PPP system with different IP update rates

6.2.2 Positioning with Outages

In this section, the GPS observation data from 63 globally distributed IGS stations, shown in Fig. 6-13, are received in real-time and stored for the 4th day of GPS week 1920. The data was stored in RINEX with 1 Hz frequency. Meanwhile, the RTS products from stream IGS03 were also received and stored for the 3rd day and 4th day of GPS week 1920. The RTS products of the 3rd day of GPS week 19020 was used to generate the extended SSR parameters. Meanwhile, the IGS final products for the 4th day of GPS week 1920 were downloaded as the reference for evaluation.

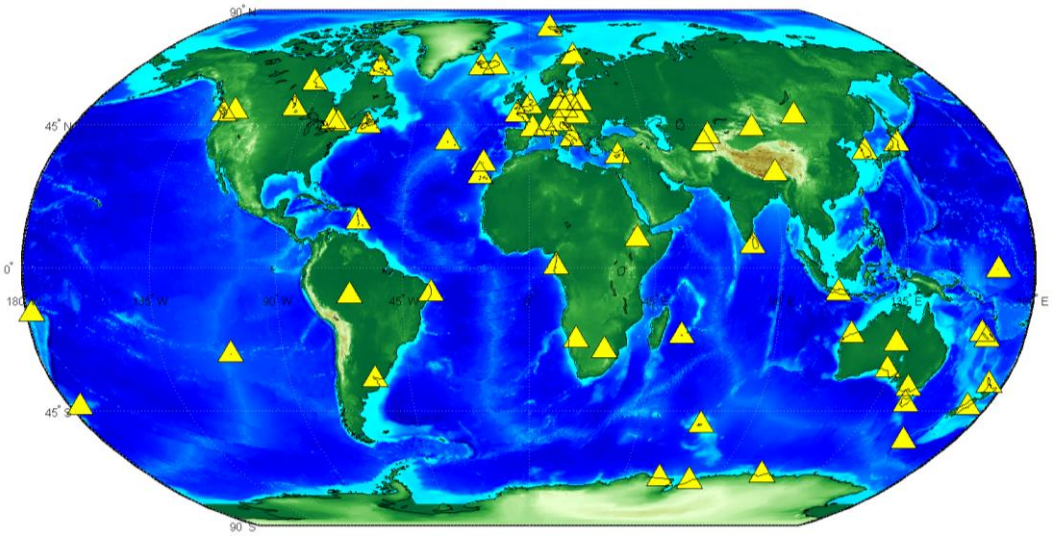

Figure 6-13 Distribution of 63 globally IGS stations selected for the RTPPP experiments

Both the kinematic and static PPP will be carried in the post-mission mode to investigate the performance of the extended SSR package during different situations. The observation data from 63 globally distributed stations will be used to comprehensively analyze positioning performances.

Convergence time is a crucial element for both kinematic and static PPP. In order to analyze the performance of the extended SSR package better, the outage will be assumed at different periods, such as 12 hours, half hour and 0 hour after convergence, as listed in the following table.

Table 6-6 Settings for simulated outages happened at different time

Set 1	Outage happens after 12 hours of positioning
Set 2	Outage happens after 0.5 hours of positioning
Set 3	Outage happens at the beginning of positioning

RMS in horizontal and vertical directions is shown separately in the following experiments to analyze the positioning results in-depth. The positioning RMS for the next 2 hours after the outage is divided into four periods - 0 to 30 minutes, 30 to 60 minutes, 60 to 90 minutes and 90 to 120 minutes - to investigate the variation of positioning precision over time.

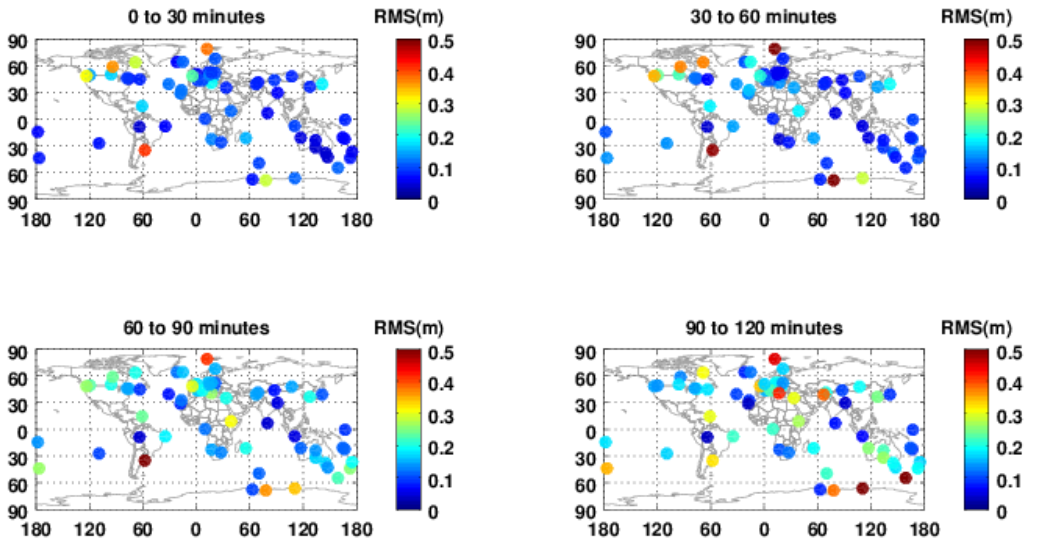

Figure 6-14 Horizontal RMS of kinematic PPP for 0 to 30 minutes, 30 to 60 minutes, 60 to 90 minutes and 90 to 120 minutes for Set 1

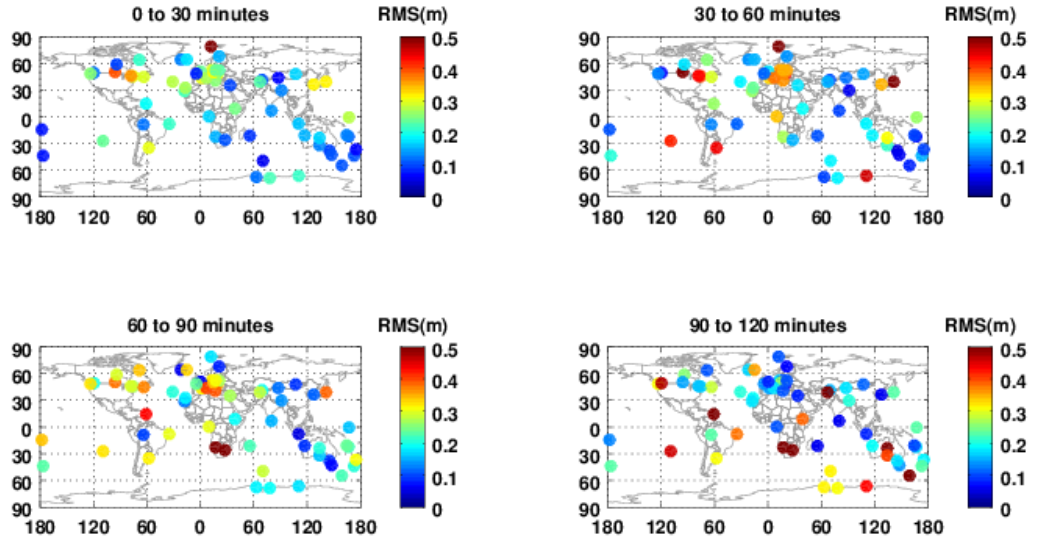

Figure 6-15 Vertical RMS of kinematic PPP for 0 to 30 minutes, 30 to 60 minutes, 60 to 90 minutes and 90 to 120 minutes for Set 1

As we can from Fig. 6-14, with 12-hours convergence before the outage, the horizontal RMS for most stations is better than 0.2 m for the first hour after the outage. As stations with various

locations have different geometry, the positioning results are different over the globally distributed stations. The RMS degrades slowly for the first two hours, for most stations, RMS is better than 0.35 m for 90 to 120 minutes after the outage, some even are still less than 0.15 m in that period. For the vertical RMS shown in Fig. 6-15, the vertical precision is little worse than the horizontal direction. During the first half hour, the vertical RMS for most stations is better than 0.3 m. For 90 to 120 minutes after the outage, the vertical RMS for most stations is better than 0.4 m.

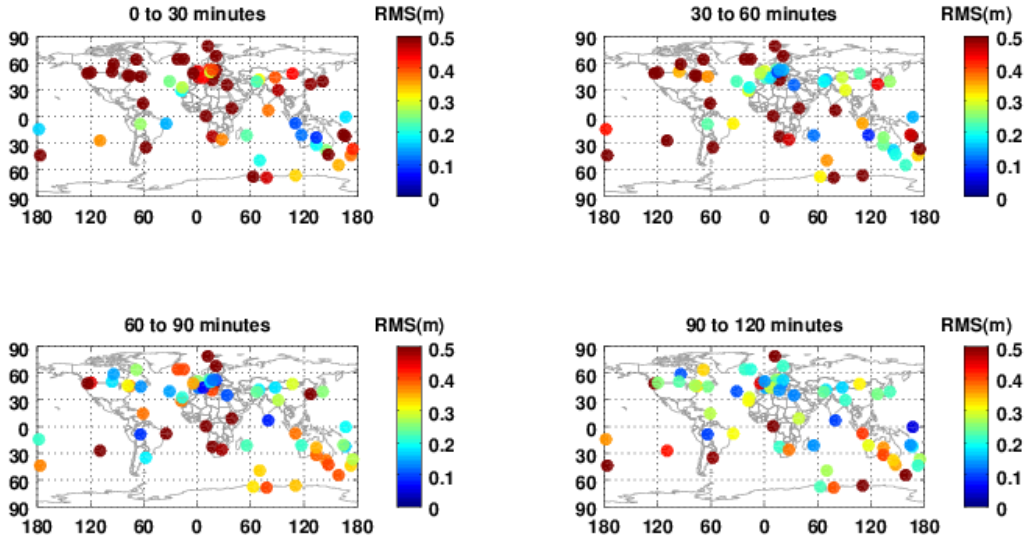

Figure 6-16 Horizontal RMS of kinematic PPP for 0 to 30 minutes, 30 to 60 minutes, 60 to 90 minutes and 90 to 120 minutes for Set 2

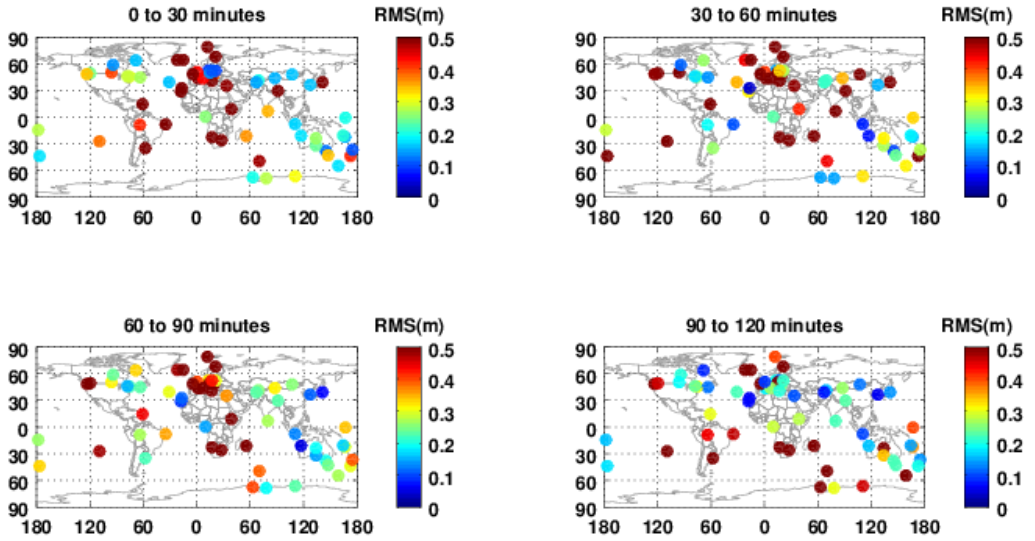

Figure 6-17 Vertical RMS of kinematic PPP for 0 to 30 minutes, 30 to 60 minutes, 60 to 90 minutes and 90 to 120 minutes for Set 2

For Fig. 6-16 and Fig. 6-17 just half an hour before the outage, not all stations have fully converged solutions. During the first half hour after the outage, the horizontal RMS can be more than 0.5 m for some stations. In this situation, two processes are interfering with each other; one process is the convergence for the PPP, and the other is the degradation of the satellite products. Most stations see more accurate positioning results during the 60 to 90 minutes and 90 to 120 minutes than in the first hour after the outage.

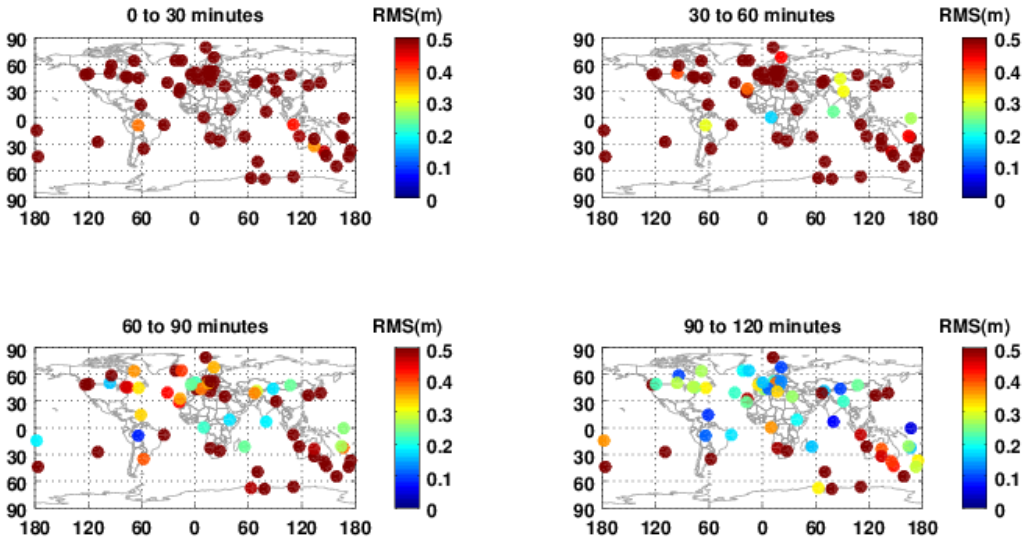

Figure 6-18 Horizontal RMS of kinematic PPP for 0 to 30 minutes, 30 to 60 minutes, 60 to 90 minutes and 90 to 120 minutes for Set 3

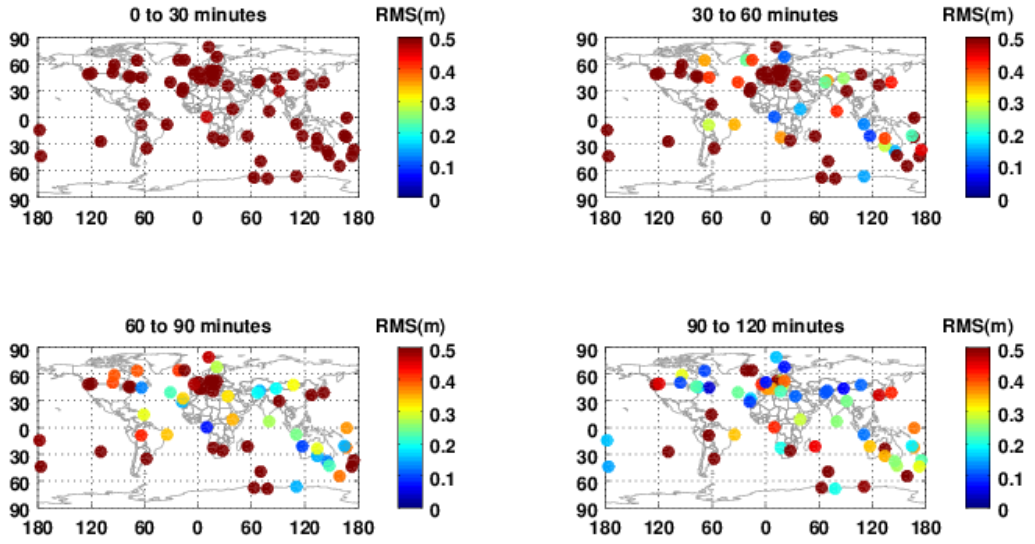

Figure 6-19 Vertical RMS of kinematic PPP for 0 to 30 minutes, 30 to 60 minutes, 60 to 90 minutes and 90 to 120 minutes for Set 3

Figures 6-18 and 6-19 show the outage occurring at the very beginning, so all the stations are during the convergence period for the first half hour. The positioning accuracy improves with longer converge time. Some stations can reach 0.1 m for both the horizontal and vertical

direction 90 minutes after the outage. The details of the positioning errors are summarized in Table 6-7.

Table 6-7 Kinematic RTPPP results of 2 hours after the outage for different settings

		Horizontal RMS (m)				Vertical RMS (m)			
		0-30 min	30-60 min	60-90 min	90-120 min	0-30 min	30-60 min	60-90 min	90-120 min
Set 1	Max	0.409	0.738	0.536	0.555	0.565	0.782	0.728	0.749
	Min	0.036	0.039	0.036	0.029	0.058	0.050	0.050	0.053
	Mean	0.117	0.144	0.169	0.198	0.196	0.238	0.249	0.238
Set 2	Max	1.206	2.659	1.034	0.918	1.000	1.424	1.516	0.814
	Min	0.086	0.081	0.066	0.047	0.089	0.037	0.047	0.054
	Mean	0.517	0.475	0.336	0.295	0.365	0.425	0.434	0.319
Set 3	Max	2.015	4.313	3.650	1.697	3.065	2.456	2.949	1.830
	Min	0.367	0.170	0.079	0.050	0.472	0.084	0.073	0.041
	Mean	1.105	0.942	0.576	0.368	1.202	0.781	0.574	0.380

As we can see that the outage will have much less effect when the filter is fully converged, the average horizontal RMS of the first set is 0.117 m, 0.144 m, 0.169 m and 0.198 m for 0 to 30 minutes, 30 to 60 minutes, 60 to 90 minutes and 90 to 120 minutes correspondingly. The vertical RMS is a little worse than the horizontal, which can also reach 0.196 m, 0.238 m, 0.249 m and 0.238 m for those four different periods. The main trend of the RMS over the following two hours after the outage is the slow degradation for Set 1. While for Set 2 and Set 3, the positioning accuracy is not that good as Set 1 because most stations experience the outage during the convergence period. There are two main trends for both Set 2 and Set 3; one is the convergence of the positioning; the other is the degradation of the satellite products. And we can tell from the comparison form that convergence is the main trend. For Set 2, the average horizontal RMS reduces from 0.517 m to 0.295 m and the average vertical RMS improves from 0.365 m to 0.319

m. For Set 3, obvious convergence trend is shown. The average horizontal RMS improves from 1.105 m to 0.368 m and the average vertical RMS improves from 1.202 m to 0.380 m.

For this section, the same three settings are listed and the RTPPP will be carried out in static mode. The positioning results are demonstrated in horizontal and vertical directions .

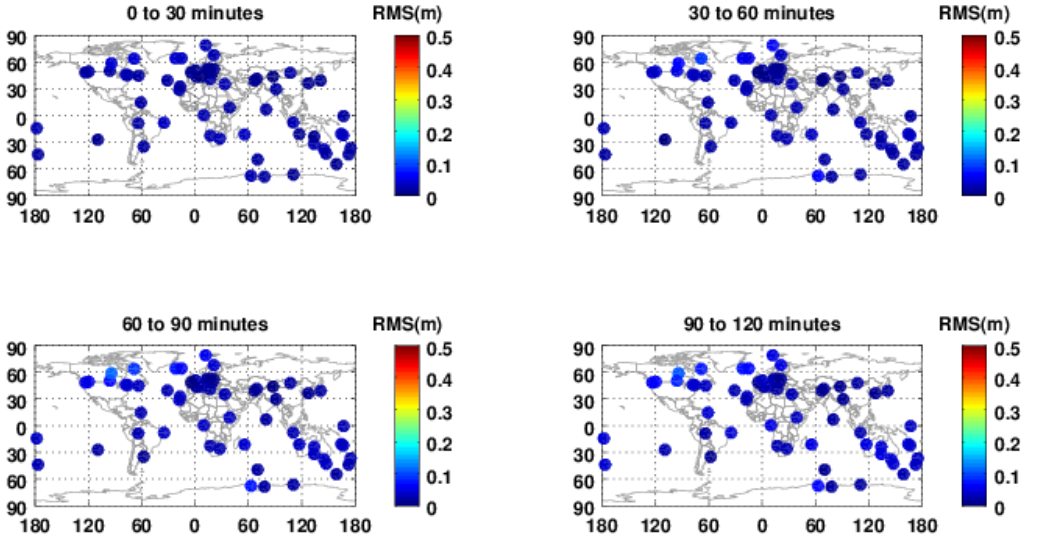

Figure 6-20 Horizontal RMS of static PPP for 0 to 30 minutes, 30 to 60 minutes, 60 to 90 minutes and 90 to 120 minutes for Set 1

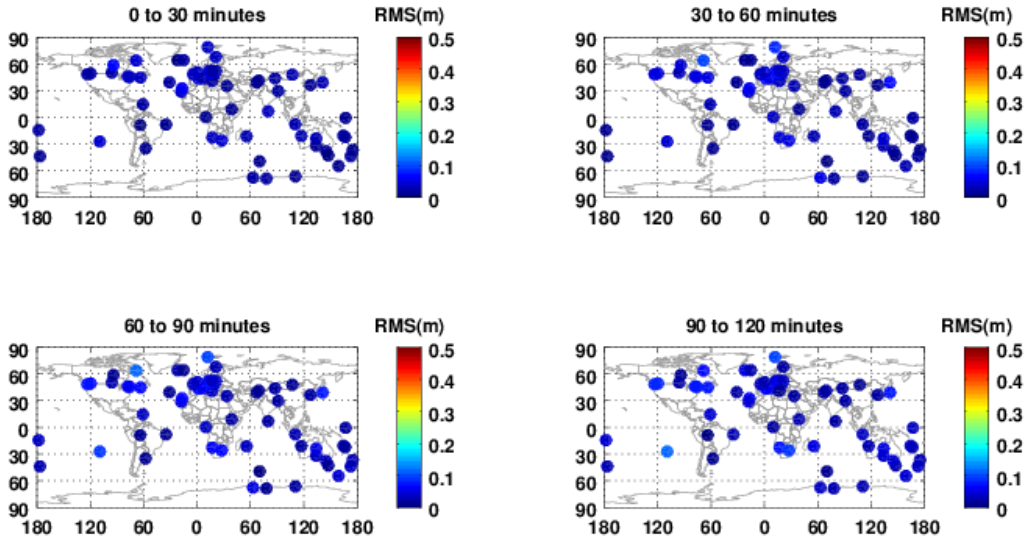

Figure 6-21 Vertical RMS of static PPP for 0 to 30 minutes, 30 to 60 minutes, 60 to 90 minutes and 90 to 120 minutes for Set 1

As shown in Fig. 6-20 and Fig. 6-21, with 12 hours convergence time for static RTPPP, the horizontal and vertical RMS for most stations remains under 0.1 m for two hours after the outage. The satellite products degrade very little over the next two hours, so the positioning results are not obviously affected. The difference between the horizontal and vertical RMS is very small in this set.

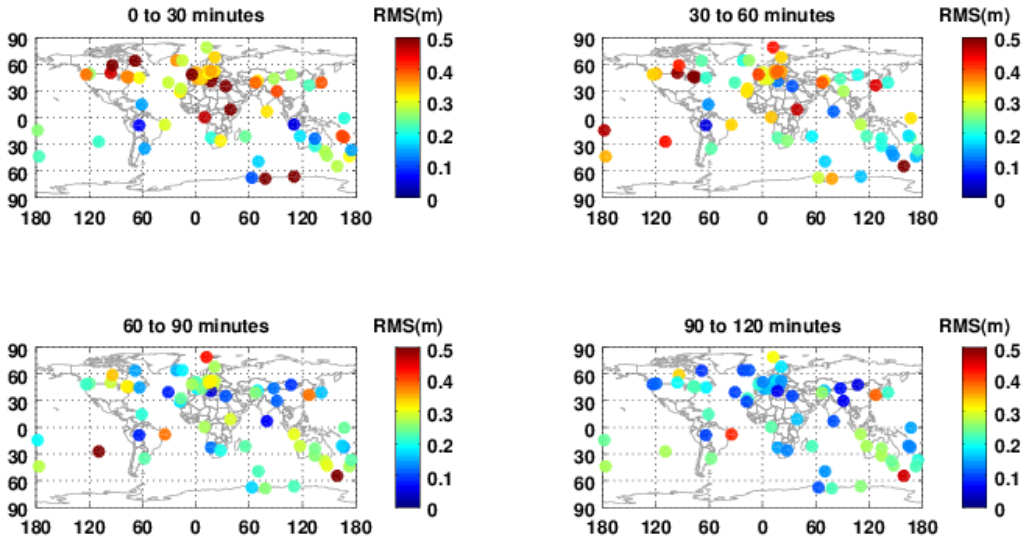

Figure 6-22 Horizontal RMS of static PPP for 0 to 30 minutes, 30 to 60 minutes, 60 to 90 minutes and 90 to 120 minutes for Set 2

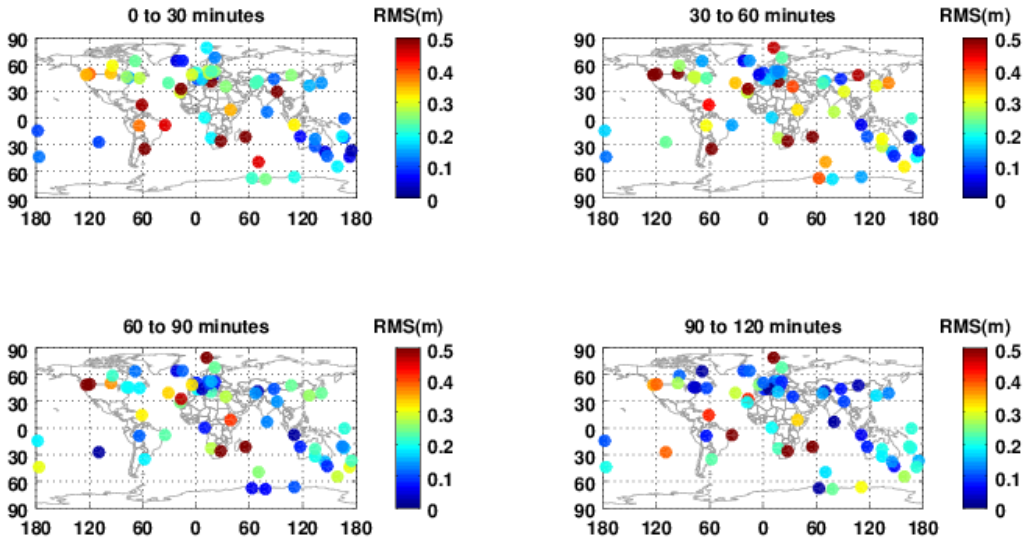

Figure 6-23 Vertical RMS of static PPP for 0 to 30 minutes, 30 to 60 minutes, 60 to 90 minutes and 90 to 120 minutes for Set 2

With half hour convergence before the outage, the horizontal and vertical RMS is shown in Fig. 6-22 and Fig. 6-23. Convergence is the main trend for both horizontal and vertical, even though the positioning accuracy of some stations also reflects the degradation of the satellite products. The RMS of horizontal and vertical directions can reach 0.25 m for most stations and the difference between the horizontal and vertical direction is not obvious in this case.

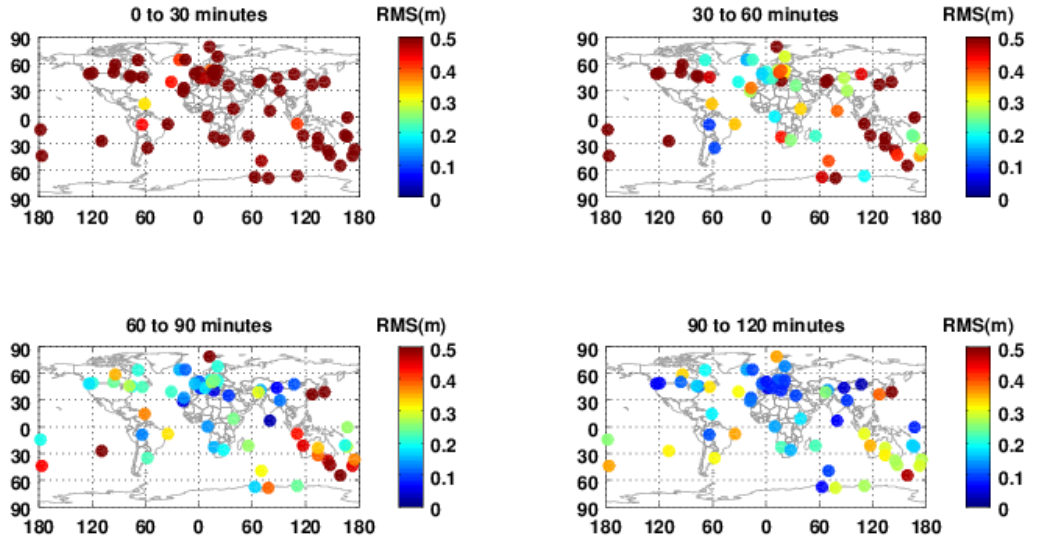

Figure 6-24 Horizontal RMS of static PPP for 0 to 30 minutes, 30 to 60 minutes, 60 to 90 minutes and 90 to 120 minutes for Set 3

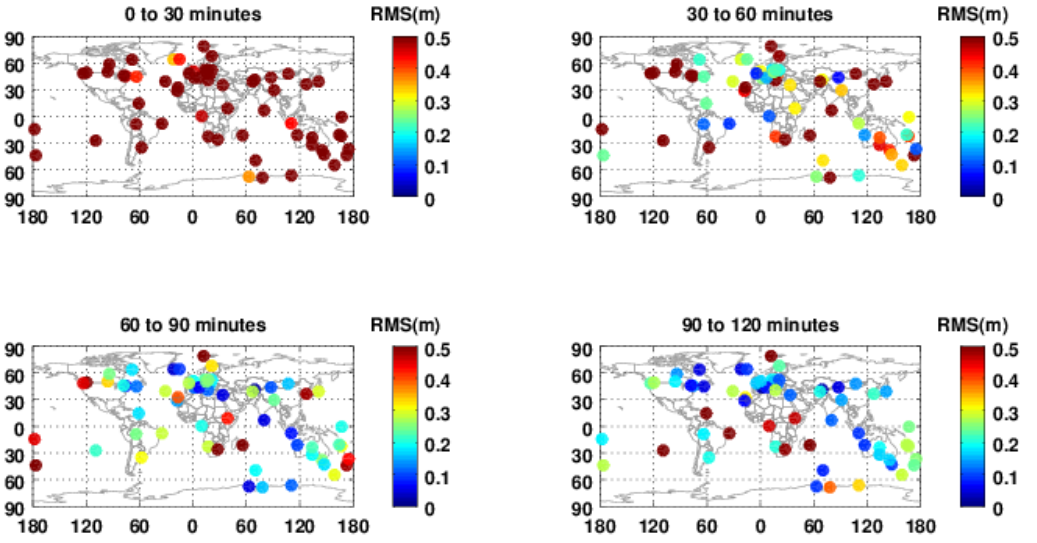

Figure 6-25 Vertical RMS of static PPP for 0 to 30 minutes, 30 to 60 minutes, 60 to 90 minutes and 90 to 120 minutes for Set 3

Figure 6-24 and Fig. 6-25 show the outage happens at the very beginning of the positioning. For most stations, positioning accuracy is beyond 0.5 m for the first half hour due to the pseudo-

range observations. With almost 2 hours of convergence, the horizontal and vertical RMS can reach 0.3 m and 0.4 m correspondingly for most stations.

Table 6-8 Static RTPPP results of 2 hours after the outage for different settings

		IP Horizontal (m)				IP Vertical (m)			
		0-30 min	30-60 min	60-90 min	90-120 min	0-30 min	30-60 min	60-90 min	90-120 min
Set 1	Max	0.041	0.084	0.108	0.107	0.061	0.094	0.112	0.110
	Min	0.003	0.002	0.002	0.004	0.002	0.003	0.002	0.003
	Mean	0.017	0.023	0.028	0.032	0.020	0.028	0.034	0.037
Set 2	Max	1.147	0.655	0.566	0.460	0.912	0.779	0.656	0.640
	Min	0.045	0.051	0.040	0.045	0.027	0.035	0.014	0.008
	Mean	0.336	0.293	0.235	0.187	0.252	0.275	0.209	0.189
Set 3	Max	2.790	2.026	1.295	0.641	3.152	1.424	1.132	0.818
	Min	0.323	0.085	0.022	0.027	0.343	0.060	0.015	0.015
	Mean	0.900	0.501	0.271	0.192	1.048	0.459	0.253	0.221

Statistics of positioning accuracy are summarized in the Table 6-8. For Set 1 with the 12-hours length of convergence, the static RTPPP results with the extended SSR package are slightly affected by the outage. The average horizontal RMS are 0.017 m, 0.023 m, 0.028 m and 0.032 m correspondingly for period of 0-30 minutes, 30 to 60 minutes, 60 to 90 minutes and 90 minutes to 120 minutes. Meanwhile, the positioning results in the vertical direction have similar accuracy, which are 0.020 m, 0.028 m, 0.034 m and 0.037m for those four periods. The positioning results see a very slow degradation cause of the degradation of the predicted satellite orbit and clock. For Set 2 and Set 3, we can see the obvious convergence trend for both the horizontal and vertical direction. For Set 2, the average horizontal RMS improves from 0.336 m to 0.187 m and the average vertical RMS improves from 0.252 m to 0.189 m. For Set 3, the convergence trend is more obvious, the horizontal and vertical RMS reaching 0.192 m and 0.221 m after convergence. Fig. 6-26 shows the performance of the new real-time PPP system during

the outage, starting from 2 minutes to 30 minutes. The same GNSS data of 144 IGS stations as in the Section 7.2.1 are used here. As we can see, the positioning RMS is degrading with outage length. Degradation is much faster in the vertical direction than the horizontal direction. Meanwhile, the degradation rate is faster in the first several minutes and then slow down. Need to mention, the lines denote the average of different stations, which demonstrate the performance trend of the new real-time PPP system during the outage.

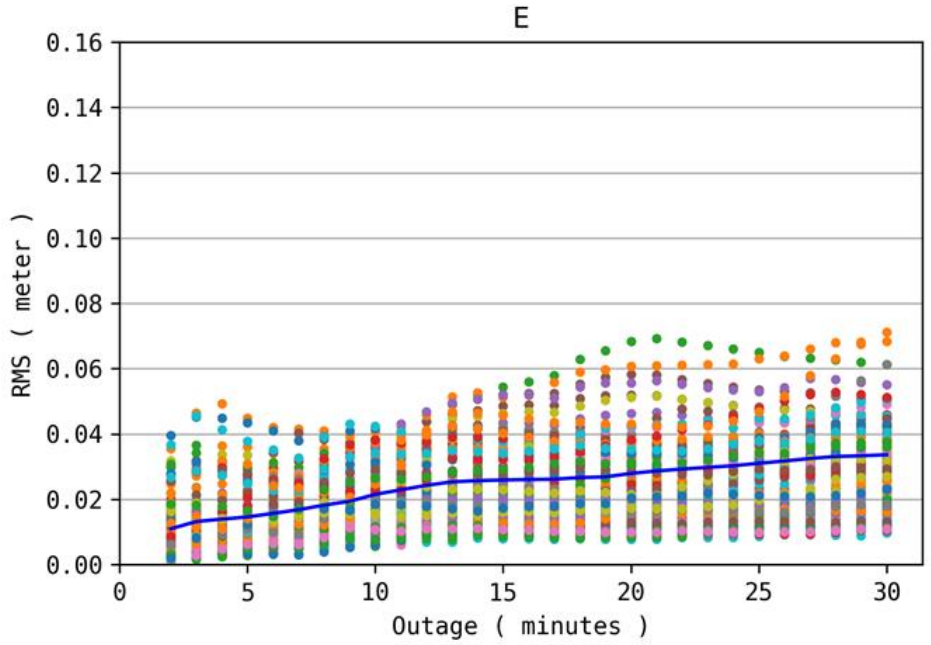

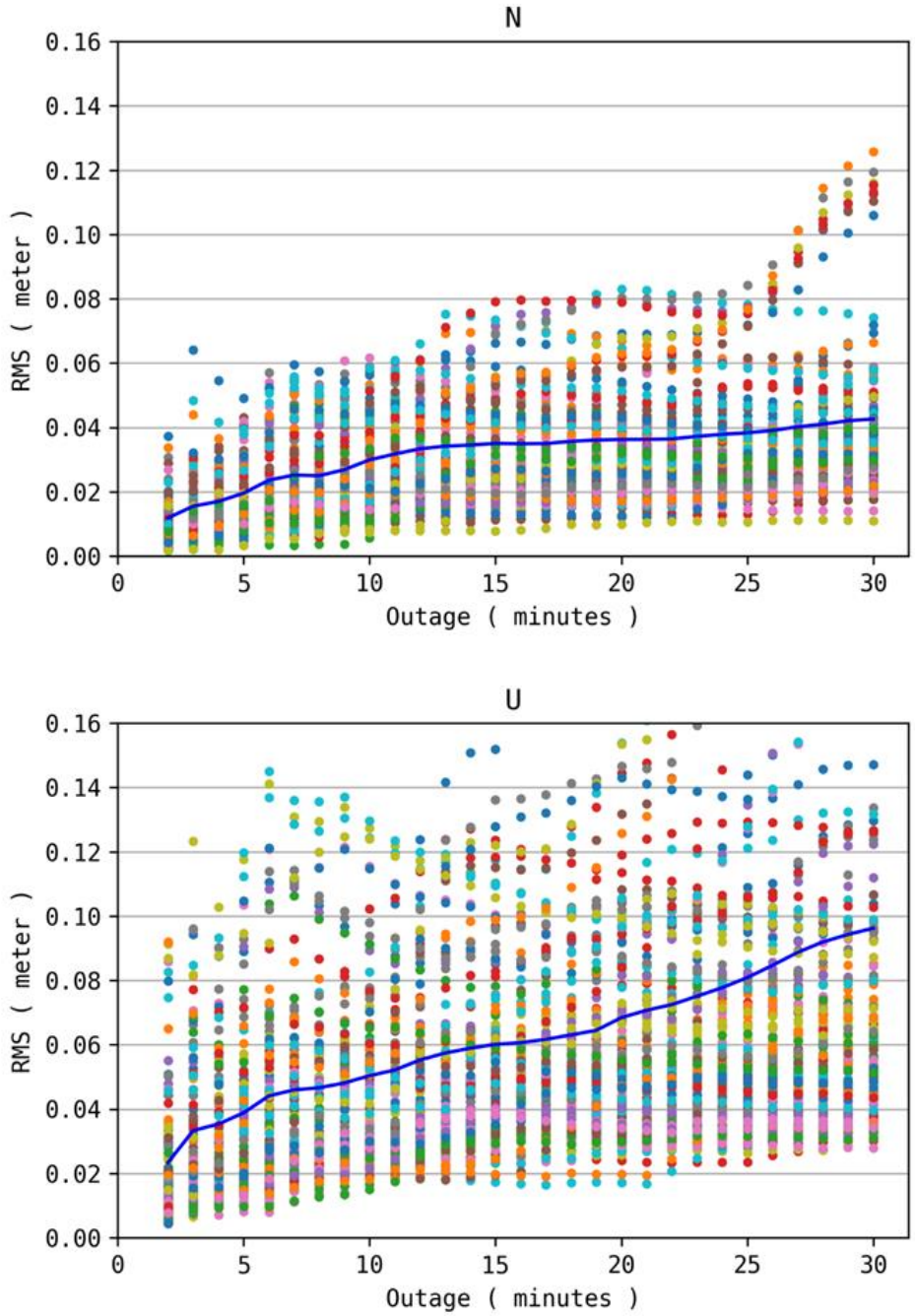

Figure 6-26 The new real-time PPP system with different outage lengths

As mentioned above, the real-time PPP system is tested continuously in real-time. The Raspberry Pi designated as 102 applies the traditional real-time PPP and the one designated as 107 runs the

new real-time PPP system. The PRDS observations are both real-time received from IGS simultaneously. Some snapshots of real-time performances of these two Raspberry Pis are shown as follows.

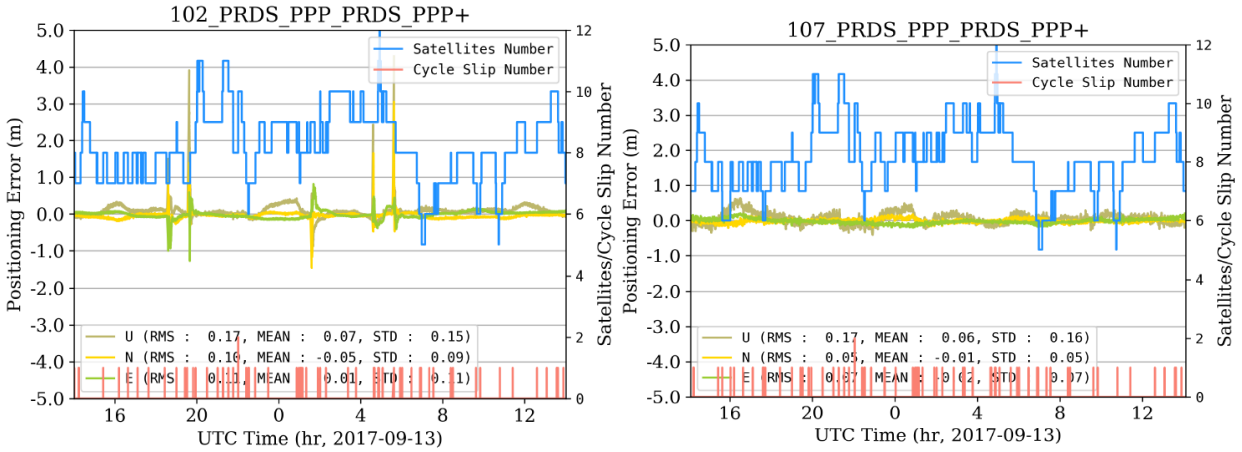

Figure 6-27 Traditional real-time PPP (left) and new real-time PPP (right) with some network outages on Sep 13th of 2017

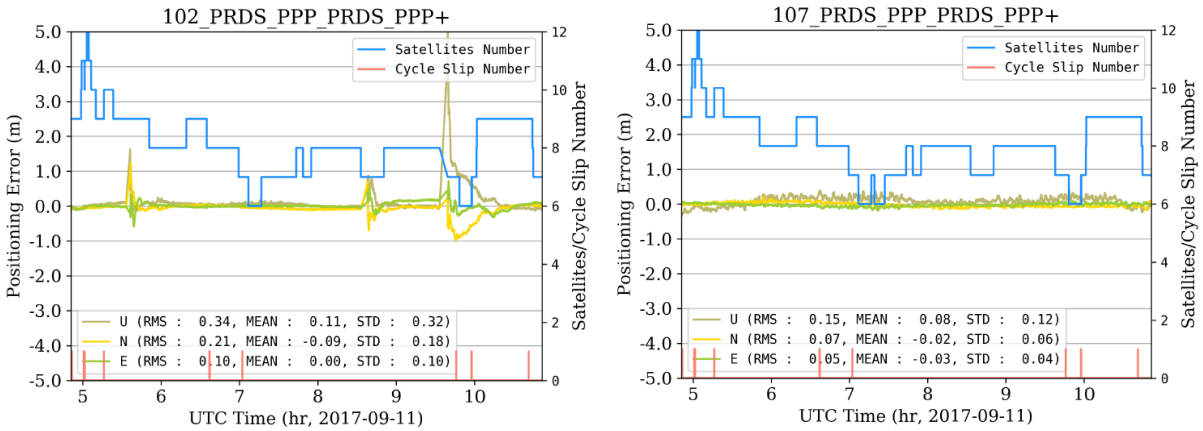

Figure 6-28 Traditional real-time PPP (left) and new real-time PPP (right) with some network outages on Sep 11th of 2017

As we can see, the traditional real-time PPP must re-converge when an outage occurs, while the new real-time PPP system can maintain performance during the same outage. The RMS of Raspberry Pi 107 on Sep 11th of 2017 can be 0.07 m, 0.05 m and 0.15 m in the north, east and

vertical directions. While the RMS of Raspberry Pi 102 reaches 0.21 m, 0.10 m and 0.34 m during the same period. There are three obvious re-convergences.

The vehicle-based land field tests are carried out to furtherly test the new real-time PPP system with outages. The field tests were carried out in the vicinity of Alberta Children's hospital. The sample rate for the GNSS observation was 1 second. The IGS station (UCAL) located 3 km away from the rover was used as the base station for RTK after the test. During the field test, the speed limit for the road section was 40 km/h, and several red lights were experienced at intersections. For each circle around the hospital, it takes about three minutes for driving. The whole test was more than one hour and the just circling around Alberta Children's hospital. The trajectory of the first circle of the test is plotted as Fig. 6-29. The testing environment is open sky and normally seven to ten GPS satellites can be received during the test.

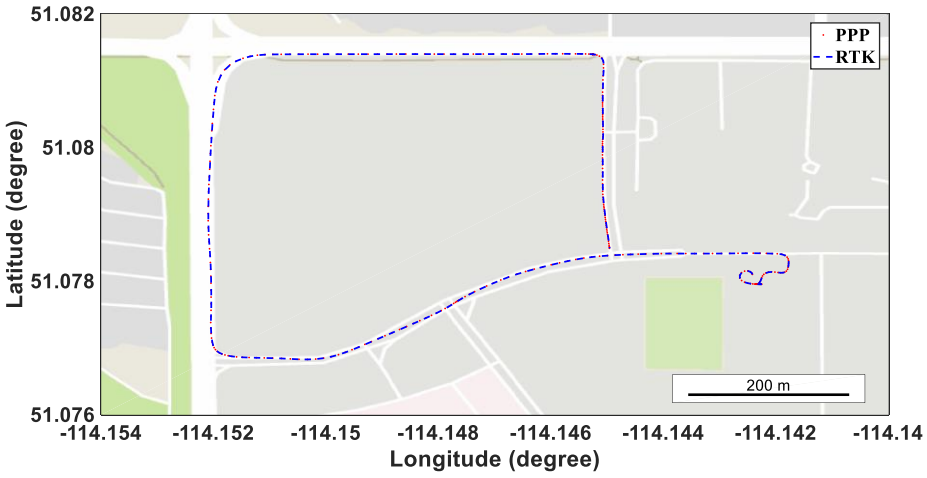

Figure 6-29 Trajectory of the kinematic PPP testing around the Alberta Children's hospital

The Internet access was realized by connecting the hot spot of the cellphone and outages are simulated by cutting off the Internet connection of the cellphone, such as turning into the flight mode. Once the cellphone Internet access is recovered, the wifi module of RPi will connect to

the hot spot automatically. Note here, the server end of the new real-time PPP system is checked in advance before the field test to ensure the success of the test. The kinematic PPP results are shown in following Fig. 6-30 with regard to the RTK reference.

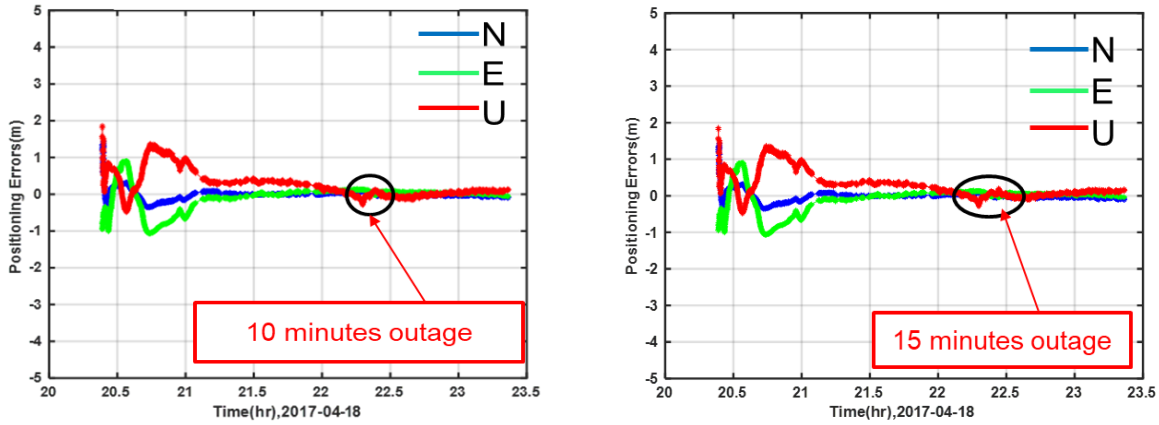

Figure 6-30 Field tests of real-time PPP system with outage for 10 mins and 15 mins

The two Raspberry Pis were started simultaneously manually by the operating the GUI introduced in Section 6.1. For both kinematic PPP results, the convergence is around half hour and the maximum errors in three directions are less than 2 meters for the whole process including the convergence period. For the results on the left, the outage was simulated for 10 minutes starting from 22:15 pm and then the Internet access was recovered, the positioning RMS after convergence was 0.035 m, 0.066 m and 0.159 m in the north, east and vertical directions. We can see that the positioning errors are slightly different from the epochs without outages. The accuracy degradation stands out in vertical direction due to the coupling of satellite clock error and positioning error in vertical direction. For the results on the right, the outage was simulated for 15 mins starting from 22:15 pm, the RMS is slighter larger at 0.041 m, 0.065 m and 0.162 m in the north, east and vertical directions. We can see that, two results are quite the same before

the outage happens, and slightly different during the outage periods, afterwards, becomes quite similar when regular IP products are received again. The main reason for the differences during the outage period is the satellite clock prediction with different length based on IP clock products. As the degradation rate of the clock prediction becomes slower after several minutes, so the difference of 10 mins and 15 mins outage in position domain is quite small. When comes to the RMS over several minutes after convergence, the difference between left and right results becomes even smaller at several milometers due to the effects of the high precision results without outages. In this kinematic experiment, the new real-time PPP system are able to continue when outage happens and can still obtain reasonable positioning results with outages lasting for 10 mins and 15 mins in the kinematic mode, which proves to be a robust and reliable positioning system.

6.3 Summary

In this chapter, the system prototype is first introduced in terms of server end, used end and communication end. Afterwards, the positioning performances are analyzed focusing on scalable update rates and outage mitigation.

The new real-time PPP system can operate with scalable IP update rates and the results indicate the positioning results degrades with the increase of the update rates. For different update rates of 144 IGS stations, the RMS in the vertical direction degrades faster than those of the east and north direction. Meanwhile, the degradation rate in all three directions is much larger in the first ten minutes. Additionally, the update rates will directly affect the convergence of the PPP. The real-time static and kinematic field test show that the positioning performances of the new real-

time PPP system with clock IP updated every 60 seconds and orbit IP updated every 6 hours are similar to that of clock IP updated every 10 seconds and orbit IP updated every 60 seconds.

Both kinematic and static RTPPP are carried out and outages are assumed at different epochs. The results of the RTPPP indicate the outage has less effect on positioning accuracy when the position has converged. In that case, the positioning results will degrade slowly with time. For kinematic RTPPP, the average horizontal RMS changes from 0.117 m to 0.198 m while the vertical RMS degrades from 0.196 m to 0.238 m. The average horizontal RMS for static RTPPP changes from 0.017 m to 0.032 m and the average vertical RMS degrades from 0.020 m to 0.037m. If the outage happened during the convergence period, such as Set 2 and Set 3, the main trend of the positioning will be convergence progress during the next two hours, also the degradation trend caused by the predicted satellite products can be seen by some stations. For Set 3, the convergence trend is a more obvious cause for the outage happened at the very beginning of the positioning. The kinematic results show the average horizontal RMS converges from 1.105 m to 0.368 m, while the vertical horizontal RMS improves from 1.202 m to 0.380 m. For static RTPPP for Set 3, the mean horizontal RMS witnesses an improvement from 0.900 m to 0.192 m and the average vertical RMS improves from 1.048 m to 0.221 m. Meanwhile, both the real-time static PPP and field test approve that the new real-time PPP system has the ability to mitigate the outage.

CHAPER SEVEN: CONCLUSIONS AND FUTURE WORK

7.1 Summary

The primary objective of this thesis is the design and development of an innovative robust real-time PPP system with high availability based on IP. After defining the concept and structure of the new real-time PPP system components, the related function modules in each component were developed and implemented. A prototype system was developed, and extensive tests were carried out to assess the performance of the new real-time PPP system with a focus on IP products with scalable update rates and the positioning performance during outages of orbit and clock corrections. The proposed new real-time PPP system improves system availability and robustness as well as system cost-effectiveness. The primary conclusions are summarized in Section 7.2 and the suggestions for future works are presented in Section 7.3.

7.2 Conclusions

1. The satellite clock offset prediction model is investigated focusing on the effects of periodic terms. For the satellite clock offsets, the periodic terms of 12 hours and 6 hours are obvious with the long-term data analysis (the whole year of 2016) and the amplitudes can reach several hundred ps level, which needs to be considered during the modeling and prediction.
2. The satellite clock offsets prediction with different update rate is investigated. The higher of the update rate, the worse of the prediction accuracy. The results show that the STD for IIR/Rb is 0.41 ns, 0.47 ns and 0.62 ns over 1 hour, 3 hours and 6 hours correspondingly. For IIR-M/Rb, the STD is 0.35 ns, 0.42 ns and 0.61 ns. For IIF/Rb, the

values are 0.24 ns, 0.39 ns and 0.60 ns, which is the best result among all the GPS satellite clocks. For IIF/Cs, the corresponding STD are 1.12 ns, 1.25 ns and 1.83 ns, which is the worst among all the clocks onboard GPS satellites.

3. A new prediction algorithm is proposed for IGS RTS clock products by adding the broadcast ephemeris as a constraint. Meanwhile, the clock offset term in the polynomial part is not estimated in the fitting process and the latest clock offset term from the RTS is directly used as long as the quality check is passed. The new algorithm shows improvements over the current method.
4. The satellite orbit can be predicted very precisely and the update rates can be much longer than the satellite clock. The average RMSE are 2.35 cm, 2.58 cm, and 2.42 cm for the predicted orbit over 1 h in radial, along-track, and cross-track directions, respectively. For predictions over 6 h, the average RMSE just increases slightly to 2.54 cm, 2.72 cm, and 2.79 cm in each of the three directions. Even for predictions over 12 h, the average RMSE is 3.14 cm, 3.17 cm, and 3.30 cm.
5. A prototype of the new real-time PPP system is implemented and extensively tested in real-time. The results indicate the outage has less effect on the positioning accuracy when the position has converged. In that case, the positioning results will degrade slowly with time. For kinematic RTPPP, the average horizontal RMS changes from 0.117 m to 0.198 m while the vertical RMS degrades from 0.196 m to 0.238 m. The average horizontal RMS for static RTPPP changes from 0.017 m to 0.032 m and the average vertical RMS degrades from 0.020 m to 0.037 m. When the outage happened during the convergence period, such as Set 2 and Set 3, the main trend of the positioning will be convergence

during the next two hours, also the degradation trend caused by the predicted satellite products can be seen by some stations. For Set 3, the convergence trend is more obvious because the outage happened at the very beginning of the positioning. As we can see from the kinematic results, the average horizontal RMS converges from 1.105 m to 0.368 m, while the vertical horizontal RMS improves from 1.202 m to 0.380 m. For static RTPPP for Set 3, the mean horizontal RMS witnesses an improvement from 0.900 m to 0.192 m and the average vertical RMS improves from 1.048 m to 0.221 m.

7.3 Suggestions for Future Work

1. Extend the new PPP system from GPS to multi-constellation.

   Currently, the new real-time PPP prototype only works with GPS. With the rapid development of the multi-GNSS, the extension of the system to adapt the other constellations, such as GLONASS, Galileo and BeiDou, will be carried in future.

2. To extend the new PPP system to single frequency and triple frequency PPP

   The new real-time PPP system is mainly tested with the dual frequency ionosphere-free combinations of GPS observations. The system will be extended to include both single frequency and triple frequency.

3. To extend the new PPP system to develop IP products for atmospheric corrections

   The new real-time PPP system is focused on satellite orbit and clock products, while other augmentation information such as ionospheric corrections and troposphere corrections can also benefit the positioning, which can be implemented afterwards.

4. To extend the new PPP system with the option of ambiguity resolution

The new real-time PPP system is now providing solutions with float ambiguities. With the phase bias disseminated in real-time, the real-time ambiguity resolution function can also be added to the system lately.

5. To extend the new PPP system with the option of ambiguity resolution

   To include the integrity information for corresponding IP products such as the degradation factor and the products variance. With additional integrity information, the real-time PPP system can be more robust and reliable.

REFERENCES

Abdel-salam MA (2005) Precise Point Positioning Using Un-Differenced Code and Carrier Phase Observations. Deparment Geomatics Eng Dr thesis, Univ Calgary, UCGE Reports Number 20229

Abdelazeem M, Çelik RN, El-Rabbany A (2016) An enhanced real-time regional ionospheric model using IGS real-time service (IGS-RTS) products. J Navig 69:521–530

Allan DW (1987) Time and frequency(time-domain) characterization, estimation, and prediction of precision clocks and oscillators. IEEE Trans Ultrason Ferroelectr Freq Control 34:647–654

Allan DW, Barnes JA (1981) A modified“ Allan variance” with increased oscillator characterization ability. In: Thirty Fifth Annual Frequency Control Symposium. 1981. IEEE, pp 470–475

Altamimi Z, Rebischung P, Métivier L, Collilieux X (2016) ITRF2014: A new release of the International Terrestrial Reference Frame modeling nonlinear station motions. J Geophys Res Solid Earth 121:6109–6131

Arnold D, Meindl M, Beutler G, et al (2015) CODE’s new solar radiation pressure model for GNSS orbit determination. J Geod 89:775–791

Ashby N (2004) The Sagnac effect in the global positioning system. In: Relativity in Rotating Frames. Springer, pp 11–28

Ashby N, Spilker JJ (1996) Introduction to relativistic effects on the Global Positioning System. Glob Position Syst Theory Appl 1:623–697

Banville S, Langley RB (2010) Instantaneous Cycle-Slip Correction for Real-Time PPP

Applications. Navigation 57:325–334

Bergland G (1969) Fast Fourier transform hardware implementations--A survey. IEEE Trans Audio Electroacoust 17:109–119

Beutler G, Brockmann E, Gurtner W, et al (1994) Extended orbit modeling techniques at the CODE processing center of the international GPS service for geodynamics (IGS): theory and initial results. Manuscr Geod 19:367–386

Bhattarai S (2015) Satellite clock time offset prediction in global navigation satellite systems

Bilitza D (2001) International reference ionosphere 2000. Radio Sci 36:261–275

Bilitza D, Reinisch BW (2008) International reference ionosphere 2007: improvements and new parameters. Adv Sp Res 42:599–609

Black HD, Eisner A (1984) Correcting satellite Doppler data for tropospheric effects. J Geophys Res Atmos 89:2616–2626

Chen J, Li H, Wu B, et al (2013) Performance of real-time precise point positioning. Mar Geod 36:98–108

Chen K, Gao Y (2005) Real-time precise point positioning using single frequency data. In: ION GNSS-2005. pp 1514–1523

Choy S, Bisnath S, Rizos C (2017) Uncovering common misconceptions in GNSS Precise Point Positioning and its future prospect. GPS Solut 21:13–22

Collins JP, Langley RB (1996) Mitigating tropospheric propagation delay errors in precise airborne GPS navigation. In: Position Location and Navigation Symposium, 1996., IEEE 1996. IEEE, pp 582–589

Collins P, Lahaye F, Héroux P, Bisnath S (2008) Precise point positioning with ambiguity

resolution using the decoupled clock model. In: Proceedings of the 21st international technical meeting of the satellite division of the Institute of Navigation (ION GNSS 2008)

de Bakker PF, Tiberius CCJM (2017) Real-time multi-GNSS single-frequency precise point positioning. GPS Solut 1–13. doi: 10.1007/s10291-017-0653-2

Desai S, Bertiger W, Garcia-Fernandez M, et al (2014) Status and plans at the JPL IGS analysis center. In: Intl. GNSS Service 2014 Workshop Compendium, Ed. IGS Central Bureau. p 53

El-Mowafy A, Deo M, Kubo N (2017) Maintaining real-time precise point positioning during outages of orbit and clock corrections. GPS Solut 21:937–947. doi: 10.1007/s10291-016-0583-4

Elsobeiey M, Al-Harbi S (2016) Performance of real-time Precise Point Positioning using IGS real-time service. GPS Solut 20:565–571

Fliegel HF, Gallini TE, Swift ER (1992) Global positioning system radiation force model for geodetic applications. J Geophys Res Solid Earth 97:559–568

Folkner WM, Williams JG, Boggs DH (2008) The planetary and lunar ephemeris DE 421. JPL IOM 343R-08-003

Fritsche M, Sośnica K, Rodríguez-Solano CJ, et al (2014) Homogeneous reprocessing of GPS, GLONASS and SLR observations. J Geod 88:625–642

Gakstatter E (2013) Sources of Public, Real-Time, High-Precision Corrections. GPS-world Retrieved May 24:2016

Gao Y, Chen K (2004) Performance Analysis of Precise Point Positioning Using Rea-Time Orbit and Clock Products. J Glob Position Syst 3:95–100

Gao Y, Shen X (2002) A New Method for Carrier-Phase-Based Precise Point Positioning.

Navigation 49:109–116

Gao Y, Zhang W, Li Y (2017) A New Method for Real-Time PPP Correction Updates. Int Assoc Geod Symp

Geng J, Teferle FN, Meng X, Dodson AH (2011) Towards PPP-RTK: Ambiguity resolution in real-time precise point positioning. Adv Sp Res 47:1664–1673

Gérard P, Luzum B (2010) IERS Conventions (2010). Bur Int Des Poids Mes Sevres 1–179

Hackman C (2012) Accuracy/precision of USNO predicted clock estimates for GPS satellites. NAVAL OBSERVATORY WASHINGTON DC

Hadas T, Kaplon J, Bosy J, et al (2013) Near-real-time regional troposphere models for the GNSS precise point positioning technique. Meas Sci Technol 24:55003

Hopfield HS (1969) Two-quartic tropospheric refractivity profile for correcting satellite data. J Geophys Res 74:4487–4499

Huang GW, Zhang Q, Xu GC (2014) Real-time clock offset prediction with an improved model. GPS Solut 18:95–104

IGS (2018a) IGS products. accessed at http://www.igs.org/products on 2018-01-25

IGS (2018b) IGS Analysis of Broadcast Ephmeris. accessed at http://www.igs.org/analysis/gps-broadcast at 2018-01-25

IGS (2018c) IGS Analysis of Final Products. accessed at http://http://www.igs.org/analysis/gps-final on 2018-01-25

Jakowski N, Hoque MM, Mayer C (2011) A new global TEC model for estimating transionospheric radio wave propagation errors. J Geod 85:965–974

Klobuchar JA (1987) Ionospheric time-delay algorithm for single-frequency GPS users. IEEE

Trans Aerosp Electron Syst 325–331

Kouba J (2009a) A simplified yaw-attitude model for eclipsing GPS satellites. GPS Solut 13:1–12. doi: 10.1007/s10291-008-0092-1

Kouba J (2009b) A Guide to using international GNSS Service (IGS) Products. Geod Surv Div Nat Resour Canada Ottawa 6:34

Kouba J, Héroux P (2001) Precise point positioning using IGS orbit and clock products. GPS Solut 5:12–28

Laurichesse D (2011) The CNES Real-time PPP with undifferenced integer ambiguity resolution demonstrator. In: Proceedings of the ION GNSS. pp 654–662

Leandro R, Landau H, Nitschke M, et al (2011) RTX positioning: the next generation of cm-accurate real-time GNSS positioning. In: ION GNSS

Leandro R, Santos MC, Langley RB (2006) UNB neutral atmosphere models: development and performance. In: Proceedings of ION NTM. pp 564–573

Li P, Zhang X (2014) Integrating GPS and GLONASS to accelerate convergence and initialization times of precise point positioning. GPS Solut 18:461–471

Li X (2012) Improving real-time PPP ambiguity resolution with ionospheric characteristic consideration. Proc ION GNSS-12, Inst Navig Nashville, Tennessee, Sept 17–21

Li X, Ge M, Dai X, et al (2015a) Accuracy and reliability of multi-GNSS real-time precise positioning: GPS, GLONASS, BeiDou, and Galileo. J Geod 89:607–635

Li X, Ge M, Zhang X, et al (2013) Real-time high-rate co-seismic displacement from ambiguity-fixed precise point positioning: Application to earthquake early warning. Geophys Res Lett 40:295–300

Li Y, Gao Y, Shi J (2016) Improved PPP ambiguity resolution by COES FCB estimation. J Geod 90:437–450

Li Y, Li B, Gao Y (2015b) Improved PPP ambiguity resolution considering the stochastic characteristics of atmospheric corrections from regional networks. Sensors 15:29893–29909

Liu S, Stürze A (2013) An evaluation of the IGS real time service based on PPP. Geodätische Woche 2013, B Abstr 1–17

Merino MMR, Lainez MD (2012) Integrity for advanced precise positioning applications. Proc ION 2012 (Nashville, TN,, 17–21 Sept 2012) 2742–2758

Mervart L, Lukes Z, Rocken C, Iwabuchi T (2008) Precise point positioning with ambiguity resolution in real-time. In: Proceedings of ION GNSS. pp 397–405

Montenbruck O, Gill E (2000a) Satellite Orbits: Models, Methods and Applications. Science 134:220

Montenbruck O, Gill E (2000b) Satellite Orbits: Models, Methods and Applications. Science 134:220

Montenbruck O, Schmid R, Mercier F, et al (2015a) GNSS satellite geometry and attitude models. Adv Sp Res 56:1015–1029. doi: 10.1016/j.asr.2015.06.019

Montenbruck O, Steigenberger P, Hauschild A (2015b) Broadcast versus precise ephemerides: a multi-GNSS perspective. GPS Solut 19:321–333

Munthe-Kaas H (1999) High order Runge-Kutta methods on manifolds. Appl Numer Math 29:115–127

Niell AE (1996) Global mapping functions for the atmosphere delay at radio wavelengths. J Geophys Res Solid Earth 101:3227–3246

Nordsieck A (1962) On numerical integration of ordinary differential equations. Math Comput 16:22–49

Petit G, Luzum B (2010) IERS conventions (2010). BUREAU INTERNATIONAL DES POIDS ET MESURES SEVRES (FRANCE)

Radicella SM (2009) The NeQuick model genesis, uses and evolution. Ann Geophys 52:417–422

Rothacher M (2016) Satellite Antenna Phase Center Offsets and the Terrestrial Scale

RTCM (2016) RTCM 10403.3, Differential GNSS (Global Navigation Satellite Systems) Services - Version 3, October 7, 2016

Saastamoinen J (1972) Atmospheric correction for the troposphere and stratosphere in radio ranging satellites. use Artif Satell Geod 247–251

Seepersad G, Bisnath S (2015) Reduction of PPP convergence period through pseudorange multipath and noise mitigation. GPS Solut 19:369–379

Senior KL, Ray JR, Beard RL (2008) Characterization of periodic variations in the GPS satellite clocks. Gps Solut 12:211–225

Shi J, Xu C, Guo J, Gao Y (2014) Local troposphere augmentation for real-time precise point positioning. Earth, planets Sp 66:30

Skone S (2013) ENGO 633: Atmospheric Effects on Satellite Navigation Systems, Lecturenotes, Department of Geomatics Engineering, University of Calgary, 2013

Springer TA, géodésique S helvétique des sciences naturelles. C (2000) Modeling and validating orbits and clocks using the global positioning system. Schweizerische Geodätische Kommission

Takasu T, Yasuda A (2013) RTKLIB ver. 2.4.2 Manual. 181

Teunissen P, Montenbruck O (2017) Springer handbook of global navigation satellite systems. Springer

U.S. COAST GUARD NAVIGATION CENTER (2018) GPS Constellation Status. accessd at https://www.navcen.uscg.gov/?Do=constellationStatus at 2018-01-25

van Bree RJP, Tiberius CCJM (2012) Real-time single-frequency precise point positioning: accuracy assessment. GPS Solut 16:259–266

Weber G (2012) Real-time GNSS Introduction

Weber G, Dettmering D, Gebhard H (2005) Networked transport of RTCM via internet protocol (NTRIP). In: A Window on the Future of Geodesy. Springer, pp 60–64

Weber G, Mervart L (2007) The BKG Ntrip Client (BNC). In: Report on EUREF symposium

Wu J-T, Wu SC, Hajj GA, et al (1992) Effects of antenna orientation on GPS carrier phase. In: Astrodynamics 1991. pp 1647–1660

Wu X, Hu X, Wang G, et al (2013) Evaluation of COMPASS ionospheric model in GNSS positioning. Adv Sp Res 51:959–968

Yang H (2017) High Availability of Real-time PPP by Extending SSR Orbit and Clock Corrections. Proc 30th Int Tech Meet Satell Div Inst Navig (ION GNSS+ 2017) Sept 25 - 29, 2017 Oregon Conv Cent Portland, Oregon 4011–4025

Yang H, Gao Y (2017) GPS Satellite Orbit Prediction at User End for Real-Time PPP System. Sensors 17:1981

Yang H, Gao Y, Xu C, Nie Z (2017a) Keynote: Analysis of the Extended Orbit and Clock Corrections for Real-Time PPP. Proc ION 2017 Pacific PNT Meet Honolulu, Hawaii 653–658

Yang H, Xu C, Gao Y (2017b) Analysis of GPS satellite clock prediction performance with different update intervals and application to real-time PPP. Surv Rev 1–10

Yuan Y, Zhang K, Rohm W, et al (2014) Real-time retrieval of precipitable water vapor from GPS precise point positioning. J Geophys Res Atmos 119:10044–10057

Zhang X, Li X (2012) Instantaneous re-initialization in real-time kinematic PPP with cycle slip fixing. GPS Solut 16:315–327

PUBLICATIONS DURING THIS Ph.D. STUDY

Journal publications:

1. Yang, H., Xu, C., & Gao, Y. (2017). Analysis of GPS satellite clock prediction performance with different update intervals and application to real-time PPP. Survey Review, 1-10.
2. Yang, H., & Gao, Y. (2017). GPS Satellite Orbit Prediction at User End for Real-Time PPP System. Sensors, 17(9), 1981.
3. Nie, Z., Gao, Y., Wang, Z., Ji, S., & Yang, H. (2018). An approach to GPS clock prediction for real-time PPP during outages of RTS stream. GPS Solutions, 22(1), 14.

Conference publications:

1. Yang, Hongzhou, Gao, Yang, Regional TEC Modelling Based on Combined GPS/BeiDou, Proceedings of the 28th International Technical Meeting of The Satellite Division of the Institute of Navigation (ION GNSS+ 2015), Tampa, Florida, September 2015, pp. 3589-3598.
2. Nie, Zhixi, Gao, Yang, Wang, Zhenjie, Yang, Hongzhou, Performance Analysis of Combined GPS, GLONASS and BeiDou RTK Based on Single Differenced Observations between Receivers, Proceedings of the 28th International Technical Meeting of The Satellite Division of the Institute of Navigation (ION GNSS+ 2015), Tampa, Florida, September 2015, pp. 2753-2765.
3. Xiang, Yan, Gao, Yang, Chen, Xingyu, Yang, Hongzhou, TEC Extraction with Different Schemes to Model DCB Under Various Ionosphere Conditions, Proceedings of the 28th International Technical Meeting of The Satellite Division of the Institute of Navigation (ION GNSS+ 2015), Tampa, Florida, September 2015, pp. 3608-3614.

4. Yang, Hongzhou, Gao, Yang, "An Investigation of GPS Satellite Clock Offsets Prediction with Different Update Intervals and Application to Real-Time PPP," Proceedings of the 29th International Technical Meeting of The Satellite Division of the Institute of Navigation (ION GNSS+ 2016), Portland, Oregon, September 2016, pp. 822-832.

5. Liu, Fei, Yang, Hongzhou, Gao, Yang, "Tightly Coupled Kinematics Visual Odometry/PPP System for Land Vehicle Navigation," Proceedings of the 29th International Technical Meeting of The Satellite Division of the Institute of Navigation (ION GNSS+ 2016), Portland, Oregon, September 2016, pp. 1330-1337.

6. Yang, Hongzhou, Gao, Yang, Xu, Chaoqian, Nie, Zhixi, "Keynote: Analysis of the Extended Orbit and Clock Corrections for Real-Time PPP," Proceedings of the ION 2017 Pacific PNT Meeting, Honolulu, Hawaii, May 2017, pp. 653-658.

7. Yang, Hongzhou, "High Availability of Real-time PPP by Extending SSR Orbit and Clock Corrections," Proceedings of the 30th International Technical Meeting of The Satellite Division of the Institute of Navigation (ION GNSS+ 2017), Portland, Oregon, September 2017, pp. 4011-4025. (Best student paper award)

8. Yang Hongzhou, Gao Yang, Zhang Liang, Nie Zhixi, “A new satellite clock offset prediction method based on the IGS RTS products” (Accepted by “Lecture Notes in Electronic Engineering--- China Satellite Navigation Conference 2018 Proceedings”)

9. Zhou Peiyuan, Gao Yang, Yang Hongzhou, “High-precision GLONASS Orbit Prediction for Real-time Precise Point Positioning” (Accepted by “Lecture Notes in Electronic Engineering--- China Satellite Navigation Conference 2018 Proceedings”)